2015

Graphene Based Metamaterials For Terahertz Cloaking And Subwavelength Imaging

Seyedali Forouzmand
University of Mississippi

GRAPHENE BASED METAMATERIALS FOR TERAHERTZ CLOAKING AND SUBWAVELENGTH IMAGING

A Thesis
presented in partial fulfillment of requirements
for the degree of Master of Science
in the Department of Electrical Engineering
with Emphasis in Electromagnetics
The University of Mississippi

by

SEYEDALI FOROUZMAND

August 2015

ABSTRACT

Graphene is a two-dimensional carbon crystal that became one of the most controversial topics of research in the last few years. The intense interest in graphene stems from recent demonstrations of their potentially revolutionary electromagnetic applications – including negative refraction, subdiffraction imaging, and even invisibility – which have suggested a wide range of new devices for communications, sensing, and biomedicine. In addition, it has been shown that graphene is amenable to unique patterning schemes such as cutting, bending, folding, and fusion that are predicted to lead to interesting properties.

A recent proposed application of graphene is in engineering the scattering properties of objects, which may be leveraged in applications such as radar-cross-section management and stealth, where it may be required to make one object look like another object or render an object completely invisible. We present the analytical formulation for the analysis of electromagnetic interaction with a finite conducting wedge covered with a cylindrically shaped nanostructured graphene metasurface, resulting in the scattering cancellation of the dominant scattering mode for all the incident and all the observation angles. Following this idea, the cylindrical graphene metasurface is utilized for cloaking of several concentric finite conducting wedges. In addition, a wedge shaped metasurface is proposed as an alternative approach for cloaking of finite wedges.

The resolution of the conventional imaging lenses is restricted by the natural diffraction limit. Artificially engineered metamaterials now offer the possibility of creating a superlens that overcomes this restriction. We demonstrate that a wire medium (WM) slab loaded with graphene sheets enables the enhancement of the near field for subwavelength imaging at terahertz (THz)

frequencies. The analysis is based on the nonlocal homogenization model for WM with the additional boundary condition in the connection of wires to graphene. The principle of the operation of the proposed lens depends on the enhancement of evanescent waves, wherein the excited surface plasmons at the lower and upper graphene interfaces are coupled by an array of metallic wires. The resolution and the operating frequency of the subwavelength imaging device are mainly determined by the tunability of graphene and the structural parameters of the WM slab. The proposed structure has a resolution better than $\lambda/10$ with the advantages of broad bandwidth, low sensitivity to losses, and tunability with respect to the chemical potential even if the distance between two graphene sheets is a significant fraction of wavelength. As a supplementary study, the performance of WM slab loaded with nanostructured graphene metasurfaces as a novel sub-diffraction imaging lens is studied. It is observed that the dual nature (capacitive/inductive) of the nanostructured graphene metasurface can be utilized to design a dual-band lens in which the subwavelength imaging simultaneously at two tunable distinct frequencies is possible. The analytical results which are presented throughout this thesis, are validated with the full-wave electromagnetic simulator, CST Microwave Studio.

DEDICATION

This work is dedicated to my family for all their love and sacrifice on my behalf.

ACKNOWLEDGMENTS

I would like to express the deepest appreciation to my advisor, Dr. Alexander B. Yakovlev, for his constant support and advice in the completion of this work. He has shown immense patience in mentoring me and guided me in the past two years. This work would not have been possible without his guidance and expert advice.

I would like to thank the committee members Dr. Paul M. Goggans and Dr. Elliott Hutchcraft for the fruitful discussions and valuable suggestions. I am thankful to the Graduate School for providing me the financial support and all the necessary facilities during my graduate studies.

I take this opportunity to express gratitude to all of the Department of Electrical Engineering faculty members especially Dr. Viswa Viswanathahan – Professor and Chair of Electrical Engineering – and Dr. Richard Gordon – Associate Professor in the Department of Electrical Engineering – for their help and support. I also thank my parents for the unceasing encouragement, support and attention.

I also place on record, my sense of gratitude to one and all, who directly or indirectly, have lent their hand in this venture.

TABLE OF CONTENTS

LIST OF TABLES

LIST OF FIGURES

CHAPTER I

ELECTROMAGNETIC CLOAKING OF A FINITE CONDUCTING WEDGE WITH A NONOSTRUCTURED GRAPHENE METASURFACE

1.1 Introduction

Recently, the phenomenon of cloaking with electromagnetic metamaterials has attracted considerable attention, and it has become the subject of intensive research. The cloaking in general is the cancellation of the scattered electromagnetic field from an arbitrarily shaped object by utilizing a surrounding cover which causes the total scattering suppression for all observation angles in the near and far field. Although obtaining invisibility and camouflaging is the most well-known application of cloaking, this technique enables some other exciting applications, including non-invasive sensing [1], [2], low-noise biomedical sensing and imaging, and low interface communications [3]-[7].

In order to obtain electromagnetic cloaking, various techniques have been proposed. A prominent approach is transformation optics which is based on the manipulation of the electromagnetic wave propagation in such a way that the cloak bends the wave around the object [8]-[11]. This phenomenon has been realized by applying a surrounding medium with spatially inhomogeneous and anisotropic properties. Although this technique can theoretically cause perfect cloaking, the experimental fabrication is intensively sensitive to any imperfection [12], [13]. As an alternative approach, the plasmonic cloaking method has been proposed in [14]-[22].

The operation mechanism of this cloak is based on the fact that the volume polarizations of the proposed cloak and the object cancel out each other and the total induced dipole moment of the structure is equal to zero thus the corresponding system becomes invisible for all observation angles.

In [23]-[29], another approach has been proposed which is based on the nonresonant cancellation of the dominant scattering mode of electrically small dielectric and conducting cylinders and spheres. In this method, unlike the aforementioned techniques which have the common feature of using bulk volumetric metamaterials, an ultrathin and conformal isotropic metasurface is utilized. The induced surface current on the metasurface radiates the anti-phase scattered field which cancels the scattered field from the object and leads to a significant scattering reduction. The metasurface has been characterized by an average surface reactance with the analytical expression obtained for the printed and slotted periodic arrays of some canonical subwavelength elements [25], [26]. The desired surface reactance to cancel the dominant scattering mode from the object can be obtained by adjusting the structural parameters of the metasurface.

In order to obtain the maximum scattering cancellation for a conducting object, capacitive surface reactance is desired. It is shown in [30] that the periodic array of graphene nanopatches, unlike the uniform graphene monolayer which is intrinsically inductive, has dual capacitive/inductive properties in the low THz spectrum. The proper capacitive reactance of graphene nanopatches can be obtained by a proper selection of the gap, array periodicity, and Fermi energy level of graphene. In addition, graphene has unique properties such as low-loss surface reactance, large tunability with respect to the applied bias voltage, and mechanical flexibility to wrap around an arbitrary shaped object, and it has been shown in [31] that the nanostructured graphene metasurface can be effectively used for cloaking both dielectric and

metallic cylinders at low THz frequencies.

The material proposed in this chapter concerns the analysis of electromagnetic interaction with finite conducting wedges covered with a nanostructured graphene metasurface, resulting in the scattering cancellation of the dominant scattering mode. It should be noted that the electromagnetic scattering from an infinite conducting wedge has been analyzed based on a variety of analytical and asymptotic approaches, including the uniform theory of diffraction, geometrical optics, and geometrical theory of diffraction [32]-[36]. On the other hand, the scattering problem of a finite conducting wedge has not been extensively studied [37], [38].

Here, we propose an analytical approach to cloak a finite conducting wedge with an arbitrary opening angle by utilizing a cylindrically shaped nanostructured graphene metasurface. We employ the tunability property of graphene to obtain the appropriate surface reactance for cloaking the structure with various opening angles by adjusting the graphene's chemical potential. Following this idea, we show that the proposed cylindrically shaped metasurface cloak can drastically decrease the total scattering width of several concentric finite conducting wedges. In addition, we propose an alternative approach to cloak a finite conducting wedge by a wedge shaped metasurface.

This chapter is organized as follows: In Section 1.2, the formulation and solution of the scattering problem of a finite conducting wedge covered by a cylindrically shaped periodic array of graphene nanopatches are presented. In Section 1.3, the analytical results are accurately validated with full-wave simulations for a wedge with the opening angles of $\pi/4$ and $3\pi/4$. In Section 1.4, we study the performance of the cylindrically shaped metasurface cloak for two concentric conducting wedges. In Section 1.5, we propose a wedge shaped metasurface cloak as an alternative approach for cloaking a finite conducting wedge.

1.2 Formulation and Solution of the Scattering Problem

The geometry of a finite conducting wedge covered by a conformal nanostructured graphene metasurface is shown in Figure 1.1. Figure 1.1(a) illustrates a cross-section view of a finite conducting wedge with the radius R_0, the opening angle α, covered by a cloak of graphene nanopatches with the radius R_c, with the space between the cloak and the conducting wedge filled with a dielectric of thickness R_c-R_0. The structure is considered infinite along the z-axis. Figure 1.1(b) demonstrates a 3D view of the same structure. Here, we consider a transverse magnetic (TM) polarized plane wave normally incident ($\theta = 90°$) on the structure with the incident angle of γ with respect to the x-axis in the x-y plane. The time dependence of the form $e^{j\omega t}$ is assumed and suppressed.

In order to solve the scattering problem, the total space is divided into three regions as shown in Figure 1.1(a). In these regions, the electric fields are expressed in terms of the series expansion of Bessel and Hankel functions in the cylindrical coordinates as follows:

Region I ($0 \le R \le R_0$, $-\alpha < \phi < +\alpha$),

$$E_z^I = \sum_{i=0}^{\infty} A_{v_i} J_{v_i}(\beta_1 R)\cos(v_i\phi) + \sum_{i=1}^{\infty} B_{\tau_i} J_{\tau_i}(\beta_1 R)\sin(\tau_i\phi) \tag{1.1}$$

where $\beta_1 = \beta_0\sqrt{\varepsilon_1}$ is the wave number in region I, $\beta_0 = \omega/c$ is the free space wave number, ω is the angular frequency, c is the speed of light in vacuum, $J_{v_i,\tau_i}(.)$ are the Bessel functions of the first kind, and $v_i = \frac{(2i+1)\pi}{2\alpha}$ and $\tau_i = \frac{i\pi}{\alpha}$ are the eigenvalues obtained subject to the boundary condition for the tangential electric field at $\phi = \pm\alpha$ [37].

Region II ($R_0 \le R \le R_c$, $-\pi < \phi < +\pi$),

$$E_z^{II} = \sum_{n=0}^{\infty} [a_n J_n(\beta_2 R) + b_n Y_n(\beta_2 R)]\cos(n\phi)$$

$$+\sum_{n=1}^{\infty}[c_n J_n(\beta_2 R)+d_n Y_n(\beta_2 R)]\sin(n\phi). \tag{1.2}$$

Region III ($R_c \le R \le \infty$, $-\pi < \phi < +\pi$),

$$E_z^{\text{inc}} = \sum_{n=0}^{\infty} A_n^{\text{inc}} J_n(\beta_0 R)\cos(n\phi) + \sum_{n=1}^{\infty} B_n^{\text{inc}} J_n(\beta_0 R)\sin(n\phi)$$

$$E_z^{\text{scat}} = \sum_{n=0}^{\infty} A_n^{\text{scat}} H_n^{(2)}(\beta_0 R)\cos(n\phi) + \sum_{n=1}^{\infty} B_n^{\text{scat}} H_n^{(2)}(\beta_0 R)\sin(n\phi)$$

$$E_z^{III} = E_z^{\text{scat}} + E_z^{\text{inc}} \tag{1.3}$$

where $\beta_2 = \beta_0\sqrt{\varepsilon_2}$ is the wave number in region II, $J_n(.)$ and $Y_n(.)$ are the Bessel functions of the first and second kind, respectively, $H_n^{(2)}(.)$ are the Hankel functions of the second kind, $A_n^{\text{inc}} = E_0(2/\xi_n)j^n\cos(n\gamma)$ and $B_n^{\text{inc}} = 2E_0 j^n\sin(n\gamma)$ are the amplitude coefficients of the incident field, $\xi_n = 2$ for $n = 0$, and $\xi_n = 1$ for $n \neq 0$. In (1.1)-(1.3), A_{v_i}, B_{τ_i}, a_n, b_n, c_n, d_n, A_n^{scat}, and B_n^{scat} are the unknown amplitude coefficients, which can be characterized into two independent systems: B_n^{scat}, c_n, d_n, B_{τ_i} and A_n^{scat}, a_n, b_n, A_{v_i}. Each system of unknown coefficients can be solved independently by enforcing the following boundary conditions.

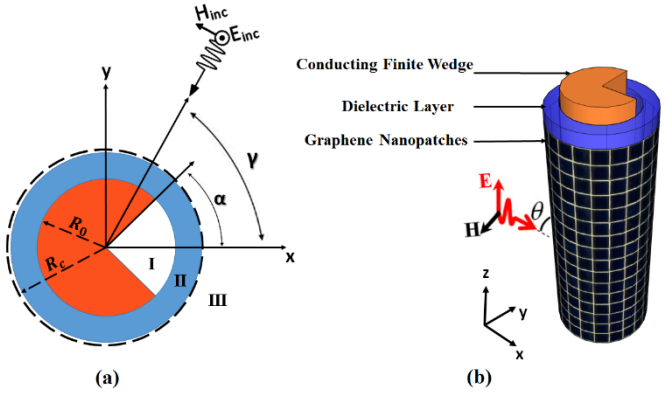

Figure 1.1. Geometry of the finite conducting wedge coated by the graphene-nanopatch metasurface: (a) cross-section view and (b) three-dimensional (3D) view.

First, two-sided impedance boundary conditions should be applied on the surface of the metasurface cloak at $R = R_c$, such that the tangential electric and magnetic fields can be related via the sheet impedance as follows:

$$E_z^{\text{scat}} + E_z^{\text{inc}} = E_z^{II} \tag{1.4}$$

$$Z_s\left(H_\phi^{\text{scat}} + H_\phi^{\text{inc}} - H_\phi^{II}\right) = E_z^{II} \tag{1.5}$$

where H_ϕ^{scat}, H_ϕ^{inc}, and H_ϕ^{II} are the corresponding magnetic field components obtained from the Maxwell's equations. Z_s is the surface impedance of the graphene-nanopatch metasurface covering the wedge and given by [30], [31]:

$$Z_s = R_s + jX_s = \frac{D}{\sigma_s(D-g)} - j\frac{\pi}{2\omega\varepsilon_0\left(\frac{\varepsilon_2+1}{2}\right)D\ln\left[\csc\left(\frac{\pi g}{2D}\right)\right]}. \tag{1.6}$$

In (1.6), R_s is the surface resistance per unit cell related to the conduction losses, X_s is the surface reactance per unit cell, D is the periodicity, g is the gap size, ε_2 is the permittivity of the dielectric layer, and σ_s is graphene's complex surface conductivity which is modeled with the Kubo formula using closed-form expressions for the interband (σ_{inter}) and intraband (σ_{intra}) contributions with the analytical expressions obtained in [39]:

$$\sigma_{\text{intra}} = -j\frac{k_B e^2 T}{\pi\hbar^2(\omega - j2\Gamma)}\left(\frac{\mu_c}{Tk_B} + 2\ln\left(e^{-\frac{\mu_c}{Tk_B}} + 1\right)\right)$$

$$\sigma_{\text{inter}} = \frac{je^2}{4\pi\hbar}\ln\left(\frac{2|\mu_c| - (\omega + j\tau^{-1})\hbar}{2|\mu_c| + (\omega + j\tau^{-1})\hbar}\right)$$

$$\sigma_s = \sigma_{\text{intra}} + \sigma_{\text{inter}}. \tag{1.7}$$

In (1.7), $\hbar$ is the reduced Plank's constant, e is the electron charge, k_B is Boltzmann's constant, τ is the relaxation time, T is the temperature, Γ is a phenomenological scattering rate, and μ_c is the chemical potential. It should be noted that σ_{intra} dominates σ_{inter} at low THz frequencies. In [40], it has been shown that different factors such as substrate type, edge-related

effect, frequency, and incident wave polarization have influences on the value of the momentum relaxation time of graphene nanostructures when $\hbar\omega > 0.2$ eV and the dimensions are small. However, here, in our designs, the operating frequency is $f_0 = 3$ THz and leads to $\hbar\omega = 12.4$ meV, which is much smaller than the optical phonon threshold $\hbar\omega = 0.2$ eV. In this regard, we have considered a constant relaxation time in our designs, which is consistent with the measured results in [41]-[45].

In addition, the tangential components of the electric and magnetic fields should be continuous on the surface of the wedge and on the dielectric interface at $R = R_0$,

$$E_z^{II} = \begin{cases} E_z^I & -\alpha \le \phi \le \alpha \\ 0 & -\pi \le \phi \le -\alpha\,,\ \alpha \le \phi \le \pi \end{cases} \tag{1.8}$$

$$H_\phi^{II} = H_\phi^I \qquad -\alpha \le \phi \le \alpha\ . \tag{1.9}$$

The analytical approach details to calculate the unknown scattering coefficients (A_n^{scat} and B_n^{scat}) are provided in the Appendix. The scattering problem can be similarly solved for the transverse electric (TE) polarized plane wave. It is also worth noting that the first TM harmonic is the dominant scattering mode of the scattering from a finite conducting wedge and leads to a large total scattering cross-section in comparison to the TE-polarized excitation. Hence, we have focused our designs and calculations on a TM-polarized plane-wave excitation.

To illustrate the efficiency of the proposed structure in the reduction of scattering from a finite conducting wedge, we utilize the total scattering width (W_{total}) as a quantitative criterion to describe the overall visibility of an object at the operation frequency. The scattering coefficients are related to the total scattering cross-section through the formula (normalized with respect to the wavelength) [37]:

$$\frac{W_{\text{total}}}{\lambda_0} = \frac{1}{\pi}\left\{\sum_{n=0}^{\infty} |A_n^{\text{scat}}|^2\, \xi_n + \sum_{n=1}^{\infty} |B_n^{\text{scat}}|^2\right\}. \tag{1.10}$$

Due to the non-symmetrical geometry of the finite conducting wedge, it is important to study the behavior of scattering for different observation angles. Therefore, the bi-static scattering cross-section (normalized with respect to the wavelength) is calculated by [37]

$$\frac{W_{\text{bistatic}}}{\lambda_0} = \frac{2}{\pi}\left|\sum_{n=0}^{\infty} A_n^{\text{scat}}\, e^{\frac{jn\pi}{2}} \cos(n\phi) + \sum_{n=1}^{\infty} B_n^{\text{scat}} e^{\frac{jn\pi}{2}} \sin(n\phi)\right|^2 \tag{1.11}$$

where ϕ is the observation angle. The ultimate goal is the suppression of the total scattering width for all the incident angles and obtaining all-angle invisibility independently of the position of observer.

1.3 Results and Discussions

Here, we investigate the total scattering width of a finite conducting wedge with the radius $\lambda_0/20$ and the opening angle $\alpha = \pi/4$, covered by a nanostructured graphene metasurface with $R_c = 1.5R_0$ as shown in Figure 1.1(a). We consider a dielectric with the relative permittivity $\varepsilon_2 = 4$ (i.e., silicon dioxide, SiO_2 or boron nitride, BN) between the cloak and the conducting wedge to avoid an electric short. By a careful study on the scattering properties of a finite conducting wedge with an ideal mantle cloak, it was observed that a cloak with capacitive behavior can significantly decrease the total scattering width. For the aforementioned structural parameters, the optimum capacitive reactance to obtain the maximum scattering cancellation for all incident angles (γ) is $X_s = -100\ \Omega$. This required surface reactance can be realized by choosing the parameters of the designed nanopatches as $D = 4.62$ μm, $g = 0.5$ μm, and $\mu_c = 0.5$ eV. It should be noted that since the geometry of this problem is non-symmetric, the total scattering width should be examined for all angles of incidence and the appropriate surface impedance should be chosen in such a way that the maximum scattering cancellation occurs for all incident angles. In all the calculations, we

assume that the operating frequency is $f_0 = 3$ THz and the temperature is 300°K.

Figure 1.2 shows the total scattering cross-section of the structure for both uncloaked and cloaked cases with the momentum relaxation time varied from $\tau = 1.5$ ps to $\tau = 0.5$ ps for the incident angle of $\gamma = 0$. It can be clearly seen that even for a relatively short relaxation time of $\tau = 0.5$ ps that corresponds to higher losses, the cloaking leads to nearly 5 dB scattering suppression, which shows the robustness of the cloaking performance against the effect of losses. Also, for the case of $\tau = 1.5$ ps, the analytical results are validated with CST Microwave Studio [46], showing a good agreement. In Figure 1.3, the solid blue line shows the analytically calculated total scattering width for the cloaked structure with the relaxation time $\tau = 1.5$ ps for $\gamma = \pi/2$. The solid brown line represents the total scattering width of an uncloaked finite conducting wedge. A significant reduction in the total scattering width of the finite conducting wedge is achieved in comparison to the case without the cloak (approximately 6 dB). The results for other incident angles are omitted here for the sake of brevity.

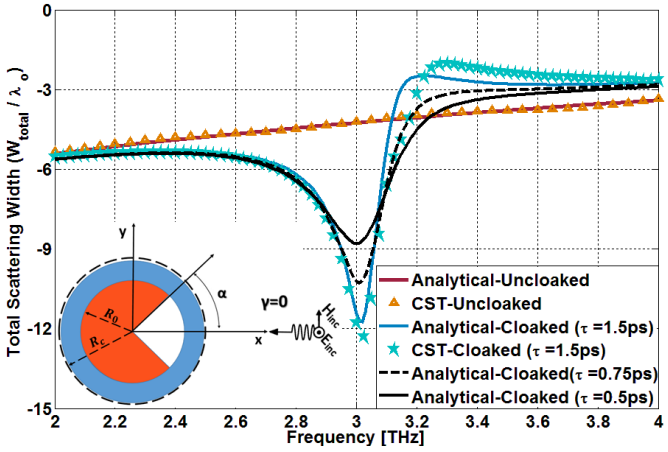

Figure 1.2. Analytical and full-wave simulation results for the total scattering width of cloaked and uncloaked finite conducting wedge with the opening angle $\alpha = \pi/4$ and $\gamma = 0$ for different values of momentum relaxation time.

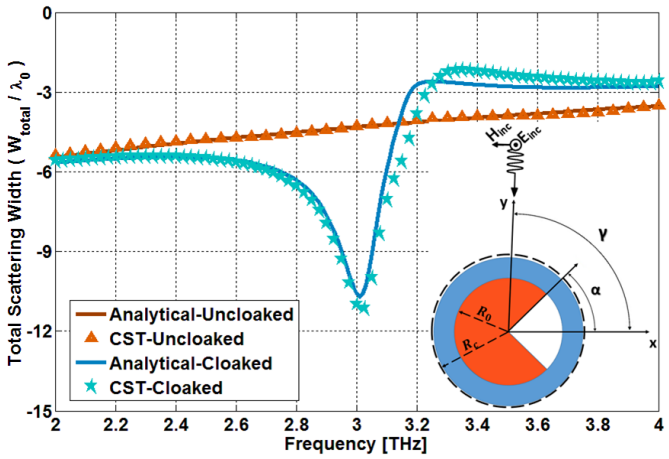

Figure 1.3. Comparison of analytical and full-wave results for the variation of the total scattering width of the finite conducting wedge with and without the metasurface cloak versus frequency for $\alpha = \pi/4$ and $\gamma = \pi/2$.

In order to illustrate the effect of cloaking, a plane wave with the electric field parallel to the z-axis is illuminated on the structure at the design frequency $f_0 = 3$ THz. Figures 1.4(a) and 1.4(b) show the vector power flow distribution in the ϕ-plane for the uncloaked and cloaked finite conducting wedge for the incident angle of $\gamma = 0$. In the presence of the metasurface cloak, most of the energy is drifted around the wedge without remarkable perturbation. However, for the case of no cloak, it is clear that the power distribution is highly perturbed by the object. Figure 1.5 presents a time snapshot of the corresponding electric field distribution in the x-y plane for all the three cases, including the cloaked finite conducting wedge by a cylindrically shaped nanostructured graphene metasurface [Figure 1.5(c)], the uncloaked conducting wedge surrounded by a cylindrically shaped dielectric cover [Figure 1.5(b)], and the isolated finite conducting wedge [Figure 1.5(a)] for the incident angles $\gamma = \pi/2$. It is apparent that the wavefronts of electric field can be restored in the near and far-field regions of the isolated conducting wedge by covering the structure with a graphene-nanopatch metasurface. This means that the capacitive mantle cloak

enables to suppress the scattering from the wedge drastically. The other cases, unlike the cloaked case, strongly disturb the impinging wave in all directions. These results are consistent with the scattering minima shown in Figures 1.2 and 1.3. The results are shown on the same scale for a fair comparison.

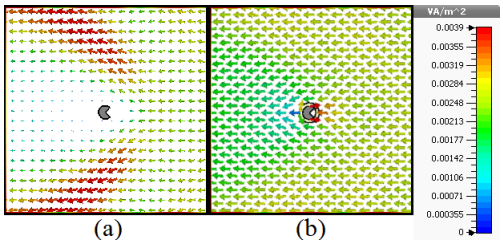

Figure 1.4. Full-wave numerical results for the vector power flow distributions in the ϕ-plane: (a) isolated and (b) cloaked finite conducting wedge for $\alpha = \pi/4$ and $\gamma = 0$.

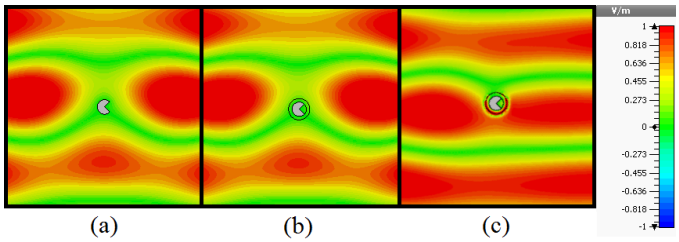

Figure 1.5. Full-wave numerical results for the electric field distribution in the x-y plane for TM polarization: (a) isolated, (b) coated by dielectric, and (c) cloaked finite conducting wedge for $\alpha = \pi/4$ and $\gamma = \pi/2$.

The normalized bi-static scattering cross-section is another criterion which can describe the scattering behavior of an object for different incident angles and observation points. Here, we studied the normalized bi-static scattering cross-section of the cloaked and uncloaked finite conducting wedge with the opening angle, $\alpha = \pi/4$, for different incident angles. In Figure 1.6(a), the solid lines represent the cloaked conducting wedge and the dashed lines show the uncloaked conducting wedge for $\gamma = 0, \pi/4, \text{and } \pi/2$. Figure 1.6(b) shows the scattering reduction

($W_{\text{bistatic,uncloaked}} - W_{\text{bistatic,cloaked}}$) versus observation angle confirming that the scattering width is suppressed effectively for all the observation points.

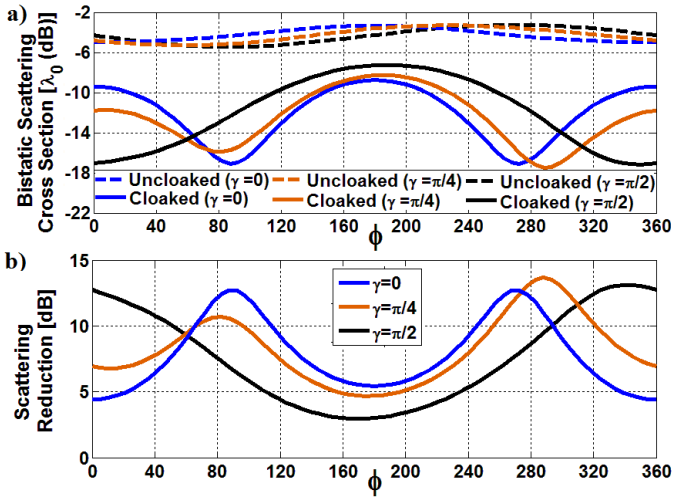

Figure 1.6. (a) Normalized bi-static scattering cross-section of cloaked and uncloaked finite conducting wedge with the opening angle $\alpha = \pi/4$ and (b) the scattering reduction, for different values of incident angle $\gamma = 0, \pi/4$, and $\pi/2$.

We now consider a finite conducting wedge with the radius $\lambda_0/20$ and the opening angle $\alpha = 3\pi/4$, surrounded by graphene nanopatches with $R_c = 1.5R_0$. The dielectric spacer has the relative permittivity $\varepsilon_2 = 4$ and the design frequency is chosen to be $f_0 = 3$ THz. It is observed that the appropriate value of the surface reactance which leads to the minimum SW for all incident angles at the operating frequency is $X_s = -280\ \Omega$. In order to achieve this required surface reactance, the parameters of the optimized cloak are obtained from (1.6) as $D = 4.62$ µm, $g = 0.5$ µm, $\tau = 1.5$ ps, and $\mu_c = 1$ eV. Here, we employ the tunability property of graphene and the required surface reactance has been obtained only by adjusting the graphene's chemical potential. The other physical parameters of the metasurface cloak are kept the same.

Figure 1.7 represents the total scattering width (normalized with respect to the wavelength) for the corresponding conducting wedge with and without the proposed graphene metasurface. The

solid brown line represents the analytically calculated total scattering width of the isolated finite conducting wedge and the solid blue line shows the analytical result which is related to the total scattering width of the cloaked structure with the incident angle $\gamma = 0$. As shown in Figure 1.7, the analytical results are validated with CST Microwave Studio, showing good agreement. Figure 1.8 demonstrates the total scattering width of cloaked and uncloaked conducting wedge with the same structural parameters for $\gamma = \pi/2$. It should be noted that the total scattering reduction depends on the incident angle. The scattering reduction for the incident angle $\gamma = 0$ is around 4 dB and it is approximately 7 dB for $\gamma = \pi/2$ [as shown in Figures 1.7 and 1.8].

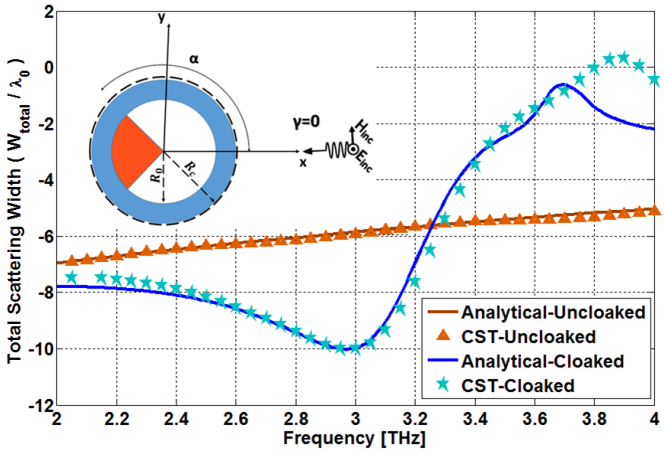

Figure 1.7. Comparison of analytical and full-wave results for the variation of the total scattering width of finite conducting wedge with and without the metasurface cloak versus frequency for $\alpha = 3\pi/4$ and $\gamma = 0$.

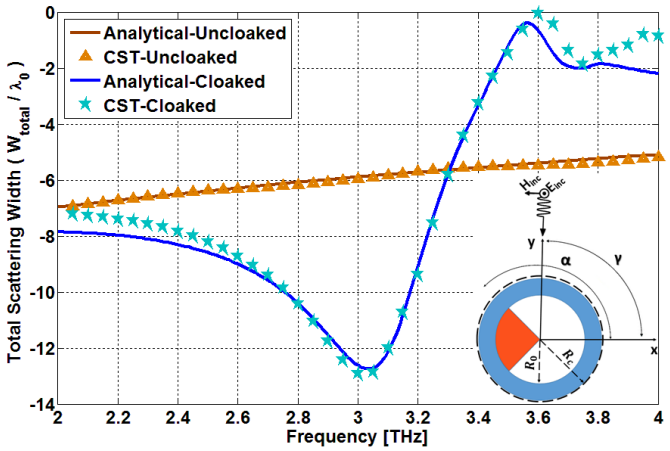

Figure 1.8. Comparison of analytical and full-wave results for the variation of the total scattering width of finite conducting wedge with and without the metasurface cloak versus frequency for $\alpha = 3\pi/4$ and $\gamma = \pi/2$.

Figure 1.9 shows the amplitude of the electric field distributions in the x-y plane. In Figure 1.9(c), the field distribution of the cloaked conducting wedge is shown at the design frequency at which the minimum scattering is achieved. The suppression of the scattered field leads to a uniform and unperturbed planar E-field wave in the near and far-field regions of the structure. Figures 1.9(b) and 1.9(a) correspond to the finite conducting wedge which is covered by a cylindrically shaped dielectric and uncloaked conducting wedge without dielectric, respectively, for the incident angle of $\gamma = 0$. It is shown that these structures scatter the illuminated wave and cause a large perturbation of the field distribution near the structure. Figure 1.10 demonstrates the electric field distribution of the same structure at $\gamma = \pi/2$. In order to have a fair comparison, the same color scale is used.

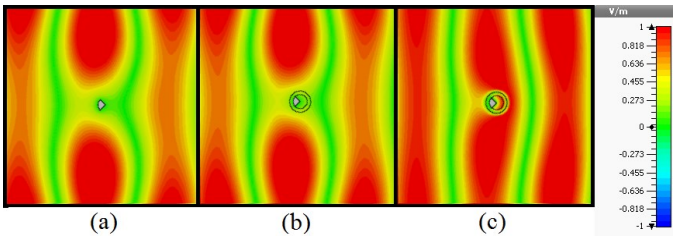

Figure 1.9. Full-wave numerical results for the electric field distribution in the x-y plane for TM polarization: (a) isolated, (b) coated by dielectric, and (c) cloaked finite conducting wedge for $\alpha = 3\pi/4$ and $\gamma = 0$.

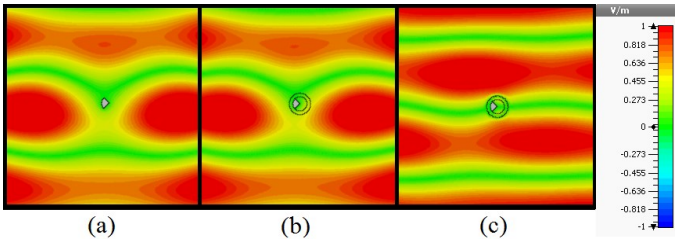

Figure 1.10. Full-wave numerical results for the electric field distribution in the x-y plane for TM polarization: (a) isolated, (b) coated by dielectric, and (c) cloaked finite conducting wedge for $\alpha = 3\pi/4$ and $\gamma = \pi/2$.

Although the total scattering width can provide useful information about the general suppression of the scattered field from an arbitrary object, the ideal cloak can be realized only when the scattering reduction is obtained for all the incident and observation angles. Hence, the bi-static scattering cross-section is calculated to measure the strength of the scattering reduction for all observation points. Figure 1.11(a) represents the normalized bi-static scattering cross-section of the cloaked and uncloaked finite conducting wedge with the opening angle of $\alpha = 3\pi/4$ for three different incident angles of $\gamma = 0,\ \pi/4,$ and $\pi/2$. The solid lines present the bi-static scattering cross-section of the cloaked conducting wedge and the dashed lines show the bi-static scattering cross-section of the uncloaked conducting wedge. A remarkable scattering reduction

($W_{\text{bistatic,uncloaked}} - W_{\text{bistatic,cloaked}}$) for almost all the observation points is achieved as shown in Figure 1.11(b).

As a supplementary study, the total scattering behavior of the structure has been studied for different opening angles and different incident angles. Table 1.1 presents the normalized scattering width of the uncloaked conducting wedge for various values of α and γ. Table 1.2 shows the scattering width of the cloaked finite conducting wedge and the proper capacitive reactance in order to obtain the cloak for different opening angles of wedge and different incident angles. The structural parameters to realize the appropriate reactance can be obtained by applying (1.6). Due to the tunability property of graphene with respect to the chemical potential, it is possible to keep the physical parameters (periodicity and gap) the same and obtain different required reactances by changing the chemical potential. Tables 1.1 and 1.2 imply a significant decrease in the total scattering width. In addition, these results confirm that the cloak is robust for all the angles of incidence.

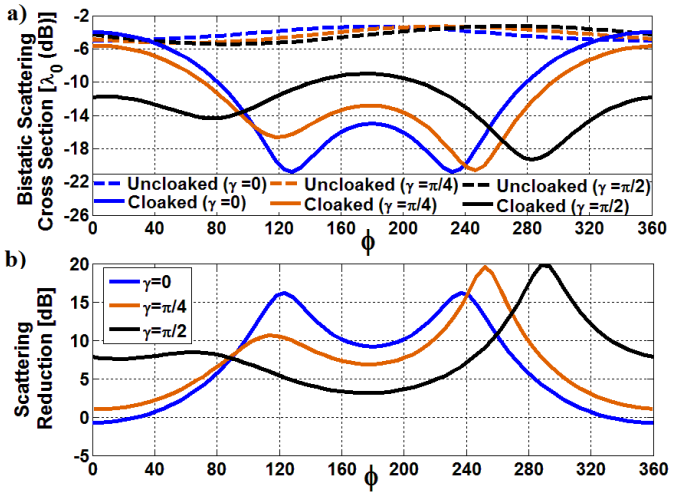

Figure 1.11. (a) Normalized bi-static scattering cross-section of cloaked and uncloaked finite conducting wedge with the opening angle $\alpha = 3\pi/4$ and (b) scattering reduction, for different values of the incident angle $\gamma = 0, \pi/4,$ and $\pi/2$.

Table 1.1. Total scattering width for different opening and incident angles for the uncloaked conducting wedge with $R_0 = \lambda_0 / 20$.

	γ =0, π	**γ=π/4, 3π/4**	**γ =π/2**
α=π/10	-4.0453	-4.0514	-4.0575
α=π/4	-4.1851	-4.2160	-4.2471
α=π/2	-4.7509	-4.8112	-4.8716
α=3π/4	-5.8544	-5.8719	-5.8894
α=π	-7.8750	-7.8496	-7.8242

Table 1.2. Total scattering width for different opening and incident angles for the cloaked wedge with $R_0 = \lambda_0 / 20$, $R_c = 1.5 R_0$, and $\varepsilon_2 = 4$.

	$X_s(\Omega)$	**γ =0, π**	**γ=π/4, 3π/4**	**γ =π/2**
α=π/10	-80	-10.849	-10.8064	-10.4649
α=π/4	-100	-11.73	-12.01	-10.69
α=π/2	-180	-8.6946	-9.8304	-10.5063
α=3π/4	-280	-10.02	-11.3161	-12.6751
α=π	-450	-15.761	-16.8571	-17.9372

1.4 Concentric Finite Conducting Wedges

In Section 1.3, we have demonstrated that it is possible to cloak an isolated finite conducting wedge by covering it with a cylindrically shaped metasurface cloak. Here, we study the possibility of obtaining the cloak for multiple concentric conducting wedges by utilizing the same proposed cylindrically shaped metasurface cloak. This structure is of particular interest due

to its complexity. Although there is an electromagnetic coupling among the objects, we predict that the proposed cloak can decrease drastically the total scattering width of the structure. In the following, we utilize full-wave electromagnetic simulations by the commercial software CST Microwave Studio to investigate the validity of this claim. The combination of two concentric finite conducting wedges is assumed as shown in Figure 1.12. The structure is considered infinite along the z-axis. The radius of each conducting wedge is $\lambda_0/20$, the structure is covered by a metasurface cloak with $R_c = 1.5R_0$, and the dielectric spacer between cloak and structure has the relative permittivity $\varepsilon_2 = 4$. The system is illuminated by a TM polarized plane wave normally incident ($\theta = 90°$) on the structure with the incident angle of γ with respect to the x-axis in the x-y plane.

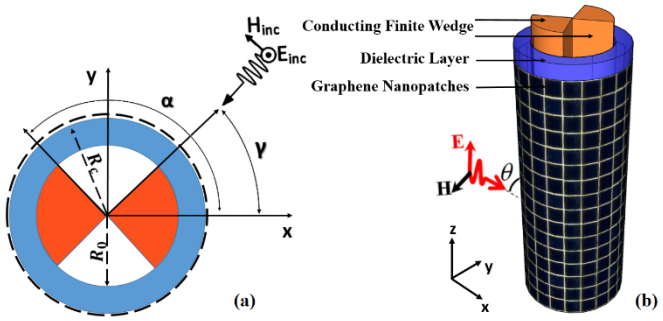

Figure 1.12. Geometry of two concentric finite conducting wedges with the structural parameters: $R_0 = \lambda_0/20$, $R_c = 1.5R_0$, and $\alpha = 3\pi/4$, surrounded by graphene-nanopatch metasurface: (a) cross-section view and (b) 3D view.

Figure 1.13 shows the total radar cross-section (RCS) as a function of frequency from $f =$ 2 THz to $f = 4$ THz. In Figure 1.13, the solid brown line shows the numerically calculated RCS for the cloaked structure, when the structural parameters for the metasurface cloak are chosen the same as the physical parameters in the Section 1.3 for cloaking an isolated conducting wedge with the opening angle $\alpha = 3\pi/4$ and incident angle $\gamma = 0$. It is observed that the minimum scattering

occurs at a frequency higher than the operating frequency ($f_0 = 3$ THz). This means that the appropriate reactance to obtain cloaking at the operating frequency is changed due to the presence of the other finite conducting wedge. As a result, the design of the cover should be modified. A parametric study leads to the numerical optimization of the parameters of the metasurface cloak which is applied to shift the minimum scattering to $f_0 = 3$ THz. Our study illustrates that the proper reactance to cloak this structure for all the incident angles is $X_s = -79\ \Omega$, which can be realized by choosing the parameters of the metasurface as $D = 4.28$ μm, $g = 0.35$ μm, $\tau = 1.5$ ps, and $\mu_c = 0.5$ eV. The solid blue line shows the numerically calculated RCS for the optimized cloak for the incident angle $\gamma = 0$.

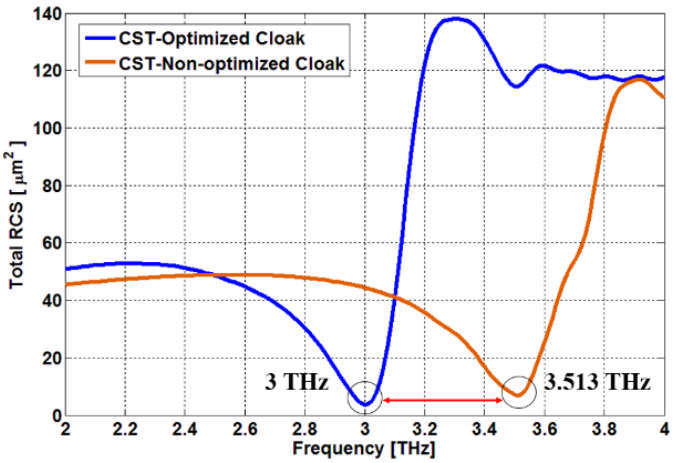

Figure 1.13. Full-wave results for variation of the total RCS versus frequency. The brown solid line is related to the non-optimized cloak of two concentric finite conducting wedge and the blue line corresponds to the optimized cloak.

In order to provide further clarification, the total RCS of the structure without cloak (dash-dotted line) and the uncloaked in the presence of the dielectric spacer (dashed line) are plotted in Figure 1.14 for the incident angle of $\gamma = 0$. Covering the structure with a dielectric layer increases the scattering cross-section due to the fact that the larger objects generally have more significant

dominant scattering coefficients which lead to a larger scattering cross-section. It is surprising to see how the metasurface cloak causes the drastic reduction of the scattering from the entire object. The results for other incident angles are omitted here for the sake of brevity.

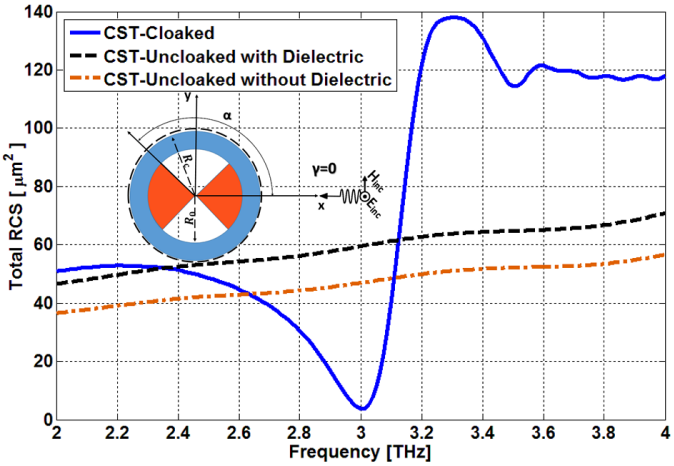

Figure 1.14. Full-wave results for the variation of the total RCS of isolated, covered by dielectric, and cloaked two concentric finite conducting wedge versus frequency for $\alpha = 3\pi/4$ and $\gamma = 0$.

To further show the effect of cloaking, Figure 1.15 presents the vector power flow distribution for the uncloaked [Figure 1.15(a)] and cloaked two concentric finite conducting wedges [Figure 1.15(b)] for the incident angle of $\gamma = 0$ at the operating frequency $f_0 = 3$ THz. Unlike the uncloaked case, wherein the power distribution is highly perturbed by the object, in the cloaked case, a uniform distribution has been obtained indicating that the object is hidden from the incoming wave. Figure 1.16 represents the total electric field distributions in the x-y plane. The structure is excited by a plane wave with the incident angle of $\gamma = \pi/2$. Figure 1.16(c) shows how the mantle cloak effectively reduces the scattering from the structure in such a way that a uniform field is observed outside the cover. It makes the object hardly detectable for an external observer. In the absence of the mantle cloak, the illuminated plane wave induces a strong scattering from the structure, as shown in Figures 1.16(a) and 1.16(b). The same color scale is considered for fair

comparison.

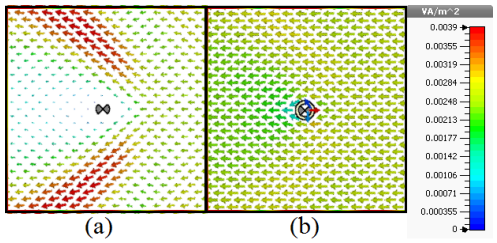

Figure 1.15. Full-wave numerical results for the vector power flow distributions in the ϕ-plane: (a) isolated and (b) cloaked two concentric finite conducting wedges for $\alpha = 3\pi/4$ and $\gamma = 0$.

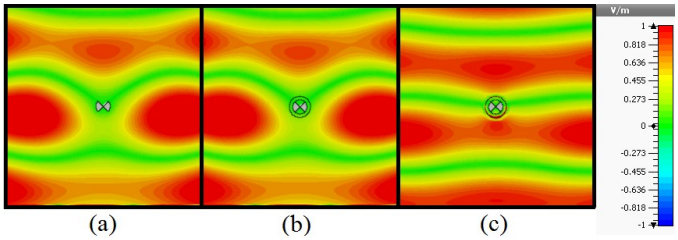

Figure 1.16. Full-wave numerical results for the electric field distribution in the x-y plane for TM polarization: (a) isolated, (b) coated by dielectric, and (c) cloaked two concentric finite conducting wedges for $\alpha = 3\pi/4$ and $\gamma = \pi/2$.

Figure 1.17 demonstrates the far-field radiation patterns of the cloaked and uncloaked two concentric finite conducting wedges for the three cases: $\gamma = 0,\ \pi/4,$ and $\pi/2$. It can be clearly seen that the significant scattering suppression occurs for all the incident angles and all the observation points by comparing the cloaked and uncloaked cases (deducting the bi-static scattering cross-section of the cloaked case from that of the uncloaked case) as shown in Figure 1.17(d). It should be noted that by increasing the angle of incidence, the cloaking efficiency decreases and the worst case is observed at the incident angle of $\gamma = \pi/2$. Even in this case, the presence of the cloak causes a significant scattering reduction.

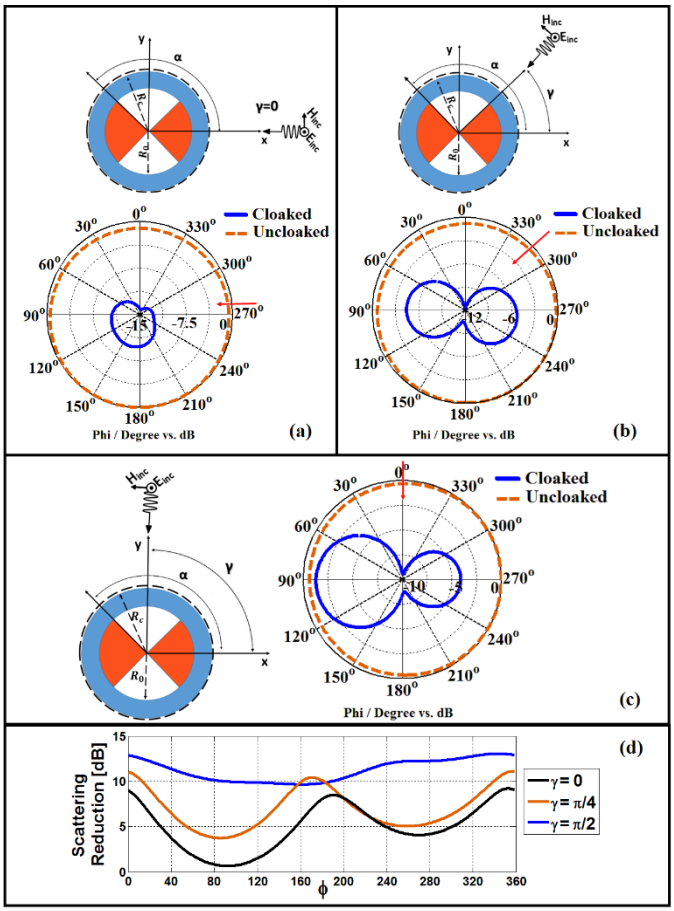

Figure 1.17. Normalized bi-static scattering cross-section of cloaked and uncloaked two concentric finite conducting wedges with the opening angle $\alpha = 3\pi/4$ for the different values of incident angle: (a) $\gamma = 0$, (b) $\gamma = \pi/4$, and (c) $\gamma = \pi/2$. (d) Scattering reduction for the same incident angles.

1.5 Wedge Shaped Cloak

By a careful study of the proposed cylindrically shaped cloak, it reveals that it could not efficiently cloak the conducting wedge with a radius larger than $\lambda/20$. In addition, the volume occupied by the mantle cloak is large. Here, we propose an alternative approach in order to obtain the maximum scattering reduction for a finite conducting wedge by utilizing a wedge shaped cloak.

As shown in Figure 1.18, we consider a finite conducting wedge with the radius $\lambda_0/10$, the opening angle $\alpha = 3\pi/4$, and a TM plane wave normally incident ($\theta = 90°$) on the structure with the incident angle of γ with respect to the x-axis in the x-y plane at the operating frequency $f_0 = 3$ THz. The structure is considered infinite along the z-axis. It should be noted that the thickness of the dielectric spacer should be chosen to restore the illuminated electric field wavefronts in the near and far-field regions. By applying a numerical optimization based on a parametric study, the appropriate thickness for the spacer is $d = 0.3R_0$ with the relative permittivity $\varepsilon_r = 4$. For these structural parameters, the proper capacitive reactance to achieve the minimum scattering width for all the incident angles is $X_s = -56.54\ \Omega$. The proper structural parameters of the nanostructured graphene metasurface can be obtained by (1.6) as following: $D = 4.8683\ \mu$m, $g = 0.475\ \mu$m, $\tau = 1.5$ ps, and $\mu_c = 0.5$ eV.

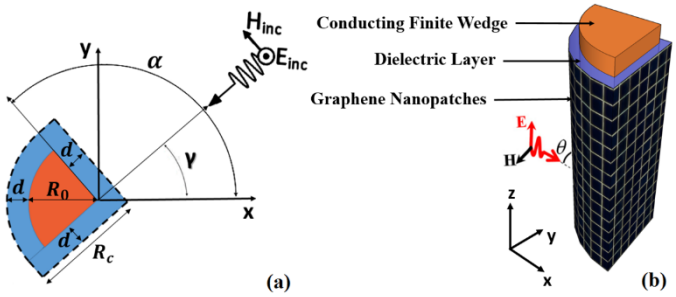

Figure 1.18. Geometry of the finite conducting wedge with the structural parameters: $R_0 = \lambda_0/10$, $d = 0.3R_0$, and $\alpha = 3\pi/4$, surrounded by a wedge shaped graphene-nanopatch metasurface: (a) cross-section view and (b) 3D view.

A full-wave electromagnetic simulation is implemented by the commercial software CST Microwave Studio to study the scattering behavior of the cloaked and uncloaked wedge. In Figure 1.19, the solid blue line presents the numerically calculated RCS for the cloaked structure at the incident angle $\gamma = 0$, the dash-dotted line shows the RCS of the isolated structure without the

cloak and the scattering behavior of the uncloaked structure in the presence of the dielectric layer is depicted by the dashed line in Figure 1.19. The result confirms that a dramatic reduction of scattering is achieved around the operating frequency for the incident angle of $\gamma = 0$. Figure 1.19 indicates an important point that when we cover an isolated finite conducting wedge with a dielectric layer due to the increasing of its size, more significant scattering coefficients appear which cause a larger scattering cross-section. We underline here that due to the complexity of the geometry, no analytical method has been proposed to solve the scattering problem. Therefore, the design and optimization of the cloak is done numerically with CST Microwave Studio. The results for other incident angles are omitted here for the sake of brevity.

In order to provide further illustration, Figures 1.20(a) and 1.20(b) represent the vector power flow distribution for the uncloaked and cloaked finite conducting wedge for the incident angle of $\gamma = 0$. The suppression of the scattered fields leads to a uniform and unperturbed power distribution in the vicinity of the wedge. Figure 1.21 presents a time snapshot of the amplitude of the total electric field distribution for the cloaked [Figure 1.21(c)], the isolated finite conducting wedge [Figure 1.21(a)], and the finite conducting wedge covered by a dielectric [Figure 1.21(b)] at the design frequency $f_0 = 3$ THz for the incident angle $\gamma = \pi/2$. It is clearly shown that by utilizing the wedge shaped mantle cloak, the wavefronts of the electric field can be restored. On the other hand, the electric field distribution is disturbed when the mantle cloak is not implemented.

The figures are plotted on the same scale for fair comparison.

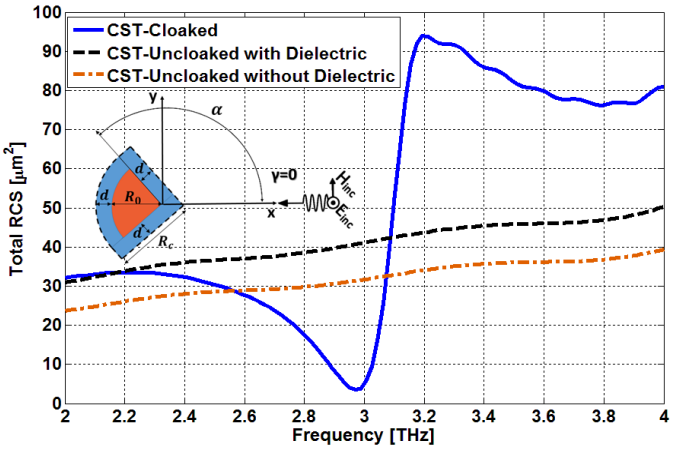

Figure 1.19. Full-wave results for the variation of the total RCS of isolated, covered by dielectric, and cloaked finite conducting wedge versus frequency for $\alpha = 3\pi/4$ and $\gamma = 0$.

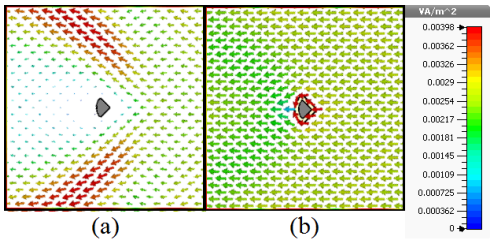

Figure 1.20. Full-wave numerical results for the vector power flow distributions in the ϕ-plane: (a) isolated and (b) cloaked finite conducting wedges for $\alpha = 3\pi/4$ and $\gamma = 0$.

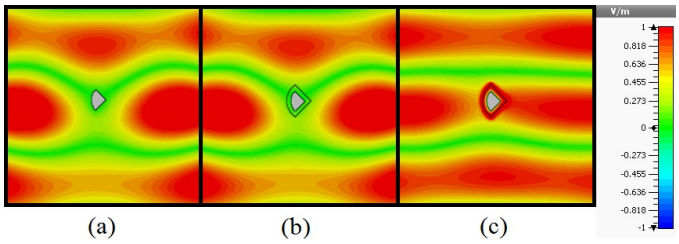

Figure 1.21. Full-wave numerical results for the electric field distribution in the x-y plane for TM polarization: (a) isolated, (b) coated by dielectric, and (c) cloaked finite conducting wedge for $\alpha = 3\pi/4$ and $\gamma = \pi/2$.

The other criterion which can demonstrate the scattering behavior for all the incident angles and all the observation points is the far-field radiation pattern. Figure 1.22 represents the far-field pattern of the cloaked and uncloaked finite conducting wedge for three different incident angles of $\gamma = 0,\ \pi/4, \text{and}\ \pi/2$. A drastic scattering reduction ($W_{\text{bistatic,uncloaked}} - W_{\text{bistatic,cloaked}}$) is observed for the cloaked case in comparison to the uncloaked case for all the observation angles as depicted in Figure 1.22(d). When the incident angle increases, the cloaking performance becomes less efficient and the worst case is related to the incident angle $\gamma = \pi/2$. Even in this case, the cloak results in a dramatic reduction of the scattering from the finite conducting wedge for all the observation angles. It should be emphasized that in order to obtain an omnidirectional cloaking, the surface impedance of the metasurface should be defined as a function of incident angle which goes beyond the scope of this paper. The proposed metasurface cloak is considered as the most efficient approach to cloak the conducting wedge as a non-symmetrical object due to the advantages of the maximum scattering cancellation, low capacitive reactance, the possibility of obtaining cloak even if the radius of the conducting wedge is larger than $\lambda/10$, and occupying less volume when it is wrapped around the structure.

As an extension of this work, the fabrication and measurement of the graphene-nanopatch cloak in the THz regime are of our particular interest. In this regard, the mechanical flexibility of graphene makes it possible to wrap the metasurface cloak around an arbitrary shaped object and the chemical potential can be largely tuned either passively by the doping profile or chemical modification, or actively by external static electric field (providing an isotropic scalar surface conductivity) or external static magnetic field via Hall effect (providing anisotropic and tensor surface conductivity) [6]. Therefore, one of the concerns is related to the bias voltage which should be applied to all the graphene nanopatches.

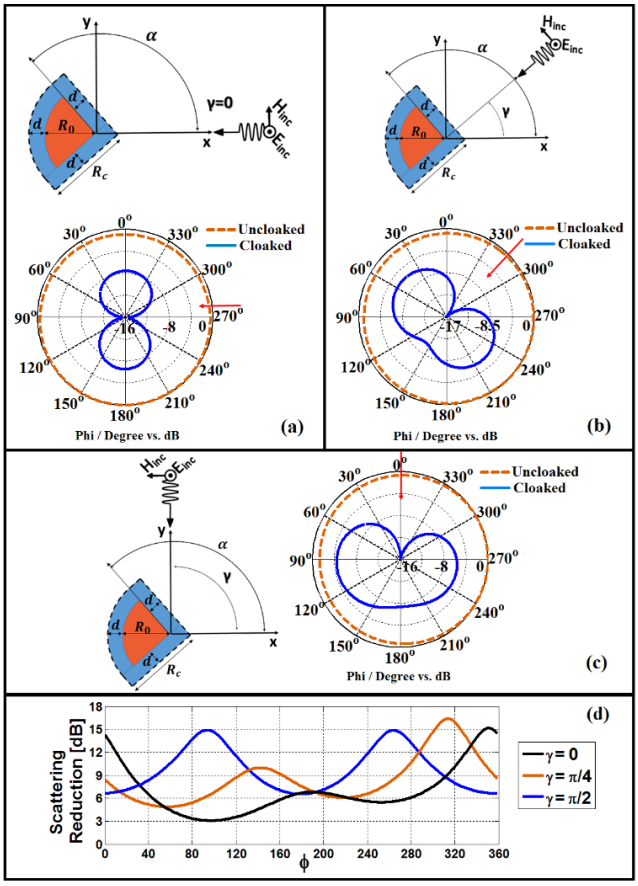

Figure 1.22. Normalized bi-static scattering cross-section of cloaked and uncloaked finite conducting wedge with the opening angle $\alpha = 3\pi/4$ for different values of incident angle (a) $\gamma = 0$, (b) $\gamma = \pi/4$ and (c) $\gamma = \pi/2$. (d) Scattering reduction for the same incident angles.

CHAPTER II

GRAPHENE LOADED WIRE MEDIUM FOR TUNABLE BROADBAND SUBWAVELENGTH IMAGING

2.1 Introduction

Since the resolution of traditional optical lenses is restricted by the diffraction limit, subdiffraction imaging is of particular interest to the metamaterials community. The conventional lenses are not able to transport evanescent near-field modes which carry subwavelength information. In order to overcome this limitation, a well-known solution is to use a metamaterial lens with negative refractive index property. Veselago pointed out the possibility of the existence of a negative index material (NIM) in 1968 [47]. Following this idea, Pendry realized that a NIM slab ($\varepsilon = -1$ and $\mu = -1$) can effectively amplify the exponentially decaying evanescent modes of a source field, and thus, could focus both the evanescent and propagating spectra [48]. Pendry also noticed that a thin slab of silver with only negative permittivity would act as a near-field lens [49]. This lens, which is known as a superlens, has important applications in biomedical imaging, sensing, and nondestructive characterization of materials [50]-[55]. The physical mechanism behind the Pendry's lens can be described as a resonant excitation of coupled surface plasmon polaritons which are supported at the interfaces of the slab. The desired conditions for this technique can be realized at a single carefully selected frequency with high sensitivity to the absorption and frequency dispersion.

Due to the fact that Pendry's subwavelength imaging process physically arises at the lens interfaces, it is also possible to utilize a pair of resonant grids or conjugate sheets instead of a bulk material [56]-[59]. Graphene as a single atom layer of carbon atoms guides surface plasmons [39], [60], [61], and this phenomenon was employed for different metamaterial plasmonic applications [62]-[65]. Recently, Ref. [66] presented a frequency tunable graphene lens, in which the enhancement of evanescent waves for subwavelength imaging is realized by the well coupled graphene sheets that can support surface plasmons. It should be noted that the structure's performance intensely depends on the distance between graphene sheets and the subwavelength information is lost when the thickness of the lens is increased.

Another metamaterial lens with artificially engineered properties has been proposed in [67]-[70]. The idea is that both evanescent and propagating harmonics are transformed into the transmission-line modes along the wires in a WM slab. The loss sensitivity of this structure is remarkably small and the resolution is restricted only by the spacing between the wires. It has been shown that the properties of this lens cannot be tuned after fabrication and the thickness of WM should be chosen in such a way that it is an integer number of half wavelength to satisfy the subwavelength imaging condition.

Here, we propose a WM slab loaded with graphene sheets that provides both of the aforementioned subwavelength imaging properties of the WM and graphene. The enhancement of evanescent waves is provided by the coupling of the surface plasmons at the lower and upper interfaces. The WM slab has a remarkable effect on the strong coupling and waveguiding of evanescent waves to the other side of the structure. The modal dispersion behavior of the proposed structure can be described as the perturbation of the surface plasmons of graphene sheets by utilizing an array of metallic wires. The proposed lens has advantages of widely tunable

subwavelength imaging and the possibility of obtaining image even if the distance between two graphene sheets is a significant fraction of wavelength. In addition, the structure has a remarkable improvement in comparison to other subwavelength imaging devices in terms of bandwidth and position of a source.

The study of the transmission/reflection behavior of the graphene-dielectric stack, provided in [71], was carried out using a simple analytical transfer-matrix method (TMM). Alternatively, the analysis can be realized by using the principles of the circuit-theory model described in [72], wherein graphene sheets are modeled as shunt admittances. Also, in [73], the optical properties of one-dimensional graphene-embedded quarter-wave stack have been investigated by modifying the conventional transfer matrix method [71]. Here, we deal with the analysis of the transmission/reflection properties of the WM slab loaded with graphene sheets, wherein the impinging evanescent waves excite surface plasmons at the interfaces of the structure. A nonlocal homogenization model is utilized [74], [75], such that the WM is modeled as a uniaxial anisotropic material characterized by a nonlocal dielectric function with a generalized additional boundary condition (GABC) at the connection of wires to graphene. We employ two widely used approaches to investigate the imaging properties of the structure. First, we placed an infinite magnetic line source at a distance from the upper interface of the structure, and calculated the magnetic field distribution at the same distance from the lower interface. The resolution of the lens is quantified by the half-power beamwidth (HPBW) criterion [76]. In the second approach, the performance of the lens is assessed by a double-slit source and then interpreted by the Rayleigh criterion [77]-[81]. The analytical results are validated with the full-wave electromagnetic simulator, CST Microwave Studio [46], showing good agreement.

It is also worth noting that in addition to the theoretical studies described above, subwavelength imaging has been verified experimentally with different imaging structures. In [82], an experimental validation of subwavelength imaging by a WM slab has been performed at microwave frequencies. Also, it has been extended to THz and infrared frequencies by employing silver nanorods in [69]. In addition to these WM lenses, recently, subwavelength imaging has been theoretically and experimentally studied in [83] by using a fishnet flat lens, wherein a 3D metamaterial has been fabricated by Printed-Circuit-Board (PCB) technology. This stacked fishnet metamaterial forms waveguide channels, which provide the propagation of quasi-TEM modes in the dielectric layers.

From the experimental point of view, fabrication of the graphene monolayer sheet by itself is a severe challenge. Recently, various methods have been proposed to achieve a graphene monolayer with the lowest imperfection, namely Chemical Vapor Deposition (CVD) [84] and Epitaxy [85]. The process of joining the WM to the intensely thin graphene sheet deals with some difficulties due to the fact that the well-known methods such as ohmic contact, soldering, plasmonic welding are not applicable in the proposed structure. To overcome this limitation, here we show that a small gap between the graphene monolayer and the WM does not change the response of the lens because of the strong coupling of the surface plasmons of the graphene sheet and the WM slab. This approach has been studied by the full-wave simulation in CST Microwave Studio, which confirms this claim. In addition, the possibility of embedding the WM in a dielectric slab facilitates the fabrication and growth of the graphene sheets on the interfaces of the lens [86].

This chapter is organized as follows: In Section 2.2, we present the closed-form expressions for the reflection and the transmission coefficients of the WM slab loaded with graphene sheets based on the nonlocal homogenization model. The dispersion behavior of odd and even modes and

the transmission response of the structure are studied in Section 2.3. In Section 2.4, the performance of the proposed lens is analyzed in the presence of the magnetic line source and the double-slit source. In Section 2.5, we discuss the tunability and broadband properties of the lens. The severe challenges in the practical realization of the lens have been discussed, and a promising approach in order to surmount these difficulties has been proposed in Section 2.6. A time dependence of the form $e^{j\omega t}$ is assumed and suppressed.

2.2 Nonlocal Model for WM with Graphene Sheets

Here, we consider a WM slab loaded with graphene sheets as shown in Figure 2.1. The WM slab consists of the metallic wires symmetrically arranged in a square lattice with the following structural parameters: a is the spacing between the wires (lattice constant), r_0 is the radius of the wires, ε_h is the dielectric permittivity of the slab, and h is the thickness of the structure. The metallic wires are oriented along the z-direction and two graphene sheets are located at $z = 0$ and $z = -h$. To determine the transmission/reflection response of the structure with a TM plane-wave excitation, the even/odd excitation mode technique is utilized. By considering the perfect electric conductor (PEC) and the perfect magnetic conductor (PMC) at the center of the wires ($z = -h/2$), the even and odd responses of the structure can be obtained. Figure 2.1(b) demonstrates the cross-section view in the presence of PEC/PMC symmetries. In the nonlocal homogenization model, a WM is characterized by a uniaxial anisotropic material with the effective permittivity of $\varepsilon_{zz} = \varepsilon_h\left[1 - k_p^2/(k_h^2 - k_z^2)\right]$, where $k_h = k_0\sqrt{\varepsilon_h}$ is the wave number of the host medium, $k_0 = \omega/c$ is the free space wave number, ω is the angular frequency, c is the speed of

light, k_z is the z-component of the wave vector $\vec{k} = (k_x, 0, k_z)$, and k_p is the plasma wave number as $k_p = \sqrt{(2\pi/a^2)/(\ln(a/2\pi r_0) + 0.5275)}$.

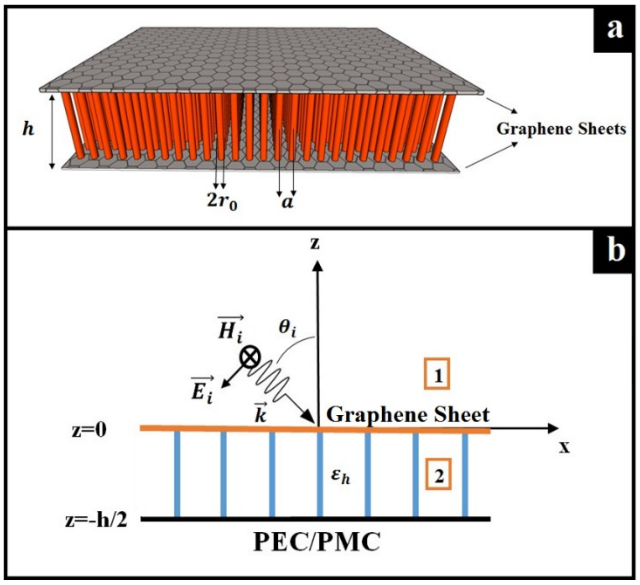

Figure 2.1. Schematics of a WM slab loaded with graphene sheets: (a) 3D view and (b) cross-section view of the structure by considering PEC/PMC at the symmetry plane.

A TM-polarized plane wave excites both transverse electromagnetic (TEM) and the extraordinary TM modes in the homogenized WM slab. First, it is assumed that the PEC plane is located at $z = -h/2$. The total magnetic fields in the air region above the structure (region 1) and in the WM slab (region 2), as shown in Figure 2.1(b), can be written as follows:

$$H_y^{(1)} = (e^{\gamma_0 z} + R_{\text{even}} e^{-\gamma_0 z}) e^{-jk_x x}$$

$$H_y^{(2)} = (A_{\text{TM}}^{+} e^{\gamma_{\text{TM}}\, z} + A_{\text{TM}}^{-} e^{-\gamma_{\text{TM}}\, z} + B_{\text{TEM}}^{+} e^{\gamma_{\text{TEM}}\, z} + B_{\text{TEM}}^{-} e^{-\gamma_{\text{TEM}}\, z}) e^{-jk_x x} \qquad (2.1)$$

where $A_{\text{TM}}^{\pm}$ and $B_{\text{TEM}}^{\pm}$ are the amplitudes of the extraordinary TM and transmission-line TEM modes in the WM slab, R_{even} is the reflection coefficient of the even-mode excitation, $\gamma_0 =$

$\sqrt{k_x^2 - k_0^2}$, $k_x = k_0 \sin\theta_i$ is the x-component of the wave vector $\vec{k} = (k_x, 0, k_z)$, $\gamma_{\mathrm{TEM}} = jk_h = jk_0\sqrt{\varepsilon_h}$, and $\gamma_{\mathrm{TM}} = \sqrt{k_p^2 + k_x^2 - k_0^2}$. In order to determine the unknown coefficients (R_{even}, $A_{\mathrm{TM}}^{\pm}$, and $B_{\mathrm{TEM}}^{\pm}$), the two-sided impedance boundary conditions are satisfied at the graphene interface ($z = 0$):

$$E_x^{(1)}\Big|_{z=0^+} = E_x^{(2)}\Big|_{z=0^-} = Z_g[\, H_y^{(2)}\Big|_{z=0^-} - H_y^{(1)}\Big|_{z=0^+}] \tag{2.2}$$

where the graphene sheet impedance Z_g is given by $Z_g = 1/\sigma_s$, and σ_s is graphene's complex surface conductivity ($\sigma_s = \sigma' + j\sigma''$) which is modeled with the Kubo formula using closed-form expressions for the interband (σ_{inter}) and intraband (σ_{intra}) contributions [60]:

$$\sigma_{\mathrm{intra}} = -j\frac{k_B e^2 T}{\pi\hbar^2(\omega - j\tau^{-1})}\left(\frac{\mu_c}{Tk_B} + 2\ln\left(e^{-\frac{\mu_c}{Tk_B}} + 1\right)\right)$$

$$\sigma_{\mathrm{inter}} \approx -\frac{je^2}{4\pi\hbar}\ln\left(\frac{2|\mu_c| - \omega\hbar}{2|\mu_c| + \omega\hbar}\right)$$

$$\sigma_s = \sigma_{\mathrm{intra}} + \sigma_{\mathrm{inter}}\,. \tag{2.3}$$

In (2.3), $\hbar$ is the reduced Planck constant, e is the electron charge, k_B is the Boltzmann's constant, T is the temperature, τ is the momentum relaxation time, and μ_c is the chemical potential. In the low-THz region and below the interband transition threshold, $\hbar\omega < 2|\mu_c|$, σ_{intra} dominates over σ_{inter} [39]. In the upper GHz and low-THz range, the imaginary part of surface conductivity has a negative value, $\sigma'' < 0$, and graphene acts as an inductive sheet [63], [71]. This behavior of the surface impedance is analogous to the subwavelength metallic mesh grid at microwave frequencies. It should be noted that when $\sigma'' < 0$, a proper TM surface wave can propagate and

for $\sigma'' > 0$, a proper TE surface wave can propagate. In this study, it is assumed that $T = 300$ K, $\varepsilon_h = 1$, $\tau = 0.5$ ps, $a = 215$ nm, and $r_0 = 21.5$ nm.

At the PEC interface ($z = -h/2$), the tangential electric field vanishes implying that $(1/\varepsilon_h)(dH_y/dz) = 0$. Moreover, it has been shown that an additional boundary condition (ABC) is required to describe the appropriate boundary condition for the WM connected to the perfect electric conductor [87]-[91]. The microscopic ABC which is enforced at the PEC ground plane ($z = -h/2^+$) can be written for the wire current, $I(z)$, as [92]:

$$\frac{dI(z)}{dz}\Big|_{z = (-h/2)^+} = 0 \tag{2.4}$$

and in terms of macroscopic fields:

$$\frac{\partial}{\partial z}\left(k_0\varepsilon_h E_z^{(2)} + k_z\eta_0 H_y^{(2)}\right)\Big|_{z = (-h/2)^+} = 0. \tag{2.5}$$

In addition, it requires the use of GABC for the microscopic current at the connection of wires to graphene [74]:

$$\left[\frac{\sigma_s}{j\omega\varepsilon_0\varepsilon_h}\frac{dI(z)}{dz} + I(z)\right]\Big|_{z = 0^-} = 0 \tag{2.6}$$

and in terms of macroscopic fields:

$$\left(1 + \frac{\sigma_s}{j\omega\varepsilon_0\varepsilon_h}\frac{\partial}{\partial z}\right)\left(k_0\varepsilon_h E_z^{(2)} + k_z\eta_0 H_y^{(2)}\right)\Big|_{z = 0^-} = 0. \tag{2.7}$$

By enforcing the aforementioned boundary conditions, the closed-form expression of the reflection coefficient for PEC symmetry (even excitation) can be obtained by [74]

$$R_{\text{even}} = \frac{\frac{N_{\text{even}}}{D_{\text{even}}}\coth\left(\gamma_{\text{TM}}\frac{h}{2}\right)\cot\left(k_h\frac{h}{2}\right) - \left(\frac{1}{\gamma_0} + j\frac{\eta_0}{Z_g k_0}\right)}{\frac{N_{\text{even}}}{D_{\text{even}}}\coth\left(\gamma_{\text{TM}}\frac{h}{2}\right)\cot\left(k_h\frac{h}{2}\right) + \left(\frac{1}{\gamma_0} - j\frac{\eta_0}{Z_g k_0}\right)},$$

$$N_{\text{even}} = \left(\frac{1}{\varepsilon_{zz}^{\text{TM}}} - 1\right)\left(\frac{\sigma_s\gamma_{\text{TM}}}{j\omega\varepsilon_0\varepsilon_h}\tanh\left(\gamma_{\text{TM}}\frac{h}{2}\right) + 1\right) + \left(1 - \frac{\sigma_s k_h}{j\omega\varepsilon_0\varepsilon_h}\tan\left(k_h\frac{h}{2}\right)\right),$$

$$D_{\text{even}} = -\frac{k_h}{\varepsilon_h}\left(\frac{1}{\varepsilon_{zz}^{\text{TM}}} - 1\right)\left(\frac{\sigma_s\gamma_{\text{TM}}}{j\omega\varepsilon_0\varepsilon_h} + \coth\left(\gamma_{\text{TM}}\frac{h}{2}\right)\right) + \frac{\gamma_{\text{TM}}}{\varepsilon_h}\left(\cot\left(k_h\frac{h}{2}\right) - \frac{\sigma_s k_h}{j\omega\varepsilon_0\varepsilon_h}\right). \quad (2.8)$$

The closed-form expression of the reflection coefficient for the PMC symmetry (odd excitation) can be derived using a similar approach:

$$R_{\text{odd}} = \frac{\frac{N_{\text{odd}}}{D_{\text{odd}}}\tanh\left(\gamma_{\text{TM}}\frac{h}{2}\right)\tan\left(k_h\frac{h}{2}\right) - \left(\frac{1}{\gamma_0} + j\frac{\eta_0}{Z_g k_0}\right)}{\frac{N_{\text{odd}}}{D_{\text{odd}}}\tanh\left(\gamma_{\text{TM}}\frac{h}{2}\right)\tan\left(k_h\frac{h}{2}\right) + \left(\frac{1}{\gamma_0} - j\frac{\eta_0}{Z_g k_0}\right)},$$

$$N_{\text{odd}} = \left(\frac{1}{\varepsilon_{zz}^{\text{TM}}} - 1\right)\left(\frac{\sigma_s\gamma_{\text{TM}}}{j\omega\varepsilon_0\varepsilon_h}\coth\left(\gamma_{\text{TM}}\frac{h}{2}\right) + 1\right) + \left(1 + \frac{\sigma_s k_h}{j\omega\varepsilon_0\varepsilon_h}\cot\left(k_h\frac{h}{2}\right)\right),$$

$$D_{\text{odd}} = +\frac{k_h}{\varepsilon_h}\left(\frac{1}{\varepsilon_{zz}^{\text{TM}}} - 1\right)\left(\frac{\sigma_s\gamma_{\text{TM}}}{j\omega\varepsilon_0\varepsilon_h} + \tanh\left(\gamma_{\text{TM}}\frac{h}{2}\right)\right) + \frac{\gamma_{\text{TM}}}{\varepsilon_h}\left(\tan\left(k_h\frac{h}{2}\right) + \frac{\sigma_s k_h}{j\omega\varepsilon_0\varepsilon_h}\right) \quad (2.9)$$

where $\varepsilon_{zz}^{\text{TM}} = \varepsilon_h k_x^2/(k_p^2 + k_x^2)$ is the relative effective permittivity for TM polarization. The results can be validated by considering the limiting case of $\sigma_s \to 0$. In this case, (2.8) and (2.9) turn to the WM slab expressions derived in [91]. The transmission/reflection response of the structure (shown in Figure 2.1(a)) can be obtained by the superposition principle as follows:

$$R = \frac{1}{2}(R_{\text{even}} + R_{\text{odd}}) \quad (2.10)$$

$$T = \frac{1}{2}(R_{\text{even}} - R_{\text{odd}}). \quad (2.11)$$

2.3 Parametric Study of Dispersion and Transmission Properties

Here, we are interested in studying the dispersion behavior of the TM^x surface waves and the transmission response of the WM slab loaded with graphene sheets in order to determine the proper operating frequency regime in which the enhancement of evanescent waves leads to the recovering of the source details at the image plane. The ultimate goal is designing a subwavelength imaging lens with a high resolution and low distortion properties.

First, we study the dispersion relation obtained by applying the perfect magnetic conductor plane at $z = -h/2$ [as shown in Figure 2.1(b)]. The dispersion of the surface waves is calculated by finding the complex roots of the dispersion function [denominator of the reflection coefficient in (2.9)]. Figure 2.2 shows the dispersion behavior of the normalized propagation constant (k_x/k_0) of the odd TM^x modes of the WM slab loaded with graphene sheets with $\mu_c = 1.5$ eV and $h = 2400$ nm. At low frequencies ($f < 18$ THz), the real part of (k_x/k_0) is close to 1 and the imaginary part has a negligibly small negative value, indicating that the proper complex bound mode (surface plasmon) interacts weakly with the WM slab and propagates primarily in the air region in the vicinity of graphene sheet. With the increase of frequency it interacts stronger with the structure, and at a frequency around 19.6 THz a stopband occurs for the first TM^x surface plasmon which corresponds to the left bound of the stopband. The cutoff frequency of the second proper complex bound mode occurs approximately at 65 THz which is considered as the right bound of the stopband. Within the stopband for the proper bound mode (from 19.6 THz to 65 THz), a proper complex leaky wave with Re(k_x/k_0) > 1 and large Im(k_x/k_0)) exists.

Figure 2.3 illustrates the dispersion behavior of the structure for the odd excitation with different thicknesses. It is observed that by increasing the length of the lens, the total behavior of the dispersion does not change drastically. However, the resonance has a remarkable shift to the

lower frequencies. It leads to the expansion of the stopband regime wherein the propagation of the proper (bound) complex modes stops. For example, by changing the length from 400 nm to 3000 nm, the resonance frequency changes from 49.71 THz to 17.34 THz.

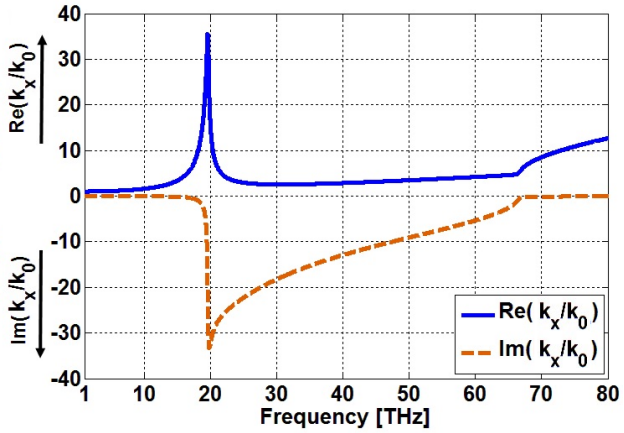

Figure 2.2. Dispersion behavior of the odd modes of a WM slab loaded with graphene sheets. The solid line represents the real part of the normalized propagation constant, $\mathrm{Re}(k_x / k_0)$, and the dashed line represents the imaginary part of the normalized propagation constant, $\mathrm{Im}(k_x / k_0)$.

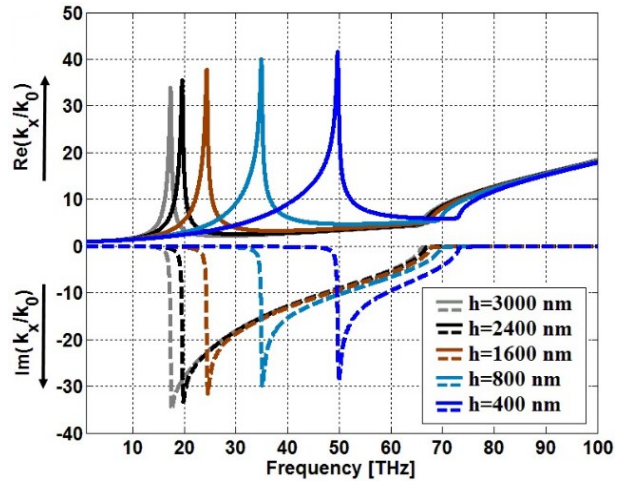

Figure 2.3. Dispersion behavior of the odd modes of the WM slab loaded with graphene sheets with different structure's thicknesses in the range from 400 to 3000 nm. The solid line represents the real part of the normalized propagation constant, $\mathrm{Re}(k_x / k_0)$, and the dashed line represents the imaginary part of the normalized propagation constant, $\mathrm{Im}(k_x / k_0)$.

In order to provide further illustrations, Figure 2.4 shows the dispersion behavior of the structure for the odd excitation with the various values of the chemical potential. The chemical potential can be largely tuned either passively by doping the profile (density and type of carriers) or chemical/structural surface modification, or actively by an external static electric field or magnetic field [60]. It is observed that the resonance corresponding to the left bound of the stopband occurs at lower frequencies by decreasing the graphene's chemical potential. The length of the structure is set to $h = 2400$ nm for all the cases.

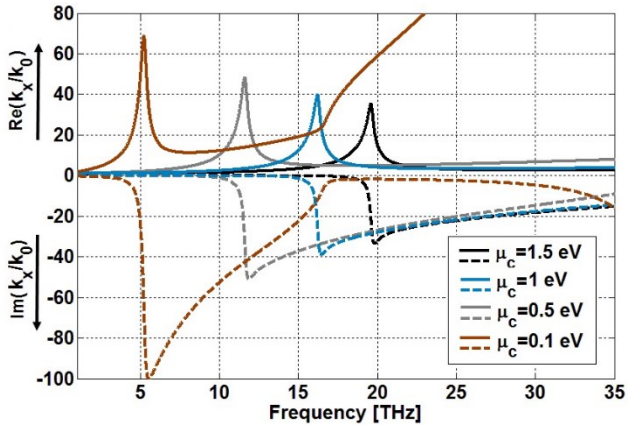

Figure 2.4. Dispersion behavior of the odd modes of the WM slab loaded with graphene sheets with different chemical potentials in the range from 0.5 to 1.5 eV. The solid line represents the real part of the normalized propagation constant, $\mathrm{Re}(k_x/k_0)$,and the dashed line represents the imaginary part of the normalized propagation constant, $\mathrm{Im}(k_x/k_0)$.

Similarly, the response of the structure for the even excitation can be obtained by applying the PEC symmetry in Figure 2.1(b). In this regard, Figure 2.5 shows the dispersion behavior of the normalized propagation constant (k_x/k_0) of the even TM^x modes of the WM slab loaded with graphene sheets with $\mu_c = 1.5$ eV and $h = 2400$ nm. When the real part of (k_x/k_0) is close to 1

and the imaginary part has a small negative value, it indicates that the proper complex (bound) mode interacts weakly with the structure and propagates in the air region in the vicinity of graphene sheets (the solid/dashed brown lines at the frequencies below 50 THz). The other mode as an improper complex leaky wave (solid/dashed blue lines) has a similar dispersion behavior for $\mathrm{Re}(k_x/k_0)$ for the frequencies up to 50 THz. Since $\mathrm{Im}(k_x/k_0)$ of this mode has a large value, the wave attenuates and does not radiate. In this paper, we are interested in subwavelength imaging at low THz frequencies. Therefore, the dispersion behavior at high THz frequencies (frequencies higher than 50 THz) has not been discussed in details. By a careful study of the dispersion relation for odd and even excitations, it concludes that the significant resonance of the structure is associated with the odd modes at low-THz frequencies, and thus, we restrict our analysis to the modes obtained with the PMC symmetry. However, at frequencies higher than 50 THz, the dispersion behavior of the TM^x surface waves for the even excitation, shown by the black line in Figure 2.5, keeps increasing unlike other modes and the imaginary part has a small negative value. Therefore, it should be mentioned that both even and odd excitations play important roles in the formation of resonances with a higher value of k_x/k_0 in this frequency range.

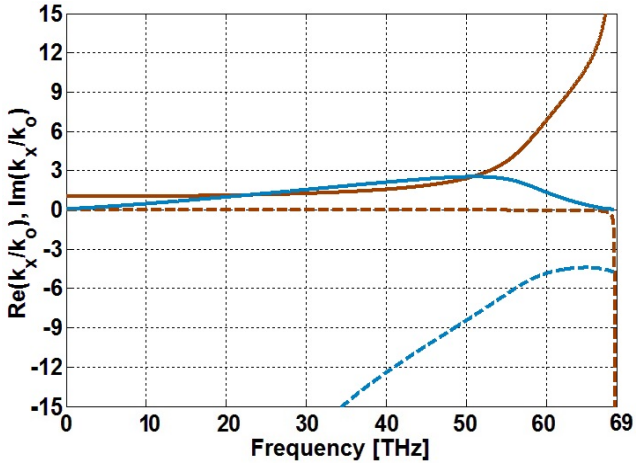

Figure 2.5. Dispersion behavior of the even modes of the WM slab loaded with graphene sheets. The solid line represents the real part of the normalized propagation constant, $\mathrm{Re}(k_x/k_0)$, and the dashed line represents the imaginary part of the normalized propagation constant, $\mathrm{Im}(k_x/k_0)$.

The other criterion that can provide more quantitative and detailed information about the structure's performance in subwavelength imaging is the transmission response of the device as a function of wave vector k_x/k_0 [93]. The behavior of the transmission coefficients is sensitive to the variations in the operating frequency. Therefore, the transmission magnitude $|T|$ as a function of $\mathrm{Re}(k_x/k_0)$ is calculated at different frequencies of operation in the range from 16 to 21 THz and is depicted in Figure 2.6. It is shown that the reduction of the frequency of operation reveals a significant resonant phenomenon which leads to the enhancement of the amplitude of the evanescent modes for a certain range of k_x. The observed resonant enhancement deteriorates the subwavelength imaging since some of the spatial harmonics are amplified by a large factor. In contrast, for the frequencies close to 19 THz, the resonant behavior has not been observed in the transmission coefficients and the transmission magnitude is close to unity for a larger range of spatial harmonics.

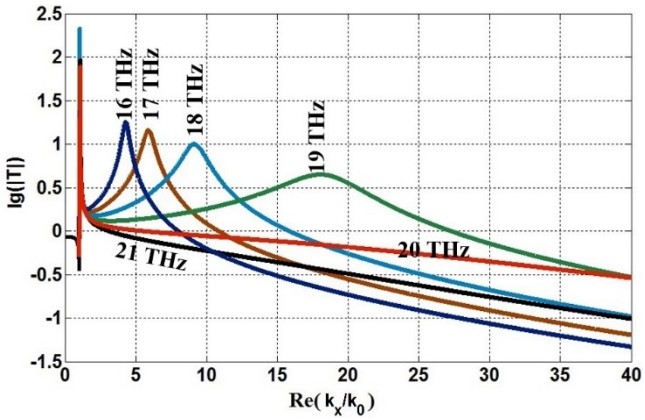

Figure 2.6. Magnitude of the transmission coefficient as a function of k_x/k_0 calculated for a WM slab loaded with graphene sheets in the range from 16 to 21 THz.

We study in detail the dispersion behavior and the transmission response considered as two important parameters in the formation of the subwavelength imaging. As shown in Figures 2.2 and 2.6, at frequencies lower than 18 THz, the imaginary part of the normalized propagation constant of the proper bound mode has a small value [$\mathrm{Im}(k_x/k_0) \approx 0$], and thus, the transmission intensity will be large at the resonance that leads to the overamplification of some of the Fourier components (k_x). This phenomenon diverges the transmission and deteriorates the subwavelength imaging. For this reason, the subwavelength imaging is not possible in this region. In addition, the real part of the normalized propagation constant, $\mathrm{Re}(k_x/k_0)$, is nearly equal to 1, which leads to a transmission resonance at the vicinity of $\mathrm{Re}(k_x/k_0) = 1$. At $18\ \mathrm{THz} < f < 19.6\ \mathrm{THz}$, the imaginary part of the propagation constant increases and prevents the divergence of the transmission and effectively moderates the effects of the resonance. It should be mentioned that although the imaginary part of (k_x/k_0) by itself would not cause a fundamental improvement in the image resolution, any finite amount of $\mathrm{Im}(k_x/k_0)$ in the slab will not allow the transmission to diverge. In this region, by increasing the frequency the resonance peak shifts to a greater value of $\mathrm{Re}(k_x/k_0)$ of the proper complex bound mode, which means that a larger number of Fourier

components can be transferred with a transmission coefficient equal or slightly greater than 1, leading to a better resolution for the structure. At $19.6\ \text{THz} < f < 22\ \text{THz}$ the subwavelength imaging is obtained by coupling of evanescent waves from the source to the leaky wave with both large values of $\text{Re}(k_x/k_0)$ and $\text{Im}(k_x/k_0)$, which exists in the stopband region for the proper complex bound waves. At frequencies higher than 22 THz, the transmission coefficient decays drastically because of the large value of $\text{Im}(k_x/k_0)$ and the small value of $\text{Re}(k_x/k_0)$ of the leaky wave; as a result, the structure has a poor performance in terms of subwavelength imaging. By a careful study of the dispersion relation and the transmission coefficient, it can be concluded that the proper frequency regime is $18.5 - 22$ THz for the aforementioned parameters. In Sec. 2.4, we investigate the validity of this claim.

In order to provide more clarifications regarding the distinct properties of the WM slab loaded with graphene sheets in comparison with the isolated WM slab and parallel graphene sheets, Figure 2.7 shows the dispersion behavior of the bound modes for these three cases with the following parameters: $a = 215$ nm, $r_0 = 21.5$ nm, $\mu_c = 1.5$ eV, and $h = 2400$ nm. The blue solid line represents $\text{Re}(k_x/k_0)$ for the even excitation of the isolated WM slab. At frequencies around 62.5 THz corresponding to $h = \lambda/2$, a stopband occurs for the first TM^x surface-wave mode. It is observed that the second stopband can be obtained by utilizing the odd excitation at $f = 125$ THz ($h = \lambda$). This phenomenon arises due to the fact that the WM slab acts as a Fabry-Perot resonator at frequencies in which the thickness of the structure is an integer number of half wavelength ($h = n\lambda/2$, $n = 1, 2, 3, \ldots$). The solid and dashed orange lines present the dispersion behavior of the two parallel graphene sheets for the even and odd excitations, respectively. It can be clearly seen that the dispersion behavior of the WM slab loaded with graphene sheets is remarkably different from the isolated WM slab and two parallel graphene sheets. Figure 2.7

conveys two important points. First, at low frequencies, the modal behavior of the proposed structure can be described as a perturbation of the surface plasmons of two parallel graphene sheets and it is similar to the dispersion of bound modes in the WM slab at higher frequencies resulting in a Fabry-Perot stopband. The graphene sheets and the WM slab can modulate each other's surface plasmons when they are placed in ultimate close vicinity of each other. Second, the resonance behavior of the proposed structure can be explained in terms of the Fabry-Perot resonance when the electrical thickness of the slab is larger than its physical thickness ($h = 2400$ nm) [72], [94], [95]. It is worth noting that the intrinsically inductive property of graphene at low-THz frequencies provides the required excess length to satisfy the Fabry-Perot resonance condition.

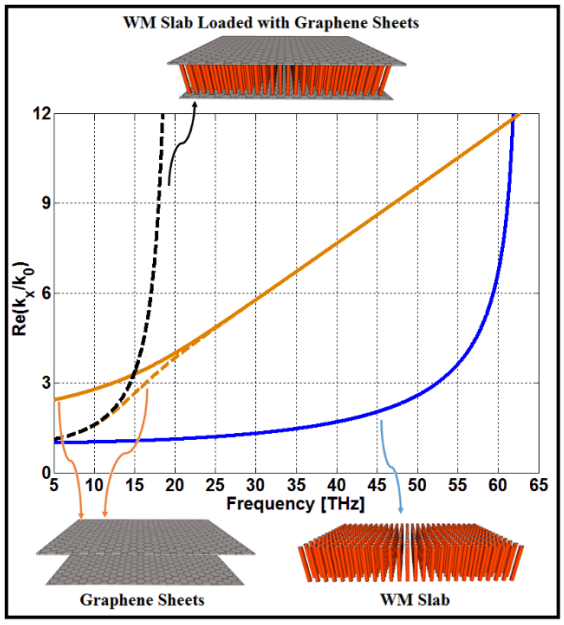

Figure 2.7. Dispersion behavior of the WM slab loaded with graphene sheets (black line), the isolated WM slab (blue line), and two parallel graphene sheets (orange line). The solid lines represent the real part of the normalized propagation constant for even excitation (PEC symmetry) and the dashed lines represent the real part of the normalized propagation constant for odd excitation (PMC symmetry).

In Figure 2.8, we show the transmission characteristics of the WM slab loaded with graphene sheets, the isolated WM slab, and two parallel graphene sheets at the operating frequency of $f = 19$ THz. Due to the fact that the structure thickness is not an integer number of the half wavelength ($h = \lambda/6.58$) the transmission magnitude of the WM slab is lower than 1 [$\lg(|T|) = 0$] and decays rapidly. The transmission of two graphene sheets has two resonances at $k_x/k_0 = 3.623$ and 3.816, then it drops drastically. Figure 2.7 shows that the first resonance corresponds to the odd excitation (dashed orange line), and the second resonance is related to the even excitation (solid orange line) [66]. Rather differently, the transmission curve is smooth and close to unity [$\lg(|T|) = 0$] for a large range of k_x in our proposed structure, which means that two graphene sheets are strongly coupled (even if the thickness of the slab is a large fraction of wavelength) and the near field can be effectively transferred by the array of metallic wires. The physical mechanism of our proposed structure can be explained as the resonant excitation of the surface waves supported by the graphene sheets assisted by the canalization effect of the WM slab.

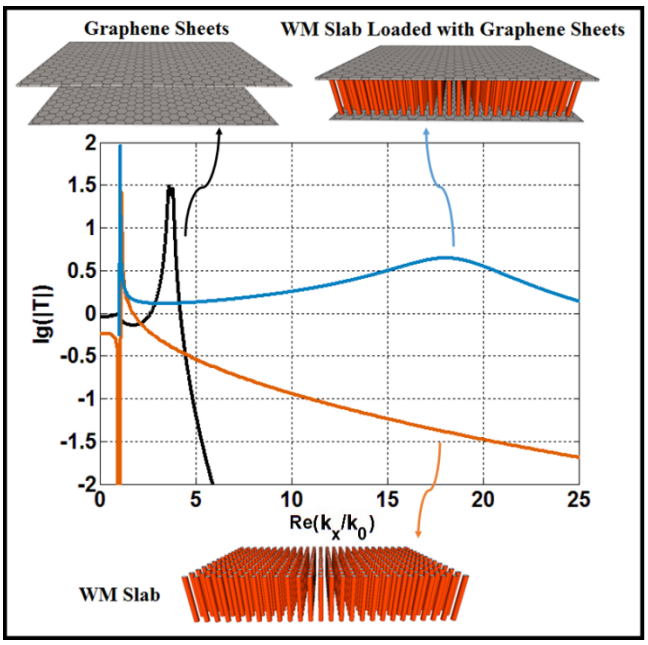

Figure 2.8. Magnitude of the transmission coefficient as a function of k_x / k_0 calculated for a WM slab loaded with graphene sheets, isolated WM slab, and two parallel graphene sheets.

2.4 Study of Resolution

In order to evaluate the subwavelength imaging resolution of a structure, various techniques have been proposed. Here, we utilize two well-known methods to characterize the imaging properties of the structure. The performance of the lens is studied in the presence of the magnetic line and double-slit sources, and the resolution is evaluated by using the HPBW and the Rayleigh criteria.

2.4.1 Magnetic Line Source

We consider an infinite magnetic line source oriented along the y-direction and placed at a distance d from the upper interface of the structure. The geometry is shown in Figure 2.9. The

current density of the infinite magnetic line source is $\boldsymbol{J}_m = I_0\delta(z-d)\delta(x)\hat{\boldsymbol{y}}$, with the excited magnetic field given by

$$\boldsymbol{H}(x,z) = \frac{I_0 k_0^2}{j\omega\mu_0}\left[\frac{1}{4j}H_0^{(2)}(k_0\rho)\right]\hat{\boldsymbol{y}} \tag{2.12}$$

where $\rho = \sqrt{x^2+(z-d)^2}$ and $H_0^{(2)}(k_0\rho)$ is the zero order Hankel function of the second kind. The magnetic field at a distance d from the lower interface of the structure can be obtained by a Sommerfeld-type integral as [76]:

$$H_y(x) = \frac{I_0 k_0^2}{j\pi\omega\mu_0}\int_0^\infty \frac{1}{2\gamma_0} e^{-\gamma_0(2d)} T(\omega,k_x)\cos(k_x x)\,dk_x \tag{2.13}$$

where $\gamma_0 = \sqrt{k_x^2 - k_0^2}$ is the propagation constant in free space and $T(\omega,k_x)$ is the transfer function of the structure defined in (2.11).

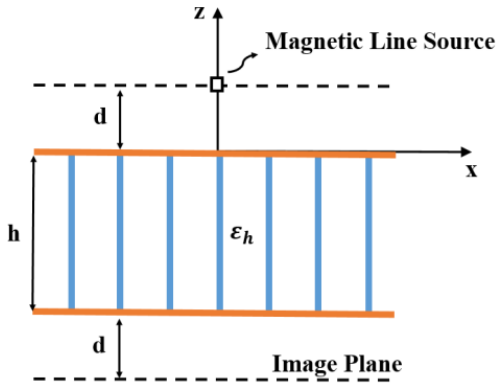

Figure 2.9. Geometry of the WM slab loaded with graphene sheets excited by a magnetic line source placed at a distance d from the upper interface, with the image plane at a distance d from the lower interface.

Figure 2.10 shows the square normalized amplitude of the magnetic field profile calculated at the image plane as a function of x/λ at the operating frequency of $f = 19$ THz. It is assumed that the magnetic line source is located at $d = 150$ nm. The blue solid line has been obtained by

the numerical integration of the Sommerfeld integral in 2.13. According to the HPBW criterion, the resolution is approximately 0.1λ. The dashed line represents the performance of the proposed lens studied by using the electromagnetic simulator CST Microwave Studio and the same resolution is obtained (0.1λ). The black solid line represents the magnetic field profile for the propagation in free space with the resolution of 0.65λ. The resolution of the proposed structure is approximately 6.5 times better than the resolution in free space. The resolution of $\lambda/10$ for the structure has been obtained analytically and verified with the full-wave simulation. At $f = 19$ THz, as shown in Figure 2.6, the enhanced transmission curve is relatively smooth and flat in the range before approaching the first peak ($k_x < 10\ k_0$), which means that the structure transfers the evanescent fields in this range without distortion. The amplitude of the transmission exceeds 1 [$\lg(|T|) = 0$] at the resonance ($k_x = 18\ k_0$) and causes the enhancement of the decaying evanescent wave components. This amplification is helpful to compensate the decaying effect of the air gaps above and below the structure ($2d = 300$ nm).

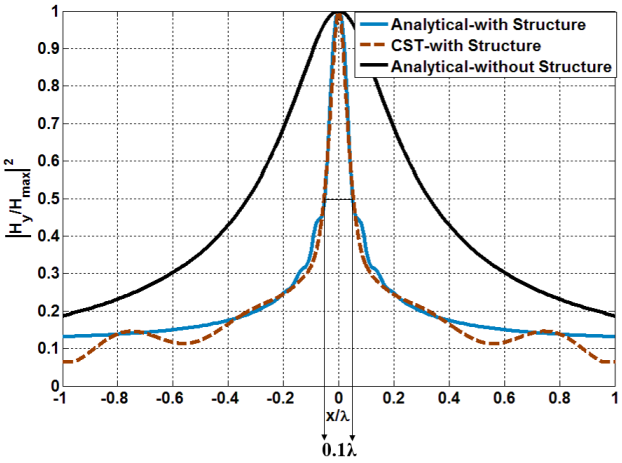

Figure 2.10. The square normalized amplitude of the magnetic field H_y calculated at the image plane for $f = 19$ THz. The black curve represents the field profile when the structure is absent. The blue curve is the field profile in the presence of the structure and the dashed line corresponds to the CST Microwave Studio result.

In the CST Microwave Studio, the magnetic line source is modeled by a current-carrying square loop and the structure is assumed periodic along the y-direction and the width of the slab has been fixed at $2.22\lambda_0$ along the x-direction. The metallic wires are modeled as the copper metals ($\sigma = 5.8 \times 10^7\ ^{\mathrm{S}}/_{\mathrm{m}}$) and the effect of ohmic losses is taken into account. A snapshot of the magnetic field (H_y) in the x-z plane calculated using CST is shown in Figure 2.11 at $f = 19$ THz. The image can be observed at the lower interface of the structure. The resolution of the image is $\lambda/10$ and it is nearly insensitive to the effect of losses.

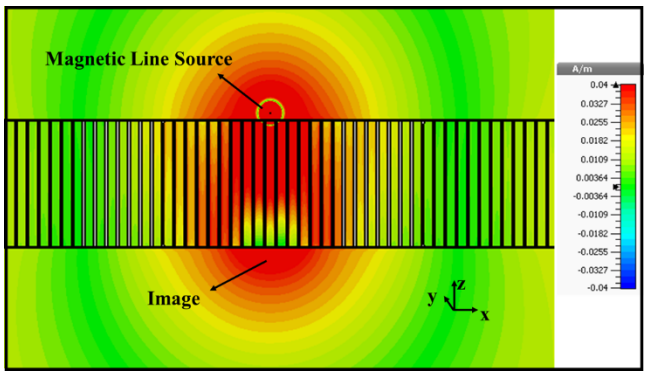

Figure 2.11. CST simulation result for the magnetic field distribution H_y of a WM slab loaded with graphene sheets. The magnetic line source is located at a distance of $d = 150$ nm from the upper interface of the structure and the image plane is located at the same distance from the lower interface.

2.4.2 Double-Slit Source

To obtain a rough estimate of the resolution of the proposed structure, we utilize the double-slit source at a distance d from the upper interface of the structure as shown in Figure 2.12. The double-slit source consists of two subwavelength slits ($2w$) spaced at a distance of $2b$ apart (center to center). As a starting point, we consider a TM-polarized electromagnetic wave, with H_y, E_x,

and E_z components, impinging on the structure. The incident electric field $E_i(k_x)$ and the transmitted electric field $E_t(k_x)$ can be written as [80]

$$\boldsymbol{E}_i(k_x) = e^{-jk_x x + jk_z z}(-k_x\hat{\boldsymbol{z}} - k_z\hat{\boldsymbol{x}}) \tag{2.14}$$

$$\boldsymbol{E}_t(k_x) = Te^{-jk_x x}e^{+jk_z(z+h)}(-k_x\hat{\boldsymbol{z}} - k_z\hat{\boldsymbol{x}}) \tag{2.15}$$

where T is the transmission function of the WM slab loaded with graphene sheets, which is obtained in Sec. 2.2. The electric field of the double-slit source (E_s) can be calculated by [80]

$$\boldsymbol{E}_s = \int_0^{\infty} dk_x v_{k_x} e^{jk_z z}\left(-\hat{z}\cos(k_x x) + \hat{x}\frac{jk_z}{k_x}\sin(k_x x)\right) \tag{2.16}$$

where $v_{k_x} = \left(\frac{4}{\pi k_x}\right)\sin(k_x w)\cos(k_x b)$ is the Fourier component of the aperture. The distribution of the transmitted near field at the image plane can be obtained by the integration of (2.15) with $\frac{v_{k_x}}{k_x}$ over k_x.

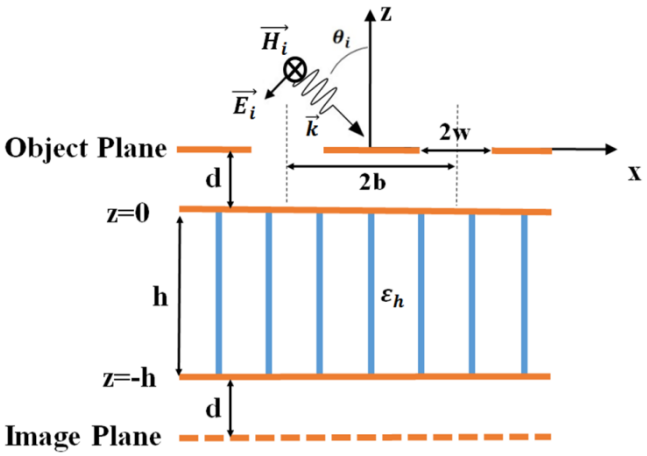

Figure 2.12. Geometry of the WM slab loaded with graphene sheets excited by a double-slit source placed at a distance d from the upper interface, with the image plane at a distance d from the lower interface.

To verify the subwavelength resolution, we study the electric field distribution by means of two narrow slits with $2w = 1000$ nm separated by the distance of $2b = 1500$ nm ($\lambda/10$ for the central operating frequency $f = 20$ THz). Figure 2.13 depicts the normalized electric field intensity distribution calculated at the image plane ($d = 150$ nm) for $f = 18.5$ THz (the lowest proper operating frequency). The black solid line represents the normalized intensity of the electric field for propagation in free space. It is observed that in the absence of the proposed structure, the subwavelength information is lost rapidly with the distance from the source plane and two slits are not resolvable. The field intensity profile at the image plane is depicted by the blue solid line when the structure is present. In the presence of the structure, the image is completely resolved according to the Rayleigh criterion which states that the total intensity at the mid-point of the sum intensity profile of two just-resolved slit source is 81% of the maximum intensity [96]. In Figure 2.13, the dashed and dash-dotted lines represent the imaging performance with and without the proposed lens which are obtained with CST Microwave Studio. It can be clearly seen that there is remarkable agreement between analytical and simulation results.

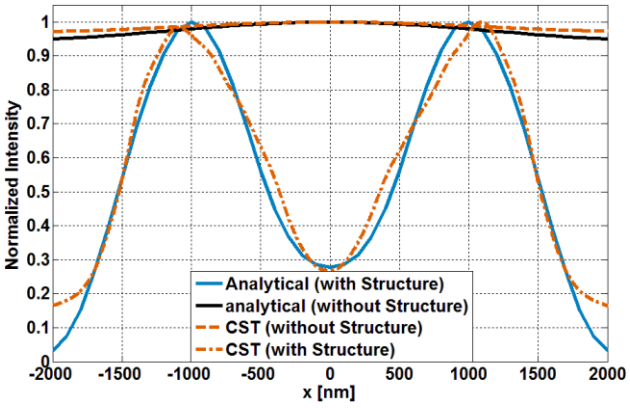

Figure 2.13. The normalized electric field intensity distribution calculated at the image plane for $f = 18.5$ THz. The black curve represents the field profile when the structure is absent. The blue curve is the field profile in the presence of the structure and the dashed and dash-dotted lines correspond to the CST Microwave Studio results.

Unlike other subwavelength imaging devices which have the common restriction of narrow spectral bandwidth and the increase/decrease of the incident wave frequency results in the complete loss of the resolution in the image plane, it is possible to obtain subwavelength imaging in a broad frequency range with no change in the parameters of the structure. In Figure 2.14, we provide the normalized electric field intensity distribution profiles at the image plane in the frequency range from 18 to 22 THz. It is apparent that the resolution of the structure becomes degraded with increasing the frequency. It is worth noting that even in the worst case ($f = 22$ THz), two subwavelength slits can be resolved according to the Rayleigh criterion. Therefore, the proposed structure can cover a wide range of frequencies even if the parameters of the structure are kept the same. Figure 2.14 reveals two important points. First, the position of the maximum intensity is not matched with the position of the slit source center (the shift value is smaller than 1/6 of the slits separation). This shift effect arises from the imperfect property of the transmission function. As shown in Figure 2.8, the transmission magnitude ($|T|$) does not behave uniformly and exceeds unity especially for the frequencies lower than 19 THz, and thus the near field evanescent waves are effectively restored but in a manner of overamplification. This phenomenon would result in the destructive effects for the image profile of a double-slit source such as the large side lobes, the fat profile of the main lobe, and the significant shift of the intensity peak position. Second, as shown in Figure 2.14, an extra bump appears between the two maxima of the intensity profile for $f = 18$ THz. The bump also arises from the imperfect transmission of the evanescent waves with a huge overamplification at the resonance as shown in Figure 2.6. Fortunately, the level of the bump and the shift of maxima as the artifacts of imaging are not significant enough to cause a considerable effect on resolving the two slits at the frequency range $f = 18.5$ to 22 THz.

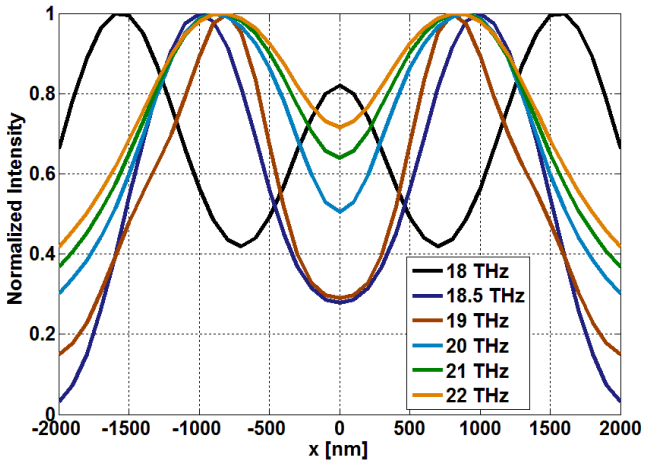

Figure 2.14. The normalized electric field distribution calculated at the image plane for a WM slab loaded with graphene sheets in the range from 18 to 22 THz.

The total electric field distribution of the WM slab loaded with graphene sheets, the isolated WM slab, and two parallel graphene sheets with the following parameters: $a = 215$ nm, $r_0 = 21.5$ nm, $h = 2400$ nm, and $\mu_c = 1.5$ eV, are calculated in the x-z plane by using CST Microwave Studio and are shown in Figure 2.15. Figure 2.15 shows a plane wave with $f = 19$ THz, which is incident on the double-slit source from the left. Figures 2.15(a) and 2.15(b) represent the field distributions in the presence of two graphene sheets and the isolated WM slab, respectively. In these cases, all subwavelength information is lost at a short distance away from the slits. The near fields decay rapidly and the two subwavelength slits are not resolved at the position of the image plane. On the other hand, Figure 2.15(c) illustrates that the WM slab loaded with graphene sheets can effectively transmit the near field information of the source to the image plane and the two subwavelength slits are clearly resolved. The results are consistent with the transmission behaviors of the aforementioned cases in Figure 2.8.

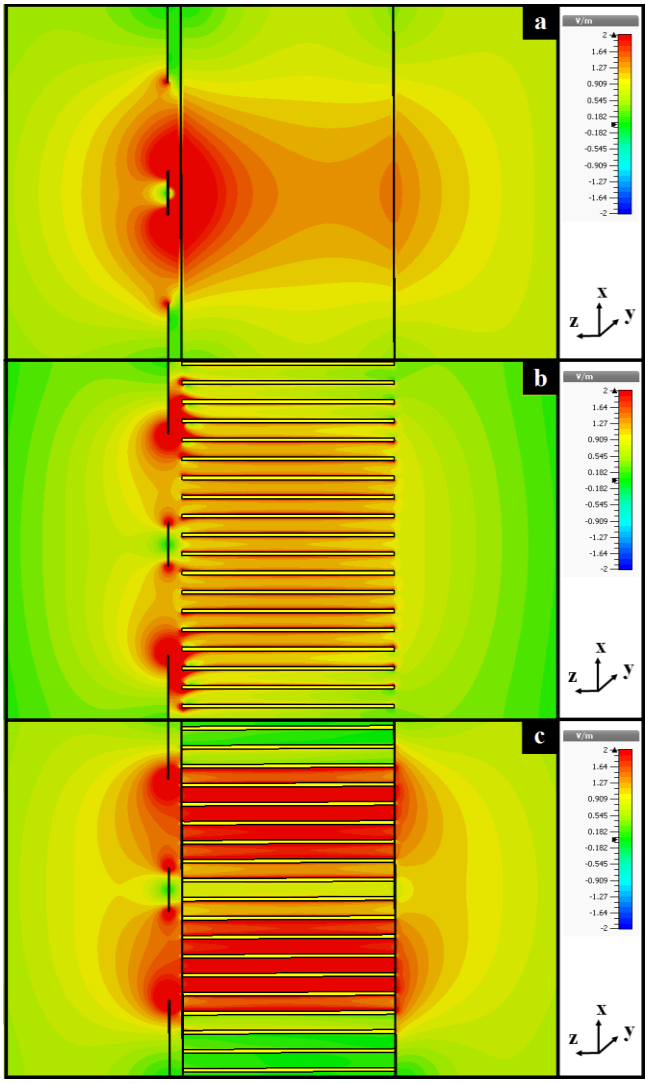

Figure 2.15. CST simulation results for the electric field distribution of (a) two graphene sheets, wherein all subwavelength information is lost and two slits are not resolvable, (b) a WM slab, showing that the subwavelength information is not transmitted to the image plane, and (c) a WM slab loaded with graphene sheets that restores the field distribution from the object plane. The double-slit source is located at a distance of $d = 150$ nm from the upper interface of the structure. Two slits are separated by a distance of $2b = 1500$ nm and the width of the slits is $2a = 1000$ nm.

2.5 Tunable and Broadband Subwavelength Imaging

In this section, we present a possibility of tuning the imaging frequencies of the WM slab loaded with graphene sheets by changing the chemical potential of graphene. As shown in Figure 2.4, the structure's performance depends intensely on the chemical potential of graphene. It is observed that by decreasing the chemical potential, the appropriate operating frequency range, which leads to a high resolution subwavelength imaging, will decrease. For instance, if we change the chemical potential from 1.5 eV to 0.5 eV, the operating frequency range decreases from (18.5-22) THz to (10.5-13) THz.

Here, we investigate a structure with the same parameters as in the previous section except that the graphene's chemical potential is changed from 1.5 eV to 0.5 eV. Figure 2.16 shows the square normalized amplitude of the magnetic field profile calculated at the image plane as a function of x/λ at the operating frequency of 11 THz. We consider $d = 150$ nm and the magnetic line source is placed at $z = 150$ nm. The blue solid line is obtained by the analytical technique at the image plane. The resolution based on the HPBW criterion is 0.065λ. The dashed line shows the full wave simulation result achieved by using CST Microwave Studio and the HPBW resolution is equal to 0.088λ. The black solid line corresponds to the magnetic field propagation in free space with the resolution of 0.38λ. The resolution of the proposed structure improves nearly 5.85 times in comparison to free space. According to HPBW criterion, the resolution of $\lambda/15$ has been obtained analytically and validated by the full-wave simulation. As an important point, it should be mentioned that the better performance of the lens in terms of the resolution in comparison with the case of $\mu_c = 1.5$ eV is because the dispersion curve of the structure has a larger value of $\mathrm{Re}(k_x/k_0)$ at the resonance frequency which leads to the higher and more uniform transmission response.

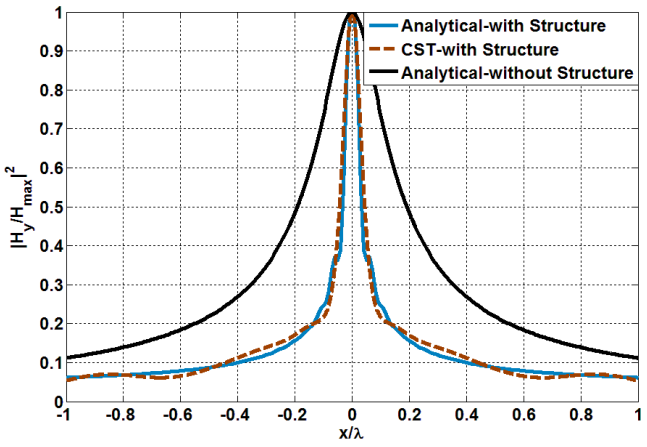

Figure 2.16. The square normalized amplitude of the magnetic field H_y calculated at the image plane for $f = 11$ THz. The black curve represents the field profile when the structure is absent. The blue curve is the field profile in the presence of the structure and the dashed line corresponds to the CST Microwave Studio result.

In addition to the tunability, we investigate the possibility of obtaining subwavelength imaging in a broad frequency range for the proposed structure with $\mu_c = 0.5$ eV and $h = 2400$ nm. In Figure 2.17, the magnetic line source is placed at $d = 150$ nm and the magnetic field profiles are calculated at the image plane in the frequency range from 10.5 to 13 THz. It can be seen that the resolution based on the HPBW criterion is better than $\lambda/7$ in this frequency range. Therefore, the proposed structure can cover a wide range of frequencies with fixed structural parameters.

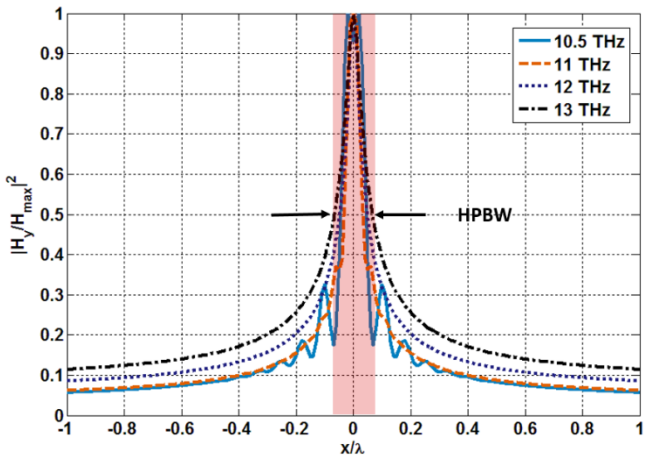

Figure 2.17. Subwavelength imaging performance of a WM slab loaded with graphene sheets (μ_c= 0.5 eV) at different frequencies. The square normalized amplitude of the magnetic field H_y calculated at the image plane located at $d = 150$ nm from the structure in the range from 10.5 to 13 THz.

The proposed structure has a remarkable improvement in comparison to other subwavelength imaging devices such as stacked graphene monolayers, wherein the source and object are positioned in the immediate vicinity of the lens [66], and the WM slab, where the source and image planes are located at a distance $d = a/2$ from the WM [67]-[70]. It is observed that our lens can provide subwavelength imaging even when the source and object planes are placed at distances larger than the lattice constant of the WM slab. For example, here we assume a WM slab loaded with graphene sheets with $\mu_c = 0.5$ eV and $h = 2400$ nm at the operating frequency of $f = 11$ THz. The image/source plane has been considered to be at different distances in the range from $d = 150$ nm to $d = 600$ nm. It should be mentioned that although the distance is increased significantly in comparison to the lattice constant, the resolution of $\lambda/5$ is obtained for $d =$ 600 nm ($d = 2.79a$) as shown in Figure 2.18. In order to obtain a better resolution with the same structure, a stronger amplification of the near field to compensate the exponentially decaying effect

of the air gaps is necessary. This phenomenon can be realized by reducing the frequency. For example, if the magnetic line source is placed at $d = 500$ nm ($d = 2.32a$), the magnetic field profile at the image plane shows the resolution of $\lambda/6.66$ at the operating frequency $f = 10$ THz which is improved in comparison to the resolution of $\lambda/5.55$ at $f = 11$ THz. This result is omitted here for the sake of brevity.

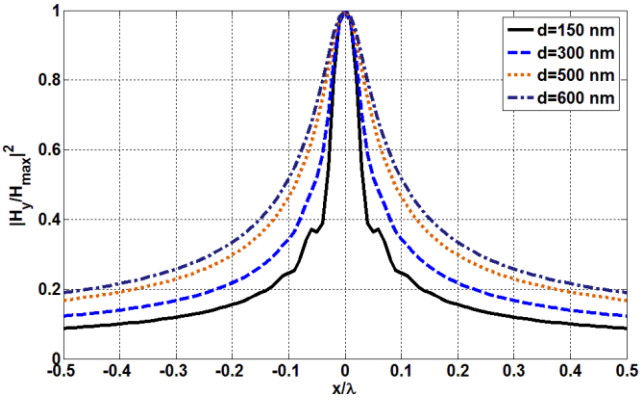

Figure 2.18. Subwavelength imaging performance of a WM slab loaded with graphene sheets (μ_c= 0.5 eV) at different distances of the source and image planes from the structure.

2.6 Fabrication Guide

The investigation on growing of graphene has been a controversial subject for researchers since its discovery in 2003. Two of the recently proposed methods are Chemical Vapor Deposition (CVD) [84] and Epitaxy [85]. As mentioned in [84], the CVD is more desirable from the fabrication point of view, wherein the graphene is grown on a nickel substrate, and then it can be transferred to a silicon-dioxide (SiO_2) substrate. It is worth noting that this transfer process can be applied to any arbitrary substrate (Figure 2.1 in [86]), and the material properties of the graphene will be maintained and depend only on the initial nickel substrate.

It should be emphasized that throughout this paper we have assumed an ideal contact between the graphene and the WM. Additionally, we have assumed that the wires are of identical length. In fact, these two assumptions face with challenges when it comes to a fabrication process. Recently, the joining of nanowires has become a critical issue for device integration and miniaturization [97]. Various joining processes such as welding and soldering have been developed for the formation of the nanowire contacts. However, up to now, it has not been possible to solder or weld a nanowire to a graphene monolayer. In addition, the well-known plasmonic welding only concerns joining two similar plasmonic materials, which is not applicable here.

To avoid the problem with connecting the wires to graphene and a non-uniform wire growth that may occur in the fabrication process, we consider a gap between the wires and the graphene sheets as depicted in Figure 2.19. As an example, we consider a WM slab loaded with graphene sheets with the following parameters: $a = 215$ nm, $r_0 = 21.5$ nm, $\mu_c = 1.5$ eV, $\varepsilon_h = 1$, and $h = 2400$ nm. Figure 2.20 shows the normalized amplitude of the magnetic field profile calculated at the image plane as a function of x/λ at the operating frequency of $f = 19$ THz for different values of the gap ($g = 0, 10, 15$, and 25 nm). The magnetic line source is located at $d = 150$ nm from the upper side of the structure. The solid blue line represents the performance of the structure for an ideal contact between the nanowires and the graphene sheets, and the resolution of the structure is $\lambda/10$. By increasing the gap up to 10 nm, the strong coupling between the surface plasmons of the graphene sheets and the WM leads to a subwavelength imaging with high resolution and low distortion as shown in Figure 2.20. The response of the structure for $g = 10$ nm is shown by the brown star symbols. Further increase in the gap size causes a significant distortion in subwavelength imaging, wherein remarkable side lobes appear in the magnetic field distribution at the image plane. This phenomenon arises due to strongly confined surface plasmons

on graphene sheets, which consequently avoids the strong coupling between the surface plasmons of graphene and the WM slab for larger gaps.

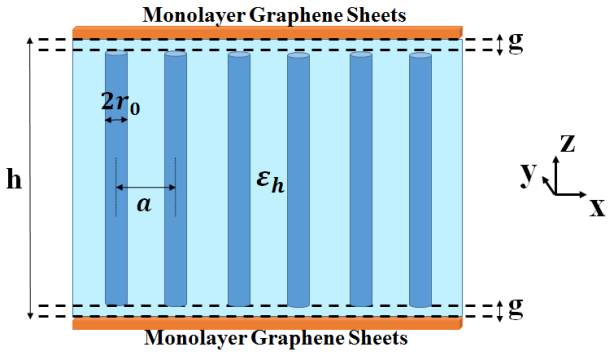

Figure 2.19. Schematics of a WM slab embedded in a dielectric slab with the permittivity of ε_h loaded with graphene sheets which are placed at a distance of g (gap size) on the upper and lower interfaces of the structure.

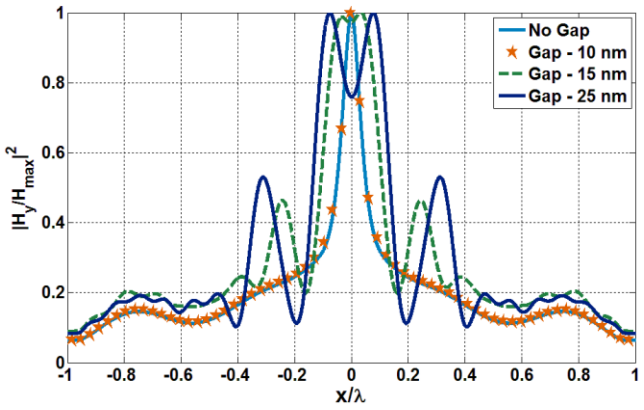

Figure 2.20. The square normalized amplitude of the magnetic field H_y calculated at the image plane located at $d = 150$ nm from the structure at the operating frequency of $f = 19$ THz for different values of gap ($g = 0, 10, 15$, and 25 nm).

In addition, in order to clarify qualitatively the effect of the gap on the imaging performance of the lens, snapshots of the magnetic field in the x-z plane calculated using CST Microwave

Studio are shown in Figure 2.21 at $f = 19$ THz for different values of the gap size. It can be observed that for $g = 10$ nm [Figure 2.21(a)], the results are promising and consistent with those for the ideal contact case [Figure 2.11]. The magnetic field distributions for $g = 15$ nm and $g = 25$ nm, which are shown in Figures 2.21(b) and 2.21(c), respectively, confirm the deterioration effect with the increase of the gap size.

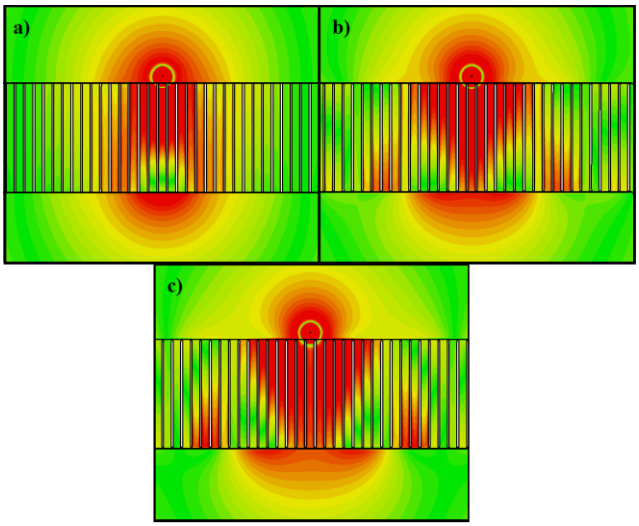

Figure 2.21. CST simulation results for the magnetic field distribution H_y of a WM slab loaded with graphene sheets for different values of the gap size, (a) $g = 10$, (b) $g = 15$, and (c) $g = 25$ nm.

It is worth mentioning that if the wires are embedded in a dielectric slab such as silicon-dioxide, the fabrication of the lens becomes easier in a way that the gap allows the graphene to be attached to the substrate and avoids a direct connection of wires to graphene. This also relaxes the requirements on the wires, as it is only important that the wires do not protrude from the substrate. Our study shows that for a WM slab loaded with graphene sheets with the following parameters: $a = 215$ nm, $r_0 = 21.5$ nm, $\mu_c = 1.5$ eV, and $h = 2400$ nm, by embedding the wires in a dielectric with the permittivity of $\varepsilon_h = 4$, the dispersion relation of the structure with the ideal

contact shifts to lower frequencies and subwavelength imaging can be obtained at the frequencies around $f = 9.8$ THz with the resolution of $\lambda/8.334$. According to our study, it has been concluded that the required gap size to restore the fine details of the source at the image plane will be $g = 1$ nm, which is smaller than that of the WM in the air due to the fast damping of the surface plasmons of the graphene in the dielectric spacer medium, which prevents the adequate surface plasmon coupling of the graphene sheets and the WM slab. The results are omitted here for the sake of brevity.

CHAPTER III

TUNABLE DUAL-BAND SUBWAVELENGTH IMAGING WITH A WIRE MEDIUM SLAB LOADED WITH NANOSTRUCTURED GRAPHENE METASURFACES

3.1 Introduction

The resolution of the conventional imaging systems is restricted by the natural diffraction limit. In order to overcome this limitation, various kinds of subdiffraction near-field imaging mechanisms have been proposed. One well-known solution is to use a metamaterial lens with negative refractive index property. In 1968, Veselago theoretically pointed out a novel kind of electromagnetic materials with simultaneously negative permeability and permittivity, known as negative index materials (NIM) [47]. Following this idea, Pendry proposed a class of "perfect lenses". Pendry realized that a NIM slab, with the relative parameters ε=-1 and μ=-1, not only focus the propagating waves, but also amplify the exponentially decaying evanescent waves of a source field [48]. The NIM lens is far from being implemented into the imaging devices due to the high sensitivity to the energy dissipation and loss (the imaginary part of ε and μ) [98]. Thus, the term "super lens" is used for the lenses such as the plasmonic silver film [49], [99], the magneto-inductive lens [100], and the swiss-roll structure [101] which take this practical limit into account. Super lenses can recover the subwavelength information through evanescent enhancement; unfortunately, such lenses are restricted by an extremely short working distance between the source, lens, and image, and have a narrow resonant frequency range.

These subwavelength imaging lenses have important potential biomedical and microelectronics applications in sub-diffraction microscopy, lithography, tomography, sensing, and nondestructive characterization of materials [50]-[55].

Indeed, the Pendry's subwavelength imaging process physically arises at the lens interfaces, and not within the metamaterials volume. Therefore, it is also possible to utilize a pair of resonant grids, conjugate sheets, and metasurfaces which can support surface-wave modes (surface plasmon-polaritons) instead of a bulk material [56]-[59].

Graphene as a two dimensional material with unique electronic, mechanical, and optical properties [39], [60], [61] has been employed for different metamaterial applications [62]-[65]. In contrast to the above mentioned metamaterials, graphene is widely tunable by the change of graphene's electrochemical potential via chemical doping, magnetic field, and electrostatic gating [39]. Recently, Ref. [66] presented a frequency tunable graphene lens, in which the enhancement of evanescent waves for subwavelength imaging is realized by the well-coupled surface plasmons supported by the graphene sheets. It should be noted that the performance of lens intensely depends on the distance between graphene sheets and the resolution reduces rapidly when the thickness of the lens is increased.

Another approach which is based on the canalization principle was proposed in [67]-[70]. A slab of WM with the thickness equal to an integer number of half wavelength is capable of transforming both the evanescent and propagating harmonics into the transmission-line modes along the wires. The loss sensitivity of this structure is remarkably small and the resolution is restricted only by the periodicity of the wires. This technique has been theoretically predicted and confirmed experimentally in [69], [82]. It has been shown that due to the employment of metal,

the properties of this lens cannot be tuned after fabrication and the lens has narrow spectral bandwidth.

It has been shown that the periodic array of graphene nanopatches, unlike the uniform graphene monolayer which is intrinsically inductive [6], has dual capacitive/inductive properties in the low-THz spectrum [30]. The required capacitive/inductive reactance of GNM can be obtained by a proper selection of the gap, array periodicity, and Fermi energy level of graphene. Here, this unique property of GNM is exploited to design a dual-band subwavelength imaging device. At lower THz frequencies the behavior of the GNM is similar to that of the metallic patches (capacitive) [76] and at higher THz frequencies it behaves similar to graphene monolayer (inductive). We show that a WM slab loaded with GNMs has the advantages of widely tunable subwavelength imaging and the possibility of obtaining image even if the distance between GNMs is significant fraction of wavelength. The principle of operation of our lens is based on the enhancement of evanescent waves which is provided by the coupling of the surface plasmons at the lower and upper interfaces. The WM slab has a remarkable effect on the strong coupling and waveguiding of evanescent waves to the other side of the structure.

In order to analyze the transmission/reflection properties of the WM slab loaded with GNMs, a nonlocal homogenization model is utilized [74], [75], wherein the WM is modeled as a uniaxial anisotropic material characterized by a nonlocal dielectric function with a generalized additional boundary condition (GABC) at the connection of wires to graphene. The subwavelength imaging resolution of a structure can be assessed by various techniques. Here, we employ two well-known methods to evaluate the imaging properties of the proposed structure. The performance of the lens is studied in the presence of the double-slit and magnetic line sources, and the resolution is quantified by using the half-power beamwidth (HPBW) [76] and the Rayleigh

[77]-[81] criteria. The analytical results are validated with the full-wave electromagnetic simulator, CST Microwave Studio [46], showing good agreement.

The practical realization of the proposed lens has several challenges. First, the synthesis of a large area continuous graphene film with mono-dispersity and large charge carrier mobility faces with severe problems such as inevitable flocculation and coalescence. Recently, various methods have been proposed to achieve a graphene monolayer with the lowest imperfection such as Exfoliation [102], Chemical Vapor Deposition (CVD) [84] and Epitaxy [85]. Second, the graphene should be fabricated in a form of nanoscale patches. Ref. [103] presents a novel method in direct synthesis of large-scale graphene films using CVD on thin nickel layers, and patterning the films and transferring them to arbitrary substrates. Also, recent advances in pattering of graphene has been studied in [104]-[107]. Third, the process of joining the WM to the intensely thin GNM deals with some obstacles due to the fact that the well-known methods such as ohmic contact, soldering, plasmonic welding are not applicable in the proposed structure. To overcome this limitation, here we show that a small gap between the GNM and the WM does not change the response of the lens because of the strong coupling of the surface plasmons of the GNMs and the WM slab. This approach has been studied by the full-wave simulation in CST Microwave Studio, which confirms this claim.

This chapter is organized as follows: In Section 3.2, we present the closed-form expressions for the reflection and the transmission coefficients of the WM slab loaded with GNMs based on the nonlocal homogenization model. The dispersion behavior of odd and even modes and the transmission response of the structure are studied in Section 3.3. In Section 3.4, the performance of the proposed lens is analyzed in the presence of the magnetic line source and the double-slit source. The critical challenges in the practical realization of the lens have been discussed, and a

promising approach in order to overcome these obstacles has been proposed in Section 3.5. The conclusion is drawn in Section 3.6. A time dependence of the form $e^{j\omega t}$ is assumed and suppressed.

3.2 Nonlocal Model for WM with Graphene Nanopatches

As shown in Figure 3.1, we consider a WM slab loaded with two-dimensional (2D) GNM [with a typical geometry as depicted in Figure 3.1(c)] illuminated by a TM polarized uniform plane wave obliquely incident at an angle θ_i. In this structure, D is the period of the patches and wires, g is the gap between the patches, r_0 is the radius of the wires, ε_h is the permittivity of the dielectric slab, and h is the thickness of the structure. The metallic wires are oriented along the z-direction and two GNMs are located at $z = 0$ and $z = -h$. To determine the transmission/reflection response of the structure with a TM plane-wave excitation, the even/odd excitation mode technique is utilized. By considering the perfect electric conductor (PEC) and the perfect magnetic conductor (PMC) at the center of the wires ($z = -h/2$), the even and odd responses of the structure can be obtained, respectively. Figure 3.1(b) demonstrates the cross-section view in the presence of PEC/PMC symmetries.

In our analytical model, the two GNMs are treated as impedance sheets, whereas the WM slab is modeled as a uniaxial anisotropic material characterized by a nonlocal effective dielectric function along the wires $\varepsilon_{zz} = \varepsilon_h\left[1 - k_p^2/(k_h^2 - k_z^2)\right]$, where $k_h = k_0\sqrt{\varepsilon_h}$ is the wave number of the host medium, $k_0 = \omega/c$ is the free space wave number, ω is the angular frequency, c is the speed of light, k_z is the z-component of the wave vector $\vec{k} = (k_x, 0, k_z)$, and k_p is the plasma wave number as $k_p = \sqrt{(2\pi/a^2)/(\ln(a/2\pi r_0) + 0.5275)}$ [76].

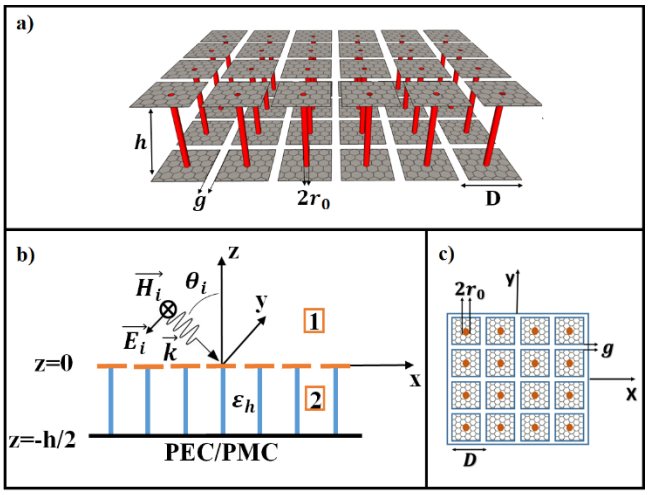

Figure 3.1. Schematics of a WM slab loaded with GNMs: (a) 3D view, (b) cross-section view of the structure by considering PEC/PMC at the symmetry plane, and (c) top view.

A TM-polarized plane wave excites both TEM and the extraordinary TM modes in the homogenized WM slab. First, it is assumed that the PEC plane is located at $z = -h/2$. The total magnetic fields in the air region above the structure (region 1) and in the WM slab (region 2), as shown in Figure 3.1(b), can be written as follows:

$$H_y^{(1)} = (e^{\gamma_0 z} + R_{\text{even}} e^{-\gamma_0 z}) e^{-jk_x x}$$

$$H_y^{(2)} = (A_{\text{TM}}^{+} e^{\gamma_{\text{TM}}\, z} + A_{\text{TM}}^{-} e^{-\gamma_{\text{TM}}\, z} + B_{\text{TEM}}^{+} e^{\gamma_{\text{TEM}}\, z} + B_{\text{TEM}}^{-} e^{-\gamma_{\text{TEM}}\, z}) e^{-jk_x x} \quad (3.1)$$

where $A_{\text{TM}}^{\pm}$ and $B_{\text{TEM}}^{\pm}$ are the amplitudes of the extraordinary TM and transmission-line TEM modes in the WM slab and R_{even} is the reflection coefficient of the even-mode excitation. The propagation constant in free space is $\gamma_0 = \sqrt{k_x^2 - k_0^2}$ and k_x is the x-component of the wave vector $\vec{k} = (k_x, 0, k_z)$. The value of γ_0 is purely imaginary if $k_x = k_0 \sin\theta_i$ (propagating mode in free space), and it becomes real valued if $k_x > k_0$ (evanescent modes in free space). Therefore, the distribution of the electromagnetic field in region 1 can include both the spatial harmonics of propagating plane waves and evanescent modes (the subwavelength spatial spectrum). In (3.1), the

propagation constants of the TEM and TM modes are $\gamma_{\mathrm{TEM}} = jk_h = jk_0\sqrt{\varepsilon_h}$ and $\gamma_{\mathrm{TM}} = \sqrt{k_p^2 + k_x^2 - k_0^2}$. In order to determine the unknown coefficients (R_{even}, $A_{\mathrm{TM}}^{\pm}$, and $B_{\mathrm{TEM}}^{\pm}$), the two-sided impedance boundary conditions are satisfied at the GNM interface ($z = 0$):

$$E_x^{(1)}\Big|_{z=0^+} = E_x^{(2)}\Big|_{z=0^-} = Z_g[\, H_y^{(2)}\Big|_{z=0^-} - H_y^{(1)}\Big|_{z=0^+}] \tag{3.2}$$

where Z_g is the surface impedance of the GNM and given by [30], [31]:

$$Z_g = R_s + jX_s = \frac{D}{\sigma_s(D-g)} - j\frac{\pi}{2D\omega\varepsilon_0\left(\frac{\varepsilon_h+1}{2}\right)\ln\left[\csc\left(\frac{\pi g}{2D}\right)\right]}\,. \tag{3.3}$$

In (3.3), R_s is the surface resistance per unit cell related to the conduction losses, X_s is the surface reactance per unit cell, and σ_s is the graphene's complex surface conductivity modeled with the Kubo formula using closed-form expressions for the interband (σ_{inter}) and intraband (σ_{intra}) contributions [60]:

$$\sigma_{\mathrm{intra}} = -j\frac{k_B e^2 T}{\pi\hbar^2(\omega - j\tau^{-1})}\left(\frac{\mu_c}{Tk_B} + 2\ln\left(e^{-\frac{\mu_c}{Tk_B}} + 1\right)\right)$$

$$\sigma_{\mathrm{inter}} \approx \frac{je^2}{4\pi\hbar}\ln\left(\frac{2|\mu_c| - \omega\hbar}{2|\mu_c| + \omega\hbar}\right)$$

$$\sigma_s = \sigma_{\mathrm{intra}} + \sigma_{\mathrm{inter}}. \tag{3.4}$$

In (3.4), $\hbar$ is reduced Plank's constant, e is the electron charge, k_B is Boltzmann's constant, τ is the relaxation time, T is the temperature, and μ_c is the chemical potential. It should be mentioned that in the low-THz region and below the interband transition threshold, $\hbar\omega < 2|\mu_c|$, σ_{intra} dominates over σ_{inter} [60]. As an example, Fig. 2 shows the imaginary part of the surface impedance of a free-standing GNM in air as a function of frequency with the following structural parameters: $D = 215$ nm, $g = 21.5$ nm, $\varepsilon_h = 1$, $\tau = 0.5$ ps, and $\mu_c = 0.5, 1,$ and 1.5 eV. The

surface impedance of GNM changes from capacitive to inductive as the frequency increases. It can be seen that when the imaginary part of surface impedance, Im(Z_s), has a negative value, the GNM behaves as a capacitive reactive surface similar to the metallic patches, and the GNM acts as an inductive reactive surface like a metallic mesh-grid and graphene monolayer when Im(Z_s) has a positive value. In addition, by employing the tunability property of graphene, the frequency at which the transition from capacitive to inductive surface impedance occurs for GNM can be tuned via the chemical potential even if the other structural parameters are kept the same. This tunability and dual property of GNM are the motivation to present a tunable dual-band imaging device. In this study, it is assumed that $T = 300$ K, $\varepsilon_h = 1$, $\tau = 0.5$ ps, $D = 215$ nm, and $r_0 = 21.5$ nm. In all following results, the full graphene interband and intraband conductivities are considered.

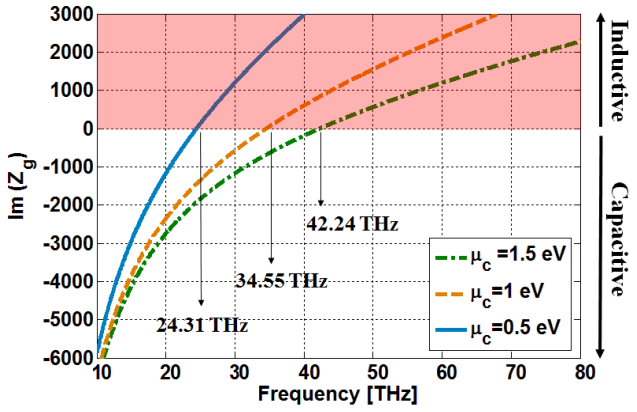

Figure 3.2. Imaginary part of the surface impedance, Im(Z_s), of a free-standing GNM with different chemical potentials in the range from 0.5 to 1.5 eV.

At the PEC interface ($z = -h/2$), we assume that $(1/\varepsilon_h)(dH_y/dz) = 0$ which is equivalent to impose that the tangential electric field vanishes at the PEC plane. Furthermore, it has been shown for the case wherein the WM is connected to the perfect electric conductor, an

additional boundary condition (ABC) is required [87]-[91]. The microscopic ABC which is enforced at the PEC ground plane ($z = -h/2^{+}$) can be written for the wire current, $I(z)$, as [92]:

$$\frac{dI(z)}{dz}\Big|_{z\,=\,(-h/2)^{+}} = 0 \tag{3.5}$$

and in terms of macroscopic fields:

$$\frac{\partial}{\partial z}\left(k_0\varepsilon_h E_z^{(2)} + k_z\eta_0 H_y^{(2)}\right)\Big|_{z\,=\,(-h/2)^{+}} = 0. \tag{3.6}$$

In addition, it requires the use of GABC for the microscopic current at the connection of wires to graphene at $z = 0^{-}$ [74], [75]:

$$\left[\frac{\sigma_s}{j\omega\varepsilon_0\varepsilon_h}\frac{dI(z)}{dz} + I(z)\right]\Big|_{z\,=\,0^{-}} = 0 \tag{3.7}$$

and in terms of macroscopic fields:

$$\left(1 + \frac{\sigma_s}{j\omega\varepsilon_0\varepsilon_h}\frac{\partial}{\partial z}\right)\left(k_0\varepsilon_h E_z^{(2)} + k_z\eta_0 H_y^{(2)}\right)\Big|_{z\,=\,0^{-}} = 0. \tag{3.8}$$

By enforcing the aforementioned boundary conditions, the closed-form expression of the reflection coefficient for PEC symmetry (R_{even}) can be obtained by [74], [75]

$$R_{\text{even}} = \frac{\frac{N_{\text{even}}}{D_{\text{even}}}\coth\left(\gamma_{\text{TM}}\frac{h}{2}\right)\cot\left(k_h\frac{h}{2}\right) - \left(\frac{1}{\gamma_0} + j\frac{\eta_0}{Z_g k_0}\right)}{\frac{N_{\text{even}}}{D_{\text{even}}}\coth\left(\gamma_{\text{TM}}\frac{h}{2}\right)\cot\left(k_h\frac{h}{2}\right) + \left(\frac{1}{\gamma_0} - j\frac{\eta_0}{Z_g k_0}\right)},$$

$$N_{\text{even}} = \left(\frac{1}{\varepsilon_{zz}^{\text{TM}}} - 1\right)\left(\frac{\sigma_s\gamma_{\text{TM}}}{j\omega\varepsilon_0\varepsilon_h}\tanh\left(\gamma_{\text{TM}}\frac{h}{2}\right) + 1\right) + \left(1 - \frac{\sigma_s k_h}{j\omega\varepsilon_0\varepsilon_h}\tan\left(k_h\frac{h}{2}\right)\right),$$

$$D_{\text{even}} = -\frac{k_h}{\varepsilon_h}\left(\frac{1}{\varepsilon_{zz}^{\text{TM}}} - 1\right)\left(\frac{\sigma_s\gamma_{\text{TM}}}{j\omega\varepsilon_0\varepsilon_h} + \coth\left(\gamma_{\text{TM}}\frac{h}{2}\right)\right) + \frac{\gamma_{\text{TM}}}{\varepsilon_h}\left(\cot\left(k_h\frac{h}{2}\right) - \frac{\sigma_s k_h}{j\omega\varepsilon_0\varepsilon_h}\right). \tag{3.9}$$

The closed-form expression of the reflection coefficient for the PMC symmetry (R_{odd}) can be derived by using a similar approach:

$$R_{\text{odd}} = \frac{\frac{N_{\text{odd}}}{D_{\text{odd}}}\tanh\left(\gamma_{\text{TM}}\frac{h}{2}\right)\tan\left(k_h\frac{h}{2}\right) - \left(\frac{1}{\gamma_0} + j\frac{\eta_0}{Z_g k_0}\right)}{\frac{N_{\text{odd}}}{D_{\text{odd}}}\tanh\left(\gamma_{\text{TM}}\frac{h}{2}\right)\tan\left(k_h\frac{h}{2}\right) + \left(\frac{1}{\gamma_0} - j\frac{\eta_0}{Z_g k_0}\right)},$$

$$N_{\text{odd}} = \left(\frac{1}{\varepsilon_{zz}^{\text{TM}}} - 1\right)\left(\frac{\sigma_s\gamma_{\text{TM}}}{j\omega\varepsilon_0\varepsilon_h}\coth\left(\gamma_{\text{TM}}\frac{h}{2}\right) + 1\right) + \left(1 + \frac{\sigma_s k_h}{j\omega\varepsilon_0\varepsilon_h}\cot\left(k_h\frac{h}{2}\right)\right),$$

$$D_{\text{odd}} = +\frac{k_h}{\varepsilon_h}\left(\frac{1}{\varepsilon_{zz}^{\text{TM}}} - 1\right)\left(\frac{\sigma_s\gamma_{\text{TM}}}{j\omega\varepsilon_0\varepsilon_h} + \tanh\left(\gamma_{\text{TM}}\frac{h}{2}\right)\right) + \frac{\gamma_{\text{TM}}}{\varepsilon_h}\left(\tan\left(k_h\frac{h}{2}\right) + \frac{\sigma_s k_h}{j\omega\varepsilon_0\varepsilon_h}\right) \quad (3.10)$$

where $\varepsilon_{zz}^{\text{TM}} = \varepsilon_h k_x^2/(k_p^2 + k_x^2)$ is the relative effective permittivity for TM polarization. The results can be validated by considering the limiting case of $\sigma_s \to 0$. In this case, (3.9) and (3.10) turn to the WM slab expressions derived in [91]. The transmission/reflection response of the structure (shown in Figure 3.1(a)) can be obtained by the superposition principle as follows:

$$R = \frac{1}{2}(R_{\text{even}} + R_{\text{odd}}) \quad (3.11)$$

$$T = \frac{1}{2}(R_{\text{even}} - R_{\text{odd}}). \quad (3.12)$$

3.3 Parametric study of Dispersion and Transmission Properties

In order to determine the appropriate operating frequency regime wherein the enhancement of evanescent waves leads to the recovering of the source details at the image plane, we study the dispersion behavior of the TM^x surface waves and the transmission response of the WM slab

loaded with GNMs. The ultimate goal is designing a subwavelength imaging lens with a high resolution and low distortion properties.

The dispersion relation of the lens can be obtained by applying the perfect electric conductor (PEC) and perfect magnetic conductor (PMC) planes at $z = -h/2$ [as shown in Figure 3.1(b)]. The response of the structure for even excitation can be achieved by finding the complex roots of the dispersion function [denominator of the reflection coefficient, R_{even}, in (3.9)]. Similarly, the response of the structure for the odd excitation can be obtained from the reflection coefficient, R_{odd}, in (3.10). At lower THz frequencies, the GNM behaves as a capacitive reactive surface. The significant resonance of the structure is associated with the even modes, and thus, we restrict our analysis to the modes obtained with the PEC symmetry. Conversely, the functionality of GNM changes to the inductive at higher THz frequencies. As a result, the significant resonances correspond to the odd modes and we study only the modes which are obtained with the PMC symmetry. Figure 3.3 shows the dispersion behavior of the normalized propagation constant (k_x/k_0) of the odd/even TM^x modes of the WM slab loaded with GNMs with the following structural parameters: $\mu_c = 0.5$ eV and $h = 2400$ nm. At low frequencies ($f < 20$ THz), the real part of (k_x/k_0) for the proper bound forward mode (the solid brown line) is close to 1 and the imaginary part has a negligibly small negative value, indicating that the proper complex bound mode (surface plasmon) interacts weakly with the WM slab and propagates primarily in the air region in the vicinity of graphene sheet. In this regime, the real part of the proper bound backward mode (the solid blue line) has extremely large value and the imaginary part has a negligibly small positive value. This mode is highly dispersive and strongly interacts with the structure (the field is primarily concentrated below the GNM in the wire medium). At the frequencies around 22.8 THz stopband occurs for the first TM^x surface bound mode. In the same way, the propagation of the

second TM^x surface bound mode, which corresponds to the PMC symmetry, stops at the frequencies near 25.9 THz.

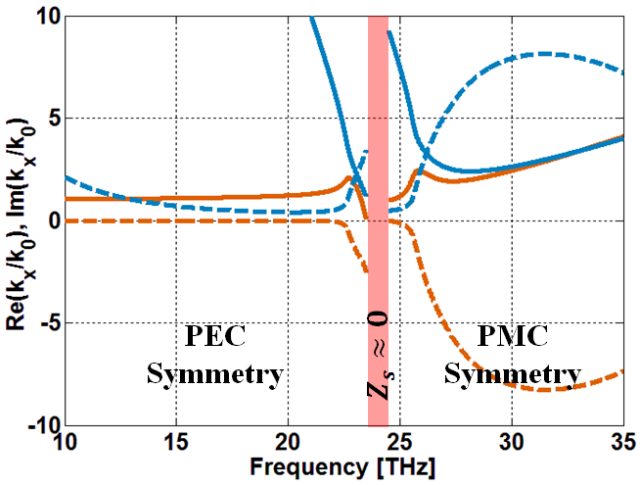

Figure 3.3. Dispersion behavior of the even/odd modes of a WM slab loaded with GNMs (μ_c= 0.5 eV and $h = 2400$ nm). The solid line represents the real part of the normalized propagation constant, Re(k_x / k_0), and the dashed line represents the imaginary part of the normalized propagation constant, Im(k_x / k_0).

It should be mentioned that the strong enhancement of the evanescent waves ideally can be obtained when the dispersion response of the structure becomes maximally flat at the operating frequency. Physical mechanism behind this condition can be described as the efficient coupling of evanescent waves with larger wave vectors to the surface modes which causes the resonant interaction. It can be shown that the turning point (the frequency at which the forward and backward waves become near to each other) to some extent has the required conditions for the subwavelength imaging with low distortion and high resolution. In order to validate this claim, we utilize the transmission response of the device as a function of wave vector k_x/k_0 which can provide more quantitative and detailed information about the structure's performance in

subwavelength imaging [93]. The behavior of the transmission coefficient is sensitive to the variations in the operating frequency. Therefore, the transmission magnitude $|T|$ as a function of $\mathrm{Re}(k_x/k_0)$ is calculated at different frequencies of operation and depicted in Figure 3.4. At $f = 22.8$ THz and 25.9 THz, $|T|$ has a smooth behavior which exceeds unity and leads to amplification of the near field in the range $1 < \mathrm{Re}(k_x/k_0) < 4$. On the other hand, at the frequencies of 22 THz and 25 THz, $|T|$ has two transmission peaks which are not beneficial, due to the lower transmission between the poles. In addition, the observed resonant enhancement deteriorates the subwavelength imaging since some of the spatial harmonics are amplified by a large factor. By a careful study of the dispersion relation and the transmission coefficient, it can be concluded that the appropriate frequencies for subwavelength imaging are 22.8 THz and 25.9 THz for the aforementioned parameters. In Section 3.4, we investigate the validity of this claim.

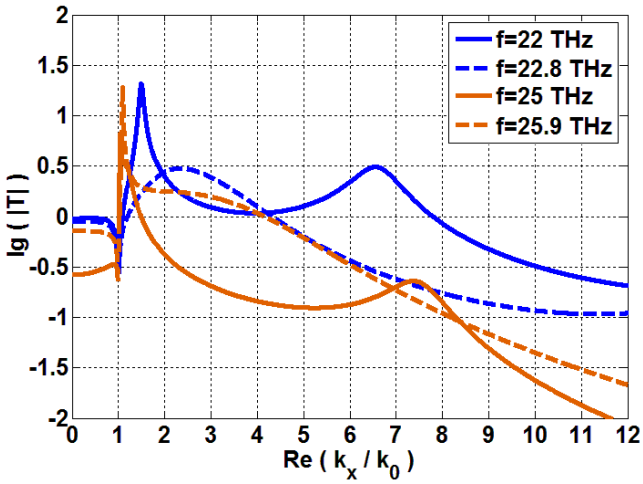

Figure 3.4. Magnitude of the transmission coefficient as a function of $\mathrm{Re}(k_x/k_0)$ calculated for the structure at different operating frequencies ($f = 22, 22.8, 25$, and 25.9 THz).

In contrast to the other well-known subwavelength imaging devices which operate at single carefully selected frequency and cannot be tuned after fabrication, this lens has large tunability with respect to the chemical potential as shown in Figure 3.2. Therefore, the presence of graphene

provides more degrees of freedom regarding the operating frequency. It is observed that by increasing the chemical potential, the frequency in which the imaginary part of the surface reactance of the GNM is equal to zero, increases to higher frequencies. The chemical potential can be largely tuned either passively by doping the profile (density and type of carriers) or chemical/structural surface modification, or actively by an external static electric field or magnetic field [60]. Figure 3.5 shows the dispersion behavior of the normalized propagation constant (k_x/k_0) of the odd/even TM^x modes of the WM slab loaded with GNMs with the following structural parameters: $\mu_c = 1.5$ eV and $h = 2400$ nm. It can be seen that by changing the chemical potential from 0.5 eV to 1.5 eV, the operating frequencies increase to 33.5 THz and 43.88 THz, respectively.

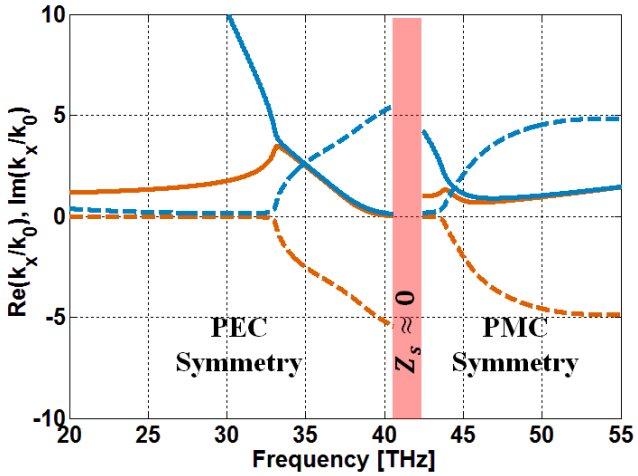

Figure 3.5. Dispersion behavior of the even/odd modes of a WM slab loaded with GNMs (μ_c= 1.5 eV and $h = 2400$ nm). The solid line represents the real part of the normalized propagation constant, Re(k_x / k_0), and the dashed line represents the imaginary part of the normalized propagation constant, Im(k_x / k_0).

It is worth noting that by decreasing the length of the lens, the overall dispersion behavior does not change drastically. However, the first and second stopbands will shift to the higher frequencies. For example, by changing the length from 2400 nm to 1200 nm, the operating frequencies change to 38 THz and 46.85 THz (the chemical potential is assumed as $\mu_c = 1.5$ eV).

At lower THz frequencies the dispersion behavior of WM slab loaded with GNMs is similar to some extent to that of WM slab loaded with metallic patch arrays which is studied in details in [76]. As shown in Figure 3.3, the forward and backward modes do not join each other at the turning point. This phenomenon is taken place due to the presence of loss in graphene. In [76], the metallic patch arrays are assumed ideally lossless. Therefore, the forward and backward branches are connected at the turning point. On the other hand, at higher THz frequencies, there are significant differences between the dispersion behavior of the proposed lens and the WM slab loaded with graphene monolayer sheets. These differences occur as a result of the presence of GNMs which leads to the propagation of backward wave and the dispersion curve does not become maximally flat at the left bound of the stopband for the proper complex mode.

3.4 Study of Resolution

In this section, we employ two widely used approaches to investigate the imaging properties of the structure. First, we placed an infinite magnetic line source at a distance from the upper interface of the structure, and calculated the magnetic field distribution at the same distance from the lower interface. The resolution of the lens is quantified by the HPBW criterion [76]. In the second approach, the performance of the lens is assessed by a double-slit source and then interpreted by the Rayleigh criterion [77]-[81].

3.4.1 Magnetic Line Source

In order to characterize the resolution of the lens, we consider an infinite magnetic line source directed along the y-direction and located at a distance d from the upper interface of the lens. This distance is chosen typically less than $\lambda_0/8$, where λ_0 is the free-space wavelength. Therefore, the impinging evanescent waves can effectively interact with the structure and lens can recover fine details of the source through evanescent enhancement. The geometry is shown in Figure 3.6. The current density of this two-dimensional infinite magnetic line source is $\boldsymbol{J}_m = I_0\delta(z-d)\delta(x)\hat{\boldsymbol{y}}$, with the excited magnetic field given by

$$\boldsymbol{H}(x,z) = \frac{I_0 k_0^2}{j\omega\mu_0}\left[\frac{1}{4j}H_0^{(2)}(k_0\rho)\right]\hat{\boldsymbol{y}} \tag{3.13}$$

where $H_0^{(2)}(k_0\rho)$ is the zero-order Hankel function of the second kind and $\rho = \sqrt{x^2+(z-d)^2}$. The magnetic field at the image plane (distance d from the lower interface of the structure) when the slab illuminated by the source can be expressed by a Sommerfeld-type integral as [76]:

$$H_y(x) = \frac{I_0 k_0^2}{j\pi\omega\mu_0}\int_0^\infty \frac{1}{2\gamma_0} e^{-\gamma_0(2d)} T(\omega,k_x)\cos(k_x x)\,dk_x \tag{3.14}$$

where $\gamma_0 = \sqrt{k_x^2 - k_0^2}$ is the propagation constant in free space and $T(\omega,k_x)$ is the transfer function of the structure defined in (3.12). It should be mentioned that the structure is assumed unbounded in the x and y directions.

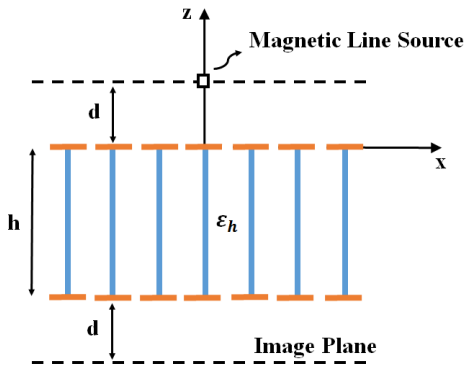

Figure 3.6. Geometry of the WM slab loaded with GNMs excited by a magnetic line source placed at a distance d from the upper interface, with the image plane at a distance d from the lower interface.

Figures. 3.7(a) and 3.7(b) show the square normalized amplitude of the magnetic field H_y calculated at the image plane as a function of x/λ at the operating frequencies of 22.8 THz and 25.9 THz, respectively. It is assumed that the magnetic line source is located at $d = 150$ nm. In Figures. 3.7(a) and 3.7(b), the blue solid lines have been obtained by the numerical integration of the Sommerfeld integral in (3.14) and the half-power beamwidths (HPBWs) are equal to 0.12λ and 0.16λ. The brown dashed lines represent the performance of the proposed lens which is studied by using electromagnetic simulator CST Microwave Studio and according to the HPBW criterion, the resolutions are approximately 0.1λ ($f = 22.8$ THz) and 0.14λ ($f = 25.9$ THz). The black solid lines represent the magnetic-field profile for the propagation in free space and the HPBWs are equal to 0.74λ ($f = 22.8$ THz) and 0.84λ ($f = 25.9$ THz). Therefore, the resolution better than $\lambda/6$ for both dual operating bands has been obtained analytically and verified with the full-wave simulation.

As shown in Figure 3.4, although the amplitude of the transmission slightly exceeds 1 [$\lg(|T|) = 0$] in the range of $1 < \mathrm{Re}(k_x/k_0) < 4$ at the operating frequencies of 22.8 THz and 25.9

THz, the total behavior of the transmission curve is relatively smooth and flat which means that the structure transfers the evanescent fields in this range without distortion. This insignificant amplification is helpful to compensate the decaying effect of the air gaps above and below the structure ($2d = 300$ nm).

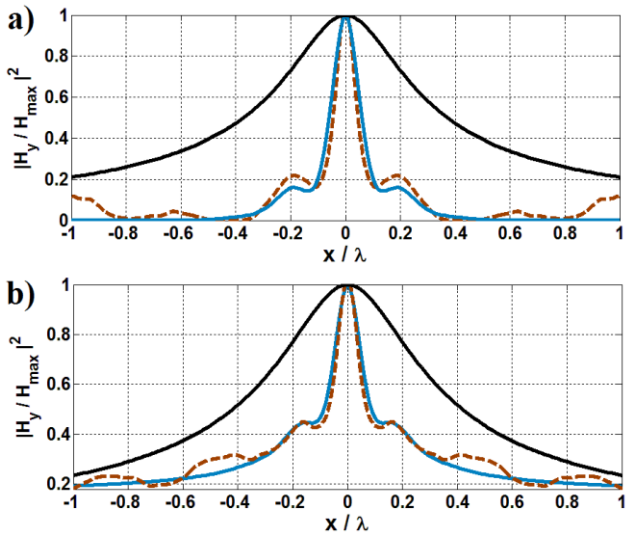

Figure 3.7. The square normalized amplitude of the magnetic field H_y calculated at the image plane for (a) $f = 22.8$ THz and (b) $f = 25.9$ THz. The black curve represents the field profile when the structure is absent. The blue curve is the field profile in the presence of the structure and the dashed line corresponds to the CST Microwave Studio result.

In the CST Microwave Studio, the magnetic line source is modeled by a current-carrying square loop and the structure is assumed periodic along the y-direction. The width of the slab has been fixed at $2.45\lambda_0$ (at the operating frequency of $f = 22.8$ THz) along the x-direction. The metallic wires are modeled as the copper metals ($\sigma = 5.8 \times 10^7$ S/m) and the effect of ohmic losses is taken into account. A snapshot of the distribution of magnetic field H_y in the x-z plane calculated using CST is depicted in Figures. 3.8(a) and 3.8(b) for $f = 22.8$ THz and 25.9 THz. The image is formed at the lower interface of the structure and the resolution of the proposed

structure is approximately 5 times better than in free space for both of the operating frequencies. The resolution of the image is nearly insensitive to the effect of losses. Figure 3.8 clearly shows the canalization of the near field along the wires. The slight quantitative disagreement between the analytical and simulation results in Figure 3.7 arises due to the fact that the structure is considered finite in the x-direction in the CST simulation and the reflection of surface waves at the edges of the structure leads to side lobe artifacts in the subwavelength imaging.

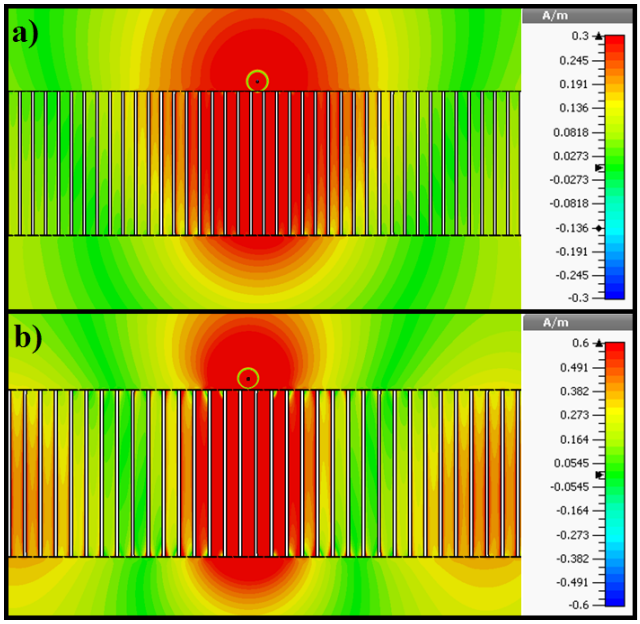

Figure 3.8. CST simulation result for the magnetic field distribution H_y of a WM slab loaded with GNMs at (a) $f = 22.8$ THz and (b) $f = 25.9$ THz. The magnetic line source is located at a distance of $d = 150$ nm from the upper interface of the structure and the image plane is located at the same distance from the lower interface.

3.4.2 Double-Slit Source

The double-slit technique has been typically utilized to estimate the resolution of subwavelength imaging devices. In this method, the resolution of lens corresponds to the minimum

possible distance for which a distinct image of two subwavelength slits can be resolved. As sketched in Figure 3.9, the double-slit source which is placed at a distance d from the upper interface of the structure consists of two subwavelength slits ($2w$) with the center to center separation of $2b$.

We consider a TM-polarized plane wave, with H_y, E_x, and E_z components, impinging on the structure. The incident electric field $E_i(k_x)$ and the transmitted electric field $E_t(k_x)$ can be written as [80]

$$\boldsymbol{E}_i(k_x) = e^{-jk_x x + jk_z z}(-k_x\hat{\boldsymbol{z}} - k_z\hat{\boldsymbol{x}}) \tag{3.15}$$

$$\boldsymbol{E}_t(k_x) = Te^{-jk_x x}e^{+jk_z(z+h)}(-k_x\hat{\boldsymbol{z}} - k_z\hat{\boldsymbol{x}}) \tag{3.16}$$

where T is the transmission function of the WM slab loaded with nanostructured graphene metasurfaces, which is obtained in Section 3.2. The electric field of the double-slit source (E_s) can be obtained by [80]

$$\boldsymbol{E}_s = \int_0^\infty dk_x v_{k_x} e^{jk_z z}\left(-\hat{z}\cos(k_x x) + \hat{x}\frac{jk_z}{k_x}\sin(k_x x)\right) \tag{3.17}$$

where $v_{k_x} = \left(\frac{4}{\pi k_x}\right)\sin(k_x w)\cos(k_x b)$ is the Fourier component of the aperture. The distribution of the transmitted near field at the image plane can be obtained by the integration of (3.16) with $\frac{v_{k_x}}{k_x}$ over k_x.

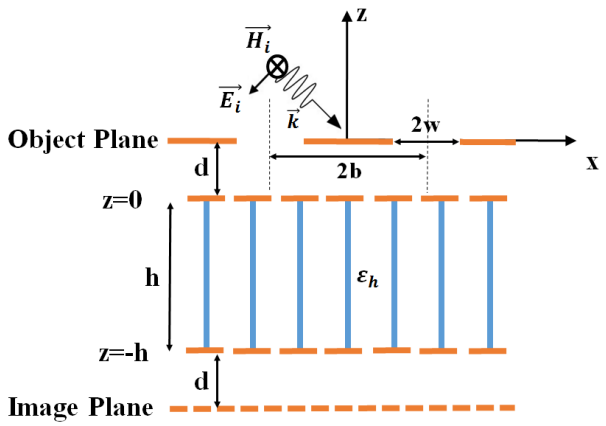

Figure 3.9. Geometry of the WM slab loaded with GNMs excited by a double-slit source placed at a distance d from the upper interface, with the image plane at a distance d from the lower interface.

To verify the subwavelength resolution, we study the electric field distribution by means of two narrow slits with $2w = 500$ nm separated by the distance of $2b = 2000$ nm (in terms of wavelength, $\lambda/6.57$ at $f = 22.8$ THz and $\lambda/5.79$ at $f = 25.9$ THz). Figure 3.10 depicts the normalized electric field intensity distribution calculated at the image plane ($d = 150$ nm) for $f =$ 22.8 THz and 25.9 THz. The field intensity profile at the image plane is depicted by the solid blue and dash-dotted brown lines when the structure is present and the operating frequencies are $f =$ 22.8 THz and 25.9 THz, respectively. In the presence of the structure, the image is completely resolved according to the Rayleigh criterion which states that the total intensity at the mid-point of the sum intensity profile of two just-resolved slit source is 81% of the maximum intensity [86]. Figure 3.10 reveals that the resolution of the structure is better than $\lambda/6.57$ at the operating frequency of $f = 22.8$ THz and it is greater than $\lambda/5.79$ at the operating frequency of $f = 25.9$ THz.

By a careful study, it can be concluded that when the separation of two slits is chosen $2b =$ 1820 nm, the Rayleigh criterion is satisfied and the resolution is $\lambda/7.23$ at the operating frequency of 22.8 THz. In addition, the proper separation for fulfillment of Rayleigh criterion is $2b =$ 1600

nm at the operating frequency of $f = 25.9$ THz, thus, the resolution is equal to $\lambda/7.24$. Figure 3.11 shows the normalized electric field intensity distribution calculated at the image plane ($d = 150$ nm) for $f = 22.8$ THz and 25.9 THz when the separation of the slits is chosen 1820 nm and 1600 nm. These results confirm the resolution which is obtained by employing the magnetic line source.

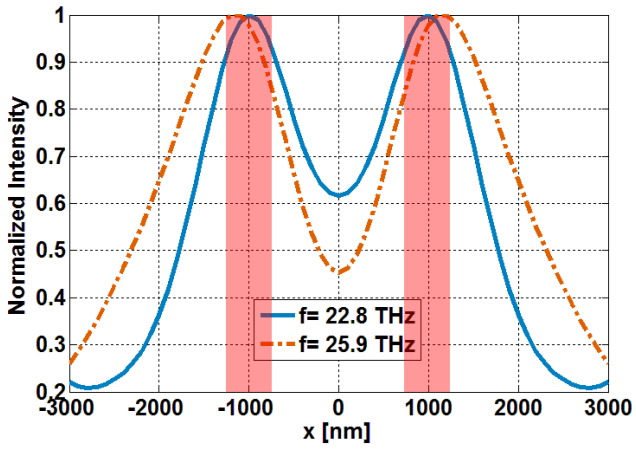

Figure 3.10. The normalized electric field intensity distribution calculated at the image plane for $f = 22.8$ THz and 25.9 THz. The structural parameters of the double-slit source are $2w = 500$ nm, $2b = 2000$ nm, $d = 150$ nm. The red bars demonstrate the positions of slits.

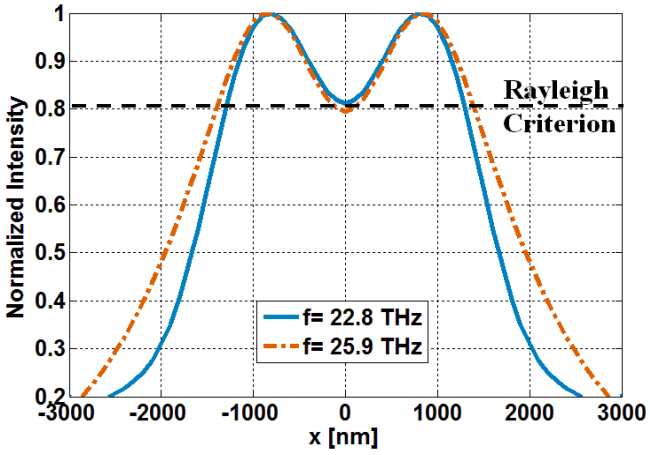

Figure 3.11. The normalized electric field intensity distribution calculated at the image plane for $f = 22.8$ THz and 25.9 THz when the separation of the slits is chosen 1820 nm and 1600 nm.

3.5 Fabrication Guide

Graphene is a two-dimensional carbon crystal that has become one of the most controversial topics of research in the last few years. Although the theoretical studies on the graphene have been done for decades, it was first produced and isolated in 2005 [108]. The recent studies on the growth of an ideal graphene monolayer with the lowest number of defects and highest electron mobility lead to several well-known production techniques which are presented in Refs. [84-86], [107]. In particular, Ref. [84] reported a simple approach to fabricate relatively high quality of a sheet of graphene in large scale via CVD on the nickel substrate. In CVD, the substrate is exposed by one or more gas molecules (Argon gas and methane). The carbon in methane has reacted with the nickel substrate and during a cooling process, diffuses out of the nickel to form the graphene film. CVD is more preferable from the fabrication point of view due to the remarkable advantages of imperviousness and high purity. Furthermore, the possibility of transferring the CVD growth graphene film to any arbitrary substrate is discussed in [86].

In addition, for the practical configuration of the proposed lens, the GNM should be manufactured by precisely patterning the graphene monolayer. It has been shown that the graphene is conformable to diverse patterning schemes which result in interesting properties. The patterned graphene has the capability to be used in various applications such as transparent electrodes, field effect transistors, biosensors and energy devices. The recent progresses in graphene's patterning have been studied in Refs. [103-107]. In this paper, we utilized the dual capacitive/inductive property of graphene which is synthesized in form of nanoscale graphene patches for designing a tunable dual-band subwavelength imaging device.

It should be emphasized that an ideal contact between the GNMs and the WM slab is assumed throughout this paper. It has been shown that the recent advances in joining of nanowires

such as soldering, welding, and mechanical bonding [97] cannot be applied for connection of nano wires to graphene. In addition, the plasmonic welding only concerns joining two similar plasmonic materials, which is not applicable in the proposed lens. The other implicit assumption which is considered in the analytical approach in Section 3.2 is that the wires are supposed to be with identical length. These two hypotheses face with challenges when it comes to a fabrication process.

In order to surmount the obstacles in connecting the wires to graphene and a non-uniform wire growth which may occur in the fabrication process, we consider a gap between the wires and the GNMs as sketched in Figure 3.12. As an example, we consider a WM slab loaded with GNMs with the following parameters: $D = 215$ nm, $g = 21.5$ nm, $r_0 = 21.5$ nm, $\mu_c = 0.5$ eV, $\varepsilon_h = 1$, and $h = 2400$ nm.

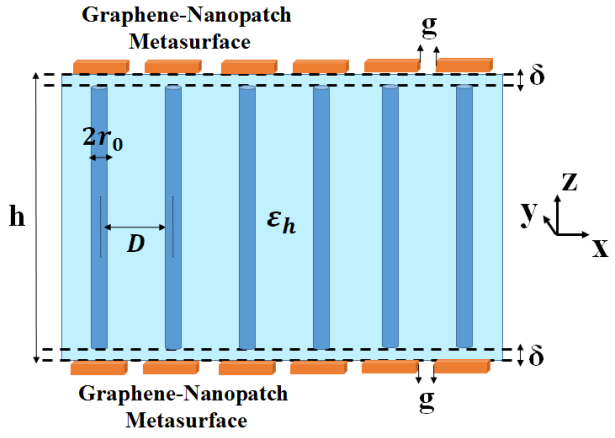

Figure 3.12. Schematics of a WM slab embedded in a dielectric slab with the permittivity of ε_h loaded with GNMs which are placed at a distance of δ (gap size) on the upper and lower interfaces of the structure.

Figure 3.13 shows the normalized amplitude of the magnetic field profile calculated at the image plane as a function of x/λ at the operating frequency of $f = 22.8$ THz for different values of the gap ($\delta = 0, 5, 7.5$, and 10 nm). The magnetic line source is located at $d = 150$ nm from the

upper side of the structure. The dashed blue line represents the performance of the lens for an ideal contact between the nanowires and the GNMs, and the resolution of the structure is $\lambda/10$ (as shown in Figure 3.7(a)). By increasing the gap up to 5 nm, the strong coupling between the surface plasmons of the GNMs and the WM ameliorates the deterioration effect of the gap and leads to a subwavelength imaging with high resolution ($>\lambda/8$) and low distortion. The response of the structure for $\delta = 5$ nm is shown by the solid black line in Figure 3.13 and it behaves similar to the blue dashed line when an ideal connection ($\delta = 0$ nm) is considered. Further increase in the gap size causes a significant distortion in subwavelength imaging, wherein large side lobes and fat profile of the main lobe appear in the magnetic field distribution at the image plane. This phenomenon arises due to the fact that the gap prevents the efficient coupling between the surface plasmons of GNMs and the WM slab.

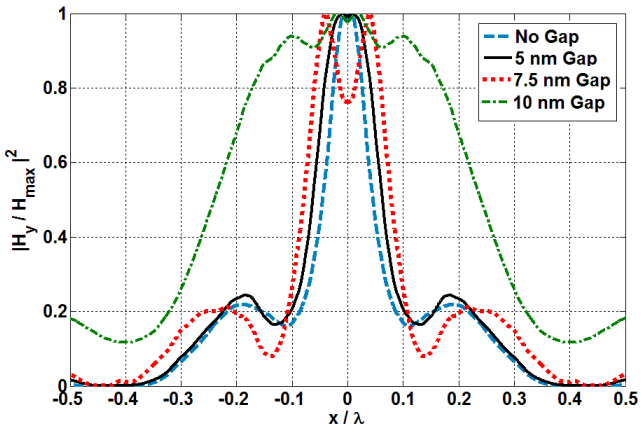

Figure 3.13. The square normalized amplitude of the magnetic field H_y calculated at the image plane located at $d = 150$ nm from the structure at the operating frequency of $f = 22.8$ THz for different values of gap ($\delta = 0, 5, 7.5$, and 10 nm).

As shown in Figure 3.13, the gap has a substantial effect on the performance of the lens, in such a way that it is not possible to obtain a low distorted image at the same operating frequency

when the gap size is larger than 5 nm. The supplementary studies on the effects of gap have been shown that by increasing the gap size the proper operating frequency for subwavelength imaging slightly shifts to the lower frequencies. This frequency shift phenomenon is not valid for the considerably large gap ($\delta \geq 10$ nm) because of a weak coupling between the surface plasmons of GNMs and the WM slab. Figure 3.14 shows the normalized amplitude of the magnetic field profile calculated at the image plane as a function of x/λ for different gap sizes ($\delta = 0, 5,$ and 7.5 nm) at the slightly changed frequencies. The black solid line represents the response of the structure for $\delta = 5$ nm. It can clearly be seen that the resolution of the lens is improved and has a less disagreement with the ideal contact of the WM slab and GNMs ($\delta = 0$ nm). Also, the result for the gap size, $\delta = 7.5$ nm, is shown by the dotted red line at the operating frequency of $f = 22.3$ THz. In this case, the result proves the claim that by a 0.5 THz shift in the operating frequency, the source details can be refined at the image plane without remarkable distortion and high resolution.

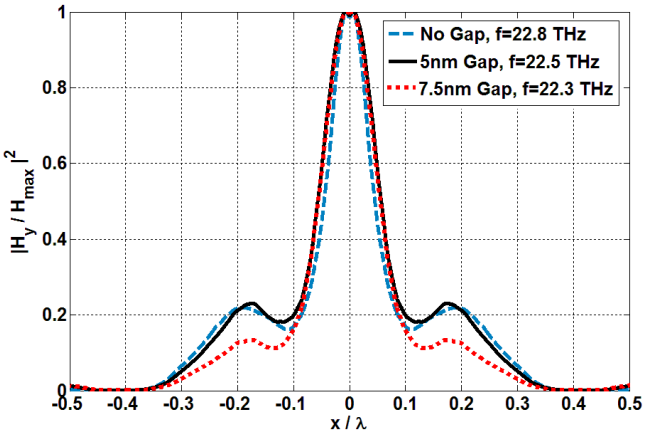

Figure 3.14. The square normalized amplitude of the magnetic field H_y calculated at the image plane located at $d = 150$ nm from the structure for different values of gap ($\delta = 0, 5,$ and 7.5 nm) at the slightly changed frequencies.

CONCLUSION

Graphene has been attracting a great deal of attention in the past decade due to its outstanding promising applications. In the first chapter, we proposed an analytical method to cloak a finite conducting wedge with an arbitrary opening angle by a cylindrically shaped nanostructured graphene metasurface. The required surface reactance for cloaking the conducting wedge with various opening angles can be obtained by tuning graphene's chemical potential. It is observed that the cylindrically shaped mantle cloak can effectively suppress the total scattering width of several concentric electromagnetically coupled conducting wedges. In addition, we proposed an alternative method for cloaking a finite conducting wedge with a wedge shaped metasurface cloak. Due to the advantages of the maximum scattering cancellation and low capacitive reactance, this approach gives the possibility of obtaining cloak even if the radius of the conducting wedge is larger than $\lambda/10$.

In the second chapter, a possibility of subwavelengh imaging by a WM slab loaded with graphene sheets is investigated. It has been shown that the presence of graphene provides significant flexibility in designing a subwavelength imaging device at THz frequencies. The physical mechanism behind the operation of our lens is based on the enhancement of evanescent waves. The presence of wires improves the strong coupling of the surface plasmons supported by the upper and lower interfaces of the structure. This lens not only has the advantages of operating in a wideband region due to graphene's tunability and low loss sensitivity, but also has the possibility of increasing the structure's thickness. In addition, the source/image plane can be located at a distance larger than the lattice constant of the WM slab. The severe challenges in the

implementation of the proposed lens have been investigated and a promising approach in order to overcome those difficulties has been proposed. As an extension of this study, the performance of WM slab loaded with nanostructured graphene metasurfaces as a novel subwavelength imaging device is studied in the third chapter. It has been shown that the presence of graphene patch arrays provides significant flexibility in designing a tunable dual-band subwavelength imaging device. The results are studied analytically and validated against the full-wave numerical results obtained with CST Microwave Studio.

LIST OF REFERENCES

[1] Alù and N. Engheta, "Cloaked near-field scanning optical microscope tip for noninvasive near-field imaging," *Phys. Rev. Lett.*, vol. 105, no. 26, pp. 263906, Dec. 2010.

[2] F. Bilotti, S. Tricarico, F. Pierini, and L. Vegni, "Cloaking apertureless near-field scanning optical microscopy tips," *Optics Lett.*, vol. 36, no. 26, pp. 211–213, Jan. 2011.

[3] Alù and N. Engheta, "Cloaking a sensor," *Phys. Rev. Lett.*, vol. 102, pp. 233901, Jun. 2009.

[4] D. H. Kwon and D. H. Werner, "Restoration of antenna parameters in scattering environments using electromagnetic cloaking," *Appl. Phys. Lett.*, vol. 92, no. 11, pp. 113507, Mar. 2008.

[5] M. Farhat, C. Rockstuhl, and H. Bağcı, "A 3D tunable and multi-frequency graphene plasmonic cloak," *Opt. Express,* vol. 21, no. 10, pp. 12592-12603, 2013.

[6] P. Y. Chen and A. Alù, "Atomically thin surface cloak using graphene monolayers," *ACS Nano*, vol. 5, no. 7, pp. 5855–5863, Jul. 2011.

[7] I. F. Akyildiz and J. M. Jornet, "The internet of nano-things," *IEEE Wireless Communications,* vol. 17, no. 6, pp. 58-63, 2010.

[8] J. B. Pendry, D. Schurig, and D. R. Smith, "Controlling electromagnetic fields," *Science*, vol. 312, no. 5781, pp. 1780–1782, Jun. 2006.

[9] U. Leonhardt, "Optical conformal mapping," *Science*, vol. 312, no. 5781, pp. 1777–1780, Jun. 2006.

[10] D. Schurig, J. J. Mock, B. J. Justice, S. A. Cummer, J. B. Pendry, A. F. Starr, and D. R. Smith, "Metamaterial electromagnetic cloak at microwave frequencies," *Science*, vol. 314, no. 5801, pp. 977–980, Nov. 2006.

[11] J. Li and J. B. Pendry, "Hiding under the carpet: A new strategy for cloaking," *Phys. Rev.*

Lett., vol. 101, p. 203901, 2008.

[12] Z. Ruan, M. Yan, C. W. Neff, and M. Qiu, "Ideal cylindrical cloak: Perfect but sensitive to tiny perturbations," *Phys. Rev. Lett.*, vol. 99, no. 11, pp. 113903, Sep. 2007.

[13] R. Fleury and A. Alù, "Cloaking and invisibility: A review," *Forum for Electromagnetic Research Methods and Application Technologies (FERMAT)*, vol. 1, no. 7, pp. 1-24. 2014.

[14] A. Alù and N. Engheta, "Achieving transparency with plasmonic and metamaterial coatings," *Phys. Rev. E*, vol. 72, no. 1, pp. 016623, Jul. 2005.

[15] B. Edwards, A. Alù, M. E. Young, M. Silveirinha, and N. Engheta, "Experimental verification of Epsilon-Near Zero metamaterial coupling and energy squeezing using a microwave waveguide," *Phys. Rev. Lett.*, vol. 100, no. 3, pp. 033903, Jan. 2008.

[16] A. Alù, D. Rainwater, and A. Kerkhoff, "Plasmonic cloaking of cylinders: finite length, oblique illumination and cross-polarization coupling," *New J. Phys.*, vol. 12, no. 10, pp. 103028, Oct. 2010.

[17] A. Alù and N. Engheta, "Cloaking and transparency for collections of particles with metamaterial and plasmonic covers," *Opt. Express*, vol. 15, no. 12, pp. 7578–7590, Jun. 2007.

[18] A. Alù and N. Engheta, "Plasmonic and metamaterial cloaking: physical mechanisms and potentials," *J. Opt. A: Pure Appl. Opt.*, vol. 10, no. 9, pp. 093002, Sep. 2008.

[19] A. Alù and N. Engheta, "Effects of size and frequency dispersion in plasmonic cloaking," *Phys. Rev. E*, vol. 78, no. 4, p. 045602, Oct. 2008.

[20] F. Bilotti, S. Tricarico, and L.Vegni, "Plasmonic metamaterial cloaking at optical frequencies," *IEEE Trans. Nanotech.*, vol. 9, no. 1, pp. 55–61, 2010.

[21] A. Monti, F. Bilotti, and A. Toscano, "Optical cloaking of cylindrical objects by using covers

made of core-shell nanoparticles," *IEEE Trans. Nanotech.*, vol. 9, no. 1, pp. 55–61, 2010.

[22] A. Monti, F. Bilotti, A. Toscano, and L. Vegni, "Possible implementation of epsilon-near-zero metamaterials working at optical frequencies," *Opt. Commun.*, vol. 285, pp. 3412–3418, 2012.

[23] A. Alù, "Mantle cloak: Invisibility induced by a surface," *Phys. Rev. B*, vol. 80, no. 24, pp. 245115, Dec. 2009.

[24] P. Y. Chen and A. Alù, "Mantle cloaking using thin patterned metasurfaces," *Phys. Rev. B*, vol. 84, no. 20, pp. 205110, Nov. 2011.

[25] Y. R. Padooru, A. B. Yakovlev, P. Y. Chen, and A. Alù, "Analytical modeling of conformal mantle cloaks for cylindrical objects using sub-wavelength printed and slotted arrays," *J. Appl. Phys.*, vol. 112, no. 3, pp. 034907, Aug. 2012.

[26] Y. R. Padooru, A. B. Yakovlev, P. Y. Chen, and A. Alù, "Line-source excitation of realistic conformal metasurface cloaks," *J. Appl. Phys.*, vol. 112, no. 10, pp. 104902, Nov. 2012.

[27] P. Y. Chen, F. Monticone, and A. Alù, "Suppressing the electromagnetic scattering with an helical mantle cloak," *IEEE Antennas Wireless Propag. Lett.*, vol. 10, pp. 1598–1601, 2011.

[28] P. Y. Chen, C. Argyropoulos, and A. Alù, "Broadening the cloaking bandwidth with non-foster metasurfaces," *Phys. Rev. Lett.*, vol. 111, p. 233001, 2013.

[29] Z. H. Jiang and D. H. Werner, "Exploiting metasurface anisotropy for achieving near-perfect low-profile cloaks beyond the quasi-static limit," *J. Phys. D: Appl. Phys.*, vol. 46, p. 505306, 2013.

[30] Y. R. Padooru, A.B. Yakovlev, C. S. R. Kaipa, G. W. Hanson, F. Medina, and F. Mesa, "Dual capacitive-inductive nature of periodic graphene patches: Transmission characteristics at low-

THz frequencies," *Phys. Rev. B*, vol. 87, pp. 115401, 2013.

[31] P. Y. Chen, J. Soric, Y. R. Padooru, H. M. Bernety, A. B. Yakovlev, and A. Alù, "Nanostructured graphene metasurface for tunable terahertz cloaking, " *New. J. Phys*., vol. 15, pp. 123029, 2013.

[32] C. A. Balanis, *Advanced engineering electromagnetics*, New York: Wiley, 1989.

[33] P. Y. Ufimtsev, *Fundamentals of the physical theory of diffraction*, John Wiley & Sons, 2014.

[34] F. Hacivelioglu, L. Sevgi, and P. Y. Uiimtsev, "Electromagnetic wave scattering from a wedge with perfectly reflecting boundaries: Analysis of asymptotic techniques," *IEEE Antennas Propag. Mag.,* vol. 53, no. 3, pp. 232-253, 2011.

[35] R. Ross and M. A. K. Hamid, "Scattering by a wedge with rounded edge," *IEEE Trans. Antennas Propag.,* vol. 19, no. 4, pp. 507-516, 1971.

[36] W. G. Lim and J. W. Yu, "Scattering by a dielectric-loaded conducting wedge with concaved edge: TE case," *Prog. Electromag. Res.*, vol. 89, pp. 85-100, 2009.

[37] L. I. Klinkenbusch, "Two-dimensional scattering of a plane wave by a finite wedge," *Arch. für Elektrotech.*, vol. 75, no. 4, pp. 261-269, 1992.

[38] A. Y. Shepilko and Y. V. Shepilko, "Scattering of a plane electromagnetic wave by a metal-dielectric composite cylinder," *Int. Conf. on Mathematical Methods in Electromagnetic Theory (MMET)*, vol. 2, pp. 474–476, 2000.

[39] G. W. Hanson, "Dyadic Green's functions and guided surface waves for a surface conductivity model of graphene," *J. Appl. Phys.*, vol. 103, pp. 064302, 2008.

[40] H. Yan, T. Low, W. Zhu, Y. Wu, M. Freitag, X. Li, F. Guinea, P. Avouris, and F. Xia,

"Damping pathways of mid-infrared plasmons in graphene nanostructures," *Nature Photonics*, vol. 7, pp. 394-399, 2013.

[41] M. Jablan, H. Buljan, and M. Soljačić, "Plasmonics in graphene at infrared frequencies," *Phys. Rev. B*, vol. 80, p. 245435, 2009.

[42] C. Berger, Z. Song, X. Li, X. Wu, N. Brown, C. Naud, D. Mayou, T. Li, J. Hass, A. N. Marchenkov, E. H. Conrad, P. N. First, W. A. de Heer, "Electronic confinement and coherence in patterned epitaxial graphene," *Science*, vol. 312, pp. 1191-1196, 2006.

[43] J. Y. Kim, C. Lee, S. Bae, K. S. Kim, B. H. Hong, and E. J. Choi, "Far-infrared study of substrate-effect on large scale graphene," *Appl. Phys. Lett.,* vol. 98, pp. 201907, 2011.

[44] J. M. Dawlaty, S. Shivaraman, J. Strait, P. George, M. Chandrashekhar, F. Rana, M. G. Spencer, D. Veksler, and Y. Chen, "Measurement of the optical absorption spectra of epitaxial graphene from terahertz to visible," *Appl. Phys. Lett.,* vol. 93, pp. 131905, 2008.

[45] Y-W. Tan, Y. Zhang, K. Bolotin, Y. Zhao, S. Adam, E. H. Hwang, S. D. Sarma, H. L. Stormer, and P. Kim, "Measurement of scattering rate and minimum conductivity in graphene," *Phys. Rev. lett.*, vol. 99, pp. 246803, 2007.

[46] CST Microwave Studio 2014, CST GmbH http://www.cst.com.

[47] V. G. Veselago. "The Electrodynamics of Substances with Simultaneously Negative Values of ε and μ," *Sov. Phys. Usp.*, vol. 10, no. 4, pp. 509-514, 1968.

[48] J. B. Pendry, "Negative refraction makes a perfect lens," *Phys. Rev. Lett., vol.* 85, no. 18, p. 3966, 2000.

[49] S. A. Ramakrishna, J. B. Pendry, M. C. K. Wiltshire, and W. J. Stewart, "Imaging the Near

Field," *J. Mod. Opt.*, vol. 50, no. 9, pp. 1419-1430, 2003.

[50] A. Grbic and G. V. Eleftheriades, "Overcoming the Diffraction Limit with a Planar Left-Handed Transmission-Line Lens," Phys. Rev. Lett., vol. 92, no. 11, p. 117403, 2004.

[51] T. Taubner, D. Korobkin, Y. Urzhumov, G. Shvets, and R. Hillenbrand, "Near-Field Microscopy Through a SiC Superlens," *Science*, vol. 313, no. 5793, pp. 1595-1595, 2006.

[52] R. Merlin, "Radiationless Electromagnetic Interference: Evanescent-Field Lenses and Perfect Focusing," *Science*, vol. 317, no. 5840, pp. 927-929, 2007.

[53] S. C. Kehr, Y. M. Liu, L. W. Martin, P. Yu, M. Gajek, S. Y. Yang, C. -H. Yang, M. T. Wenzel, R. Jacob, H. -G. von Ribbeck, M. Helm, X. Zhang, L. M. Esh, and R. Ramesh, "Microspectroscopy on Perovskite-Based Superlenses," *Opt. Mater. Express*, vol. 1, no. 5, pp. 1051-1060, 2011.

[54] P. Li and T. Taubner, "Multi-Wavelength Superlensing with Layered Phonon-Resonant Dielectrics," *Opt. Express*, vol. 20, no. 11, pp. 11787-11795, 2012.

[55] H. Liu, B. Wang, L. Ke, J. Deng, C. C. Chum, S. L. Teo, L.Shen, S. A. Maier, J. H. Teng, "High Aspect Subdiffraction-Limit Photolithography via a Silver Superlens," *Nano Lett.*, vol. 12, no. 3, pp. 1549-1554, 2012.

[56] S. Maslovski, S. Tretyakov, and P. Alitalo, "Near-field Enhancement and Imaging in Double Planar Polariton-Resonant Structures," *J. Appl. Phys.*, vol. 96, no. 3, pp. 1293-1300, 2004.

[57] S. I. Maslovski and S. A. Tretyakov, "Phase Conjugation and Perfect Lensing," *J. Appl. Phys.*, vol. 94, no. 7, pp. 4241-4243, 2003.

[58] S. I. Maslovski, "Subwavelength Imaging with Arrays of Plasmonic Scatterers," *Opt.*

Commun., vol. 285, no. 16, pp. 3363-3367, 2012.

[59] S. I. Maslovski and S. A. Tretyakov, "Perfect Lensing with Phase-Conjugating Surfaces: Toward Practical Realization," *New J. Phys.*, vol. 14, no. 3, p. 035007, 2012.

[60] G. W. Hanson, "Quasi-Transverse Electromagnetic Modes Supported by a Graphene Parallel-Plate Waveguide," *J. Appl. Phys.*, vol. 104, no. 8, p. 084314, 2008.

[61] B. Wang, Z. Xiang, Y. Xiaocong, and T. Jinghua, "Optical Coupling of Surface Plasmons between Graphene Sheets," *Appl. Phys. Lett.*, vol. 100, no. 13, p. 131111, 2012.

[62] A. Vakil, and N. Engheta, "Transformation Optics Using Graphene," *Science*, vol. 332, no. 6035, pp. 1291-1294, 2011.

[63] G. W. Hanson, A. B. Yakovlev, and A. Mafi, "Excitation of Discrete and Continuous Spectrum for a Surface Conductivity Model of Graphene," *J. Appl. Phys.*, vol. 110, no. 11, p. 114305, 2011.

[64] A. Andryieuski, A. V. Lavrinenko, and D. N. Chigrin, "Graphene Hyperlens for Terahertz Radiation," *Phys. Rev. B*, vol. 86, no. 12, p. 121108, 2012.

[65] T. Zhang, L. Chen, and X. Li, "Graphene-Based Tunable Broadband Hyperlens for Far-field Subdiffraction Imaging at Mid-infrared Frequencies," *Opt. Express*, vol. 21, no. 18, pp. 20888-20899, 2013.

[66] P. Li and T. Taubner, "Broadband Subwavelength Imaging Using a Tunable Graphene-Lens," *ACS Nano*, vol. 6, no. 11, pp. 10107-10114, 2012.

[67] P. Ikonen, P. Belov, C. Simovski, and S. Maslovski, "Experimental Demonstration of Subwavelength Field Channeling at Microwave Frequencies Using a Capacitively Loaded

Wire Medium," *Phys. Rev. B*, vol. 73, no. 7, p. 073102, 2006.

[68] P. A. Belov and M. G. Silveirinha, "Resolution of Subwavelength Transmission Devices Formed By a Wire Medium," *Phys. Rev. E*, vol. 73, no. 5, p. 056607, 2006.

[69] M. G. Silveirinha, P. A. Belov, and C. R. Simovski, "Subwavelength Imaging at Infrared Frequencies Using an Array of Metallic Nanorods," *Phys. Rev. B*, vol. 75, no.3, p. 035108, 2007.

[70] M. G. Silveirinha, P. A. Belov, and C. R. Simovski, "Ultimate Limit of Resolution of Subwavelength Imaging Devices Formed by Metallic Rods," *Opt. lett.*, vol. 33, no. 15, pp. 1726-1728, 2008.

[71] C. S. Kaipa, A. B. Yakovlev, G. W. Hanson, Y. R. Padooru, F. Medina, and F. Mesa, "Enhanced Transmission with a Graphene-Dielectric Microstructure at Low-Terahertz Frequencies," *Phys. Rev. B*, vol. 85, no. 24, p. 245407, 2012.

[72] C. S. R. Kaipa, A. B.Yakovlev, F. Medina, F.Mesa, C. A. M. Butler, and A. P. Hibbins, "Circuit Modeling of the Transmissivity of Stacked Two-Dimensional Metallic Meshes," *Opt. Express*, vol. 18, no. 13, pp. 13309-13320, 2010.

[73] Y. Fan, Z. Wei, H. Li, H. Chen, and C. M. Soukoulis, "Photonic Band Gap of a Graphene-Embedded Quarter-Wave Stack," *Phys. Rev. B*, vol. 88, no.24, p. 241403, 2013.

[74] A. B. Yakovlev, Y. R. Padooru, G. W. Hanson, A. Mafi, and S. Karbasi, "A Generalized Additional Boundary Condition for Mushroom-Type and Bed-of-Nails-Type Wire Media," *IEEE Trans. Microwave Theory Tech.*, vol. 59, no. 3, pp. 527-532, 2011.

[75] A. B. Yakovlev, Y. R. Padooru, S. Karbasi, G. W. Hanson, and A. Mafi, "Nonlocal Homogenization Model for the Analysis of Absorbing Properties of Mushroom Structures with

Graphene Patches at Microwaves," *IEEE AP-S Int. Symp. and URSI Radio Science Meeting, Toronto, ON, Canada*, 2010.

[76] C. S. Kaipa, A. B. Yakovlev, S. I. Maslovski, and M. G. Silveirinha, "Near-Field Imaging with a Loaded Wire Medium," *Phys. Rev. B*, vol. 86, no. 15, p. 155103, 2012.

[77] B. D. F. Casse, W. T. Lu, Y. J. Huang and S. Sridhar, "Robust Method to Determine the Resolution of a Superlens by Analyzing the Near-Field Image of a Two-Slit Object," *Physics. Optics*, vol. 1105, 2011.

[78] S. H. Jiang and R. Pike, "A Full Electromagnetic Simulation Study of Near-Field Imaging Using Silver Films," *New J. Phys.*, vol. 7, no. 1, p. 169, 2005.

[79] P. Kolinko and D. Smith, "Numerical Study of Electromagnetic Waves Interacting with Negative Index Materials," *Opt. Express*, vol. 11, no. 7, pp. 640-648, 2003.

[80] W. T. Lu and S. Sridhar, "Near-Field Imaging by Negative Permittivity Media," *Microw. Opt. Tech. Lett.*, vol. 39, no. 4, pp. 282-286, 2003.

[81] X. Yang, Y. Liu, J. Ma, J. Cui, H. Xing, W. Wang, C. Wang, and X. Luo, "Broadband Super-Resolution Imaging by a Superlens with Unmatched Dielectric Medium," *Opt. Express*, vol. 16, no. 24, pp. 19686-19694, 2008.

[82] P. A. Belov, Y. Zhao, S. Sudhakaran, A. Alomainy, and Y. Hao, "Experimental Study of the Subwavelength Imaging by a Wire Medium Slab," *Appl. Phys. Lett.*, vol. 89, no. 26, p. 262109, 2006.

[83] Z. Wei, Y. Cao, Z. Gong, X. Su, Y. Fan, C. Wu, J. Zhang, and H. Li, "Subwavelength Imaging with a Fishnet Flat Lens," *Phys. Rev. B*, vol. 88, no. 19, p. 195123, 2013.

[84] A. Reina, X. Jia, J. Ho, D. Nezich, H. Son, V. Bulovic, M. S. Dresselhaus, and J. Kong,

"Large Area, Few-Layer Graphene Films on Arbitrary Substrates by Chemical Vapor Deposition," *Nano Lett.*, vol. 9, no. 1, pp. 30-35, 2008.

[85] P. W. Sutter, J-I Flege, and E. A. Sutter, "Epitaxial Graphene on Ruthenium," *Nat. Mater.,* vol. 7, no. 5, pp. 406-411, 2008.

[86] A. Reina, H. Son, L. Jiao, B. Fan, M. S. Dresselhaus, Z. Liu, and J. Kong, "Transferring and Identification of Single- and Few-Layer Graphene on Arbitrary Substrates," *J. of Phys. Chem. C*, vol. 112, no. 46, pp. 17741-17744, 2008.

[87] M. G. Silveirinha, "Additional Boundary Condition for the Wire Medium," *IEEE Trans. Antennas Propag.*, vol. 54, no. 6, pp. 1766-1780, 2006.

[88] M. G. Silveirinha, C. A. Fernandes, and J. R. Costa, "Additional Boundary Condition for a Wire Medium Connected to a Metallic Surface," *New J. Phys.*, vol. 10, no. 5, p. 053011, 2008.

[89] O. Luukkonen, M. G. Silveirinha, A. B. Yakovlev, C. R. Simovski, I. S. Nefedov, and S. A. Tretyakov, "Effects of Spatial Dispersion on Reflection From Mushroom-Type Artificial Impedance Surfaces," *IEEE Trans. Microwave Theory Tech.*, vol. 57, no. 11, pp. 2692-2699, 2009.

[90] A. B. Yakovlev, M. G. Silveirinha, O. Luukkonen, C. R. Simovski, I. S. Nefedov, and S. A. Tretyakov, "Characterization of Surface-Wave and Leaky-Wave Propagation on Wire-Medium Slabs and Mushroom Structures Based on Local and Nonlocal Homogenization Models," *IEEE Trans. Microwave Theory Tech.*, vol. 57, no. 11, pp. 2700-2714, 2009.

[91] M. G. Silveirinha, C. A. Fernandes, and J. R. Costa, "Electromagnetic Characterization of Textured Surfaces Formed by Metallic Pins," *IEEE Trans. Antennas Propag*., vol. 56, no. 2,

pp. 405-415, 2008.

[92] M. G. Silveirinha, and C. A. Fernandes, "Homogenization of 3-D-Connected and Nonconnected Wire Metamaterials," *IEEE Trans. Microwave Theory Tech.*, vol. 53, no. 4, pp. 1418-1430, 2005.

[93] L. Solymar and E. Shamonina, "Waves in Metamaterials," Oxford University Press, 2009.

[94] F. Medina, F. Mesa, and D. C. Skigin, "Extraordinary Transmission through Arrays of Slits: A Circuit Theory Model," *IEEE Trans. Microwave Theory Tech.*, vol. 58, no. 1, pp. 105-115, 2010.

[95] C. S. Kaipa, A. B. Yakovlev, F. Medina, and F. Mesa, "Transmission through Stacked 2D Periodic Distributions of Square Conducting Patches," *J. Appl. Phys.*, vol. 112, no. 3, p. 033101, 2012.

[96] M. Born and E. Wolf, "Principles of Optics: Electromagnetic Theory of Propagation, Interference and Diffraction of Light," Cambridge University Press: Cambridge, 1999.

[97] X. Li, F. Gao, and Z. Gu, "Nanowire Joining Methods," *Open Surf. Sci. J.,* vol. 3, pp. 91-104, 2011.

[98] X. Zhang and Z. Liu, "Superlenses to Overcome the Diffraction Limit," *Nat. Mat.,* vol. 7, no. 6, pp. 435-441, 2008.

[99] N. Fang, H. Lee, C. Sun, and X. Zhang, "Sub–Diffraction-Limited Optical Imaging with a Silver Superlens," *Science*, vol. 308, no. 5721, pp. 534-537, 2005.

[100] F. Mesa, M. J. Freire, R. Marquès, and J. D. Baena, "Three-Dimensional Superresolution in Metamaterial Slab Lenses: Experiment and Theory," *Phys. Rev. B,* vol. 72, no. 23, p.

235117, 2005.

[101] M. C. K. Wiltshire, "Radio Frequency (RF) Metamaterials." *Phys. Status Solidi B,* vol. 244, no. 4, pp. 1227-1236, 2007.

[102] S. Stankovich, D. A. Dikin, R. D. Piner, K. A. Kohlhaas, A. Kleinhammes, Y. Jia, Y. Wu, S. T. Nguyen, and R. S. Ruoff, "Synthesis of Graphene-Based Nanosheets via Chemical Reduction of Exfoliated Graphite Oxide," *Carbon*, vol. 45, no. 7, pp. 1558-1565, 2007.

[103] K. S. Kim, Y. Zhao, H. Jang, S. Y. Lee, J. Min Kim, K. S. Kim, J-H. Ahn, P. Kim, J-Y. Choi, and B. H. Hong, "Large-Scale Pattern Growth of Graphene Films for Stretchable Transparent Electrodes," *Nature*, vol. 457, no. 7230, pp. 706-710, 2009.

[104] J. Feng, W. Li, X. Qian, J. Qi, L. Qi, and J. Li., "Patterning of Graphene," *Nanoscale*, vol. 4, no. 16, pp. 4883-4899, 2012.

[105] J-Y. Hong and J. Jang, "Micropatterning of Graphene Sheets: Recent Advances in Techniques and Applications," *J. Mat. Chem.,* vol. 22, no. 17, pp. 8179-8191, 2012.

[106] W. Xiong, Y. S. Zhou, W. J. Hou, L. J. Jiang, Y. Gao, L. S. Fan, L. Jiang, J. F. Silvain, and Y. F. Lu, "Direct Writing of Graphene Patterns on Insulating Substrates under Ambient Conditions," *Scientific reports,* vol. 4, 2014.

[107] J. B. Park, W. Xiong, Y. Gao, M. Qian, Z. Q. Xie, M. Mitchell, Y. S. Zhou, G. H. Han, L. Jiang, and Y. F. Lu, "Fast Growth of Graphene Patterns by Laser Direct Writing," Appl. Phys. Lett. 98, 123109 (2011).

[108] K. S. Novoselov, D. Jiang, F. Schedin, T. J. Booth, V. V. Khotkevich, S. V. Morozov and A. K. Geim, "Two-Dimensional Atomic Crystals," *Proc. Natl. Acad. Sci. U. S. A.*, vol. 102, pp. 10451–10453, 2005.

APPENDIX

Here, we provide the procedure details to obtain the unknown scattering coefficients. As a starting point, by inserting (1.1) and (1.2) into (1.8) and using the orthogonality relations for the trigonometric functions on $[-\pi, \pi]$ we obtain:

$$[a_n J_n(\beta_2 R_0) + b_n Y_n(\beta_2 R_0)]\pi\xi_n = \sum_{i=0}^{\infty} A_{v_i} J_{v_i}(\beta_1 R_0) < \cos(v_i\phi)\,, \cos(n\phi) > . \quad \text{(A. 1)}$$

Substituting (1.1) and (1.2) into (1.9) and applying the orthogonality relations for the trigonometric functions on $[-\alpha, \alpha]$ yields:

$$\frac{\beta_1}{j\omega} A_{v_i} J'_{v_i}(\beta_1 R_0)\alpha = \frac{\beta_2}{j\omega} \sum_{n=0}^{\infty} [a_n J'_n(\beta_2 R_0) + b_n Y'_n(\beta_2 R_0)] < \cos(v_i\phi)\,, \cos(n\phi) > \quad \text{(A. 2)}$$

where $< T_1, T_2 >= \int_{-\alpha}^{\alpha} T_1 T_2 d\phi$ is the inner product on the interval $[-\alpha, \alpha]$. It should be mentioned that the prime symbol indicates the partial derivative with respect to the entire argument of the Bessel and Hankel functions.

The insertion of (A.2) into (A.1) leads to:

$$a_n J_n(\beta_2 R_0)\pi\xi_n - \sum_{i=0}^{\infty} \frac{\beta_2}{\beta_1} \frac{J_{v_i}(\beta_1 R_0)}{J'_{v_i}(\beta_1 R_0)\alpha} \sum_{m=0}^{\infty} a_m J'_m(\beta_2 R_0) \times$$

$$< \cos(v_i\phi)\,, \cos(m\phi) > < \cos(v_i\phi)\,, \cos(n\phi) >$$

$$= -b_n Y_n(\beta_2 R_0)\pi\xi_n + \sum_{i=0}^{\infty} \frac{\beta_2}{\beta_1} \frac{J_{v_i}(\beta_1 R_0)}{J'_{v_i}(\beta_1 R_0)\alpha} \sum_{m=0}^{\infty} b_m Y'_m(\beta_2 R_0) \times$$

$$< \cos(v_i\phi)\,, \cos(m\phi) > < \cos(v_i\phi)\,, \cos(n\phi) > \quad \text{(A. 3)}$$

(A. 3) can be written in the form of a system of linear equations as follows:

$$[X]_{n\times m}[a_m]_{m\times 1} = [Y]_{n\times m}[b_m]_{m\times 1} \tag{A. 4}$$

where

$$[X]_{n\times m} = \begin{bmatrix} J_0(\beta_2 R_0)\pi\xi_0 & \cdots & 0 \\ \vdots & \ddots & \vdots \\ 0 & \cdots & J_n(\beta_2 R_0)\pi\xi_n \end{bmatrix} + \begin{bmatrix} H_{00} & \cdots & H_{0m} \\ \vdots & \ddots & \vdots \\ H_{n0} & \cdots & H_{nm} \end{bmatrix} \tag{A. 5}$$

$$H_{nm} = \sum_{i=0}^{\infty} \frac{\beta_2}{\beta_1} \frac{J_{v_i}(\beta_1 R_0)}{J'_{v_i}(\beta_1 R_0)\alpha} J'_m(\beta_2 R_0) < \cos(v_i\phi), \cos(m\phi) > < \cos(v_i\phi), \cos(n\phi) > \tag{A. 6}$$

$$[Y]_{n\times m} = \begin{bmatrix} -Y_0(\beta_2 R_0)\pi\xi_0 & \cdots & 0 \\ \vdots & \ddots & \vdots \\ 0 & \cdots & -Y_n(\beta_2 R_0)\pi\xi_n \end{bmatrix} + \begin{bmatrix} P_{00} & \cdots & P_{0m} \\ \vdots & \ddots & \vdots \\ P_{n0} & \cdots & P_{nm} \end{bmatrix} \tag{A. 7}$$

$$P_{nm} = \sum_{i=0}^{\infty} \frac{\beta_2}{\beta_1} \frac{J_{v_i}(\beta_1 R_0)}{J'_{v_i}(\beta_1 R_0)\alpha} Y'_m(\beta_2 R_0) < \cos(v_i\phi), \cos(m\phi) > < \cos(v_i\phi), \cos(n\phi) > . \tag{A. 8}$$

Here we assume $m = n$. Therefore, (A4-1) can be rewritten as:

$$[Y]^{-1}{}_{n\times n}[X]_{n\times n}[a_n]_{n\times 1} = [b_n]_{n\times 1} \tag{A. 9}$$

$$[Z]_{n\times n} = [Y]^{-1}{}_{n\times n}[X]_{n\times n} \tag{A. 10}$$

$$\begin{bmatrix} Z_{00} & \cdots & Z_{0n} \\ \vdots & \ddots & \vdots \\ Z_{n0} & \cdots & Z_{nn} \end{bmatrix} \begin{bmatrix} a_0 \\ \vdots \\ a_n \end{bmatrix} = \begin{bmatrix} b_0 \\ \vdots \\ b_n \end{bmatrix} \tag{A. 11}$$

When (1.2) and (1.3) are substituted in (1.4) and (1.5) yields:

$$A_n^{\text{inc}} J_n(\beta_0 R_c) + A_n^{\text{scat}} H_n^{(2)}(\beta_0 R_c) = a_n J_n(\beta_2 R_c) + b_n Y_n(\beta_2 R_c) \tag{A. 12}$$

$$a_n \left[J_n(\beta_2 R_c) + \frac{\beta_2 Z_s}{j\omega\mu_0} J'_n(\beta_2 R_c) \right] + b_n \left[Y_n(\beta_2 R_c) + \frac{\beta_2 Z_s}{j\omega\mu_0} Y'_n(\beta_2 R_c) \right]$$

$$= Z_s \left[\frac{\beta_0}{j\omega\mu_0} \left(A_n^{\text{inc}} J_n'(\beta_0 R_c) + A_n^{\text{scat}} H_n^{(2)'}(\beta_0 R_c) \right) \right] \tag{A. 13}$$

(A. 13) by using (A. 12) can be expressed as:

$$a_n \left(J_n(\beta_2 R_c) \left[1 - \frac{\beta_0 Z_s}{j\omega\mu_0} \frac{H_n^{(2)'}(\beta_0 R_c)}{H_n^{(2)}(\beta_0 R_c)} \right] + \frac{\beta_2 Z_s}{j\omega\mu_0} J_n'(\beta_2 R_c) \right)$$

$$+ b_n \left(Y_n(\beta_2 R_c) \left[1 - \frac{\beta_0 Z_s}{j\omega\mu_0} \frac{H_n^{(2)'}(\beta_0 R_c)}{H_n^{(2)}(\beta_0 R_c)} \right] + \frac{\beta_2 Z_s}{j\omega\mu_0} Y_n'(\beta_2 R_c) \right)$$

$$= A_n^{\text{inc}} \frac{\beta_0 Z_s}{j\omega\mu_0} \left(J_n'(\beta_0 R_c) - \frac{H_n^{(2)'}(\beta_0 R_c)}{H_n^{(2)}(\beta_0 R_c)} J_n(\beta_0 R_c) \right) \tag{A. 14}$$

(A. 14) can be written in the form of a system of linear equations as follows:

$$[L]_{n\times n}[a_n]_{n\times 1} + [M]_{n\times n}[b_n]_{n\times 1} = \left[A_n^{\text{inc}}\right]_{n\times 1} \tag{A. 15}$$

where

$$[L]_{n\times n} = \begin{bmatrix} L_0 & \cdots & 0 \\ \vdots & \ddots & \vdots \\ 0 & \cdots & L_n \end{bmatrix} \tag{A. 16}$$

$$L_n = \frac{J_n(\beta_2 R_c) \left[1 - \frac{\beta_0 Z_s}{j\omega\mu_0} \frac{H_n^{(2)'}(\beta_0 R_c)}{H_n^{(2)}(\beta_0 R_c)} \right] + \frac{\beta_2 Z_s}{j\omega\mu_0} J_n'(\beta_2 R_c)}{\frac{\beta_0 Z_s}{j\omega\mu_0} \left[J_n'(\beta_0 R_c) - \frac{H_n^{(2)'}(\beta_0 R_c)}{H_n^{(2)}(\beta_0 R_c)} J_n(\beta_0 R_c) \right]}$$

$$[M]_{n\times n} = \begin{bmatrix} M_0 & \cdots & 0 \\ \vdots & \ddots & \vdots \\ 0 & \cdots & M_n \end{bmatrix} \tag{A. 17}$$

$$M_n = \frac{Y_n(\beta_2 R_c)\left[1 - \frac{\beta_0 Z_s}{j\omega\mu_0}\frac{H_n^{(2)'}(\beta_0 R_c)}{H_n^{(2)}(\beta_0 R_c)}\right] + \frac{\beta_2 Z_s}{j\omega\mu_0} Y_n'(\beta_2 R_c)}{\frac{\beta_0 Z_s}{j\omega\mu_0}\left[J_n'(\beta_0 R_c) - \frac{H_n^{(2)'}(\beta_0 R_c)}{H_n^{(2)}(\beta_0 R_c)} J_n(\beta_0 R_c)\right]}.$$

Inserting (A. 9) into (A. 15) we obtain:

$$\left([L]_{n\times n} + [M]_{n\times n}[Y]^{-1}{}_{n\times n}[X]_{n\times n}\right)[a_n]_{n\times 1} = \left[A_n^{\text{inc}}\right]_{n\times 1} \tag{A. 18}$$

$$[K]_{n\times n} = [L]_{n\times n} + [M]_{n\times n}[Y]^{-1}{}_{n\times n}[X]_{n\times n} \tag{A. 19}$$

$$\begin{bmatrix} K_{00} & \cdots & K_{0n} \\ \vdots & \ddots & \vdots \\ K_{n0} & \cdots & K_{nn} \end{bmatrix}\begin{bmatrix} a_0 \\ \vdots \\ a_n \end{bmatrix} = \begin{bmatrix} A_0^{\text{inc}} \\ \vdots \\ A_n^{\text{inc}} \end{bmatrix}. \tag{A. 20}$$

a_n can be calculated directly from the coefficient A_n^{inc} by utilizing (A. 20) and then b_n can be obtained by inserting a_n in (A. 9). Finally, A_n^{scat} can be achieved by substituting the values of a_n and b_n in (A. 12). Similarly, B_n^{scat} can be obtained.

VITA

SEYEDALI FOROUZMAND

1711 Anderson Road, Apt. 4202B1 • Oxford, MS 38655 • (949)302-0342• sforouzm@go.olemiss.edu

EDUCATION

- M.Sc., Electrical Engineering, University of Mississippi (UM), Summer 2015.

  Concentrations: Electromagnetics

  Thesis: Graphene Based Metamaterials for Terahertz Cloaking and Subwavelength Imaging.
- B.Sc., Electrical Engineering, Ferdowsi University of Mashhad, Iran, Spring 2013.

  Thesis: Plasmonics: Theory and Applications.

TEACHING EXPERIENCE

- Electromagnetic Fields and Waves course, Prof. Mirsalehi, Ferdowsi University of Mashhad, Fall 2011, Spring 2012, and Spring 2013.
- Electromagnetics course, Prof. Mirsalehi, Bahar University of Mashhad, Fall 2012 and Spring 2013.
- Antenna and Electromagnetic Wave Propagation course, Prof. Mahdizahed, Bahar University of Mashhad, Spring 2013.

- Filters and Circuits Synthesis course, Prof. Ebrahimi, Ferdowsi University of Mashhad, Fall 2012.
- Engineering Mathematics, Prof. Moghimi, Ferdowsi University of Mashhad, Fall 2012.
- Electronic 3 course, Prof. Maymandi, Ferdowsi University of Mashhad, Spring 2012.
- Electric Circuit Analysis, University of Mississippi, Fall 2013, Spring 2014, Fall 2014.

HONORS and FELLOWSHIPS

- Selected for the first round of Unibo Action 2 study grants at University of Bologna (02/27/2013).
- Selected for Graduate Assistantship in the Electrical Engineering Department-University of Mississippi, since Fall 2013.

PUBLICATIONS and PRESENTATIONS

- A. Forouzmand and A. B. Yakovlev, "Cloaking of a Conducting Finite Wedge with Graphene Nanopatches," 2014 IEEE AP-S International Symposium on Antennas and Propagation and USNC/URSI Radio Science Meeting, pp. 1435-1436, 2014.
- A. Forouzmand and A. B. Yakovlev, "Broadband Subwavelength Imaging with a Wire Medium Slab Loaded with Graphene Sheets," IEEE 9th European Conference on Antennas and Propagation (EUCAP), 12-17 April 2015, Lisbon, Portugal, (submitted 20 October 2014, accepted 18 December 2014).
- A. Forouzmand and A. B. Yakovlev, "Electromagnetic Cloaking of a Conducting Finite Wedge with a Nanostructured Graphene Metasurface," IEEE Transactions on Antennas and Propagation, vol. 63, no.5, 2015, (submitted 25 November 2014, accepted 16 February 2015).

- A. Forouzmand, H. M. Bernety, and A. B. Yakovlev, "Graphene Loaded Wire Medium for Tunable Broadband Subwavelength Imaging," Physical Review B, (submitted 12 February 2015).
- A. Forouzmand and A. B. Yakovlev, "Tunable Dual-Band Subwavelength Imaging with a Wire Medium Slab Loaded with Nanostructured Graphene Metasurfaces," 9th International Congress on Advanced Electromagnetic Materials in Microwaves and Optics – Metamaterials 2015, (submitted 17 March 2015).
- A. Forouzmand and A. B. Yakovlev, "Tunable Dual-Band Subwavelength Imaging with a Wire Medium Slab Loaded with Nanostructured Graphene Metasurfaces," Journal of Applied Physics, (submitted 4 May 2015).
- A. Forouzmand and A. B. Yakovlev, "Mushroom-Type Structures with the Wires Connected Through Diodes," IEEE Transactions on Microwave Theory and Techniques, (to be submitted).
- A. Forouzmand and A. B. Yakovlev, "Broadband Subwavelength Imaging with a Wire Medium Slab Loaded with Graphene Sheets," Broadband Wireless Access and Applications (BWAC), Oxford, MS, 2015. (Poster)
- 2014 IEEE International Symposium on Antennas and Propagation and USNC-URSI Radio Science Meeting.
    - "Cloaking of a Conducting Finite Wedge with Graphene Nanopatches". (Presentation)
    - "Mushroom-Type Structures with the Wires Connected Through Diodes: Electronically Tunable properties". (Presentation)